Spring 1-1-2015

# Characterizing Longitude-Dependent Orbital Debris Congestion in the Geosynchronous Orbit Regime

Paul Vincent Anderson
*University of Colorado at Boulder*, anderson.paul.v@gmail.com

**Characterizing Longitude-Dependent Orbital Debris Congestion in the Geosynchronous Orbit Regime**

by

**Paul V. Anderson**

B.S., Embry-Riddle Aeronautical University, 2011

M.S., University of Colorado Boulder, 2014

A thesis submitted to the

Faculty of the Graduate School of the

University of Colorado in partial fulfillment

of the requirements for the degree of

Doctor of Philosophy

Department of Aerospace Engineering Sciences

2015

This thesis entitled:
Characterizing Longitude-Dependent Orbital Debris Congestion in the Geosynchronous Orbit Regime
written by Paul V. Anderson
has been approved for the Department of Aerospace Engineering Sciences

_____
Dr. Hanspeter Schaub

_____
Dr. Brandon Jones

_____
Dr. Jeffrey Parker

_____
Dr. Juan Restrepo

_____
Dr. Darren McKnight

Date _____

The final copy of this thesis has been examined by the signatories, and we find that both the content and the form meet acceptable presentation standards of scholarly work in the above mentioned discipline.

Anderson, Paul V. (Ph.D., Aerospace Engineering Sciences)

Characterizing Longitude-Dependent Orbital Debris Congestion in the Geosynchronous Orbit Regime

Thesis directed by Dr. Hanspeter Schaub

The geosynchronous orbit (GEO) is a unique commodity of the satellite industry that is becoming increasingly contaminated with orbital debris, but is heavily populated with high-value assets from the civil, commercial, and defense sectors. The GEO arena is home to hundreds of communications, data transmission, and intelligence satellites collectively insured for an estimated 18.3 billion USD. As the lack of natural cleansing mechanisms at the GEO altitude renders the lifetimes of GEO debris essentially infinite, conjunction and risk assessment must be performed to safeguard operational assets from debris collisions.

In this thesis, longitude-dependent debris congestion is characterized by predicting the number of near-miss events per day for every longitude slot at GEO, using custom debris propagation tools and a torus intersection metric. Near-miss events with the present-day debris population are assigned risk levels based on GEO-relative position and speed, and this risk information is used to prioritize the population for debris removal target selection. Long-term projections of debris growth under nominal launch traffic, mitigation practices, and fragmentation events are also discussed, and latitudinal synchronization of the GEO debris population is explained via node variations arising from luni-solar gravity.

In addition to characterizing localized debris congestion in the GEO ring, this thesis further investigates the conjunction risk to operational satellites or debris removal systems applying low-thrust propulsion to raise orbit altitude at end-of-life to a super-synchronous disposal orbit. Conjunction risks as a function of thrust level, miss distance, longitude, and semi-major axis are evaluated, and a guidance method for evading conjuncting debris with continuous thrust by means of a thrust heading change via single-shooting is developed.

**Dedication**

*To God, my Heavenly Father,*

*To Jesus Christ, my Savior,*

*To the Spirit, my Sanctifier,*

*for empowering me for this work*

*To Ashley, my wife,*

*for showing me the Gospel*

*To Vince and Lynn, my parents,*

*for making all of this possible*

---

"Whatever your hand finds to do, do it with your might"

Ecclesiastes 9:10 (esv)

---

## Acknowledgements

Foremost, I am honored and grateful to have had Dr. Hanspeter Schaub as my Ph.D. advisor. I have grown in an academic, technical, and professional sense under your continual guidance, support, and encouragement. Thank you for your mentorship, and support when I moved away to California after my wedding. To my committee, Dr. Brandon Jones, Dr. Jeff Parker, Dr. Juan Restrepo, and Dr. Darren McKnight, thank you for your academic and professional support of this work – your insights have helped to strengthen this thesis.

Ashley Anderson, I thank you for your unconditional love and patience throughout this process. My life changed the moment I laid eyes on you, sitting in the back row of orbit determination class. Now, as your husband, I look forward to our beautiful, godly future.

I will always be grateful for the continual love and support of my parents, Vince and Lynn Anderson. Your encouragement and motivation have granted me the opportunity to boldly pursue my dreams, one of which is achieving the Ph.D. I write with the knowledge that I would not be where I am so joyfully today without your selfless investments in me.

I would also like to acknowledge the other students working in the AVS Lab over the past several years, especially Lee Jasper, Erik Hogan, and Steve O'Keefe. I am thankful for our enjoyable collaborations, our thought-provoking discussions about life, research, and coursework, and—of course—our too-frequent Arnold Schwarzenegger movie quotations.

This dissertation was supported through two teaching assistantships generously provided by the Department of Aerospace Engineering Sciences, the Graduate Assistance in Areas of National Need (GAANN) fellowship, and the National Defense Science and Engineering Graduate (NDSEG) fellowship administered by the U.S. Department of Defense.

## Contents

**Chapter**

## Tables

**Table**

## Figures

**Figure**

# Chapter 1

# Introduction

## 1.1 Background and Motivation

The geosynchronous orbit (GEO) regime is a unique commodity of the Earth-orbiting satellite industry that is becoming increasingly contaminated with orbital debris,[5–7] but is heavily populated with high-value assets. The GEO orbit ring is home to hundreds of communications, remote sensing, and intelligence satellites harnessed for applications ranging from video and data transmission to weather support and broadband applications.[8] As of 2011, the net worth of insured satellites at GEO was valued at 18.3 billion USD.[8] As the lack of environmental cleansing mechanisms at the GEO altitude renders the lifetimes of GEO debris objects essentially infinitely long,[9–11] conjunction and mitigation assessments must be performed to safeguard operational assets from collisions with the current debris population, which could have costly financial, legal, and geopolitical consequences. Since GEO satellites are required to maintain specific longitude slots authorized by the International Telecommunication Union (ITU)[12]—and cannot simply phase shift to evade debris—analyses of the macroscopic behavior of the GEO debris population are useful for describing debris fluxes through particular longitude slots, to forecast how often operators with expensive satellites in these regions must potentially execute maneuvers to evade debris. As overcrowding of GEO is becoming a serious concern for satellite owners and operators internationally, knowledge of these debris flux patterns—termed *debris weather*[13]—is an imperative for space situational awareness (SSA) and mission assurance activities at GEO.

Existing debris analysis and evolution tools[14–16] use inertially-fixed spatial cell definitions to track debris cell passage events (CPE) triggered by osculating orbit intersections with cells of interest during long-term propagation of the orbital debris population. Harnessing a variety of probability models, the spatial density and flux contributions for each CPE—for each known derelict object—over a specified time frame are computed and subsequently employed in collision risk assessments. For the GEO regime, these analysis tools often average over cell right ascension, providing debris fluxes as a lower-resolution function of altitude and declination only.[11] Furthermore, if inertially-fixed cell definitions are used only, derelict flux contributions to particular GEO longitude slots at arbitrary times cannot be determined. Consequently, although spatially-averaged flux conditions at GEO may be estimated with existing software tools, local intersection events for arbitrary longitude slots are not accessible, and the latter is of significant interest to satellite operators concerned with the debris weather conditions in the vicinity of their operational satellites. Reference 1 emphasizes that fluxes averaged across longitude and time often grossly misrepresent the short-term collision hazard at GEO, and as a consequence, alternative GEO collision hazard depictions that employ higher temporal and spatial resolutions should be adopted by the operator community. Reference 8 illustrates that the gravitational wells at GEO render average debris flux a less relevant statistic for evaluating congestion at GEO, as the probability of collision at the center of these wells is *seven times larger* than at longitudes far from these regions. Therefore, a framework for quantifying which localized regions of the GEO regime are, in general, most susceptible to rising debris fluxes over different time frames of interest is a necessary, albeit challenging, undertaking to rectify the too-common misconception that orbit debris congestion levels at GEO are homogeneous over longitude.

Figure 1.1 depicts the unclassified and trackable (larger than approximately one meter in effective diameter for the GEO altitude[11]) resident space object (RSO) population at GEO for which up-to-date tracking data were available as of March 2014. Following a taxonomy introduced in the European Space Agency's *Classification of Geosynchronous Objects*

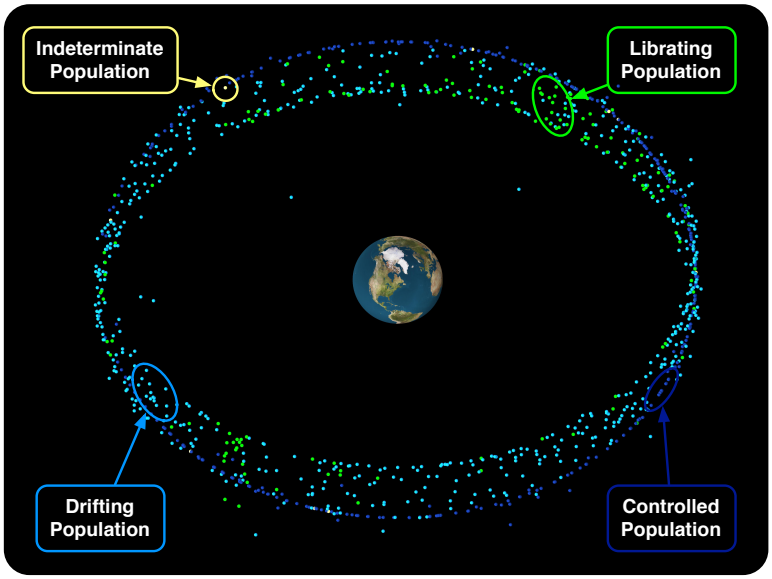


Figure 1.1: Snapshot of debris population in GEO regime.

reports, this population is subdivided into four primary classes: (1) fully-controlled satellites with East-West (longitude control) and/or North-South (inclination control) station-keeping capability, (2) drifting objects that circulate along the GEO regime, as seen by an Earth-fixed observer, (3) librating objects that are "trapped" and thus oscillate in longitude about one or both of the gravitational potential wells located at 75°E and 105°W longitude, and (4) indeterminate objects for which the type of orbit is unclassifiable or unknown. The GEO regime is subjected to a steadily-increasing population of catalogued objects, which grows at an average rate of 30 new entries each year.[11] As of March 2014, 1145 catalogued objects satisfied the European Space Operations Centre's (ESOC) criteria for GEO objects, and of this population, 35% is operational and under at least longitude control, but 51% is drifting above, below, or through the GEO ring, and 14% is librating about one or both of the gravitational wells. It is imperative to note that these large-scale debris objects—which consist of derelict satellites abandoned at end-of-life, Titan IIIC and Proton-K upper stages, etc.—constitute a subset of the actual debris field at GEO, which is dominated by significant populations of uncatalogued objects at sizes as small as 10-15 cm, detected in optical

observation campaigns and indicative of undetected break-up events in this regime.[8,17,18]

Localized, longitude-dependent congestion forecasting for the GEO regime is thus a fruitful and highly-applicable area of research, as it provides a metric as to how frequently satellite operators with assets in particular longitude slots will have to track nearby debris motion, perform high-precision conjunction assessments, and execute avoidance maneuvers if absolutely necessary. The latter is of particular importance, as avoidance maneuvers can temporarily force a satellite outside of its longitude slot, which may induce problems for the mission and be difficult to manage if neighboring assets are collocated in the same slot. Currently, the derelict population at GEO is sparse enough such that a simple time-shift of a scheduled maintenance maneuver is sufficient for evading debris – in these situations, no additional propellant is expended beyond that allocated for routine GEO station-keeping. However, as the debris population at GEO continues to increase, the amount of propellant required to maintain a specified longitude slot while simultaneously executing avoidance maneuvers—and the costs associated with analyzing conjunction events to determine if evasive action is even necessary—will begin increasing in tandem. Reference 8 summarizes the core implications of orbital debris, especially applicable to the GEO arena:

> *Space debris is no longer an academic issue. Nor is it merely an "environmental" problem; rather, debris has the potential to damage or destroy high-value, operational satellites with resulting revenue losses running into billions of U.S. dollars.*

Therefore, characterization of longitude-dependent debris weather trends is an imperative area of research that is not only directly applicable to the interests of GEO satellite owners and operators on an international scale, but is critical to preserving the long-term "health" and sustainability of this delicate regime, which has historically been too-often overlooked in environmental debris impact studies. To this end, this thesis shall paint an illuminating portrait of localized debris congestion at GEO, to drive further research in this critical area, and—ultimately—spearhead proactive, global cooperation in support of this orbit regime.

## 1.2 Previous Studies

As a consequence of the increasing population of derelict objects in the GEO regime, there was a growing concern as early as the 1980s regarding the overcrowding of the GEO arena and the long-term impacts on the sustainability of this regime[5,19] (for reference, the first spacecraft to be inserted into a GEO orbit was the USA's Syncom-2 satellite in 1963[5]). Although a variety of international mitigation standards have been implemented to curtail debris growth in this delicate arena, including NASA's Technical Standard 8719.14 (*Process for Limiting Orbital Debris*)[20] and the re-orbiting guidelines proposed by the Inter-Agency Space Debris Coordination Committee (IADC),[21,22] Reference 23 indicates that of the 80% of GEO operators in 2001-2010 that attempted to comply with mitigation standards, merely 50% were successful in achieving compliance. Johnson highlights the implications of non-enforceable mitigation guidelines – "the viability of voluntary protection measures for this regime depends upon the responsible actions of the aerospace community as a whole."[5] Thereby, in the absence of perfect adherence to adopted mitigation measures by operators internationally, the debris population in the GEO regime will continue steadily increasing.

Naturally, a variety of studies concerned with projecting the long-term growth of the GEO debris population began to arise in the literature. Flury assesses collision probability and long-term orbit evolution of the 1988 GEO debris population, and indicates the probability of collision over the gravitational wells is a factor of two larger than in less-congested regions.[24] Based on the 1999 debris catalogue, Yasaka constructs an evolution model that incorporates launch traffic, fragmentation events, and representative collision risks into a 200-year growth projection for GEO.[9] Wegener implements the European Space Agency's MASTER-2001 debris environment tool to quantify the effects of mission debris, explosion fragments, solid rocket motor (SRM) slag, and end-of-life re-orbiting on forecasted spatial density in the GEO regime.[6] References 25–29 exhaustively evaluate long-term evolution, stability, and performance factors for super-synchronous disposal orbits for GEO. Again,

these studies average over the GEO longitude slots, providing spatial density as a function of altitude or declination only, such that *local* density conditions are not available. Recently, McKnight and Di Pentino re-examine the 2010 debris population and demonstrate that the probability of collision over the gravitational wells is now a factor of seven larger than over less-congested regions, and emphasize that equatorial crossings of the derelict population are synchronized spatially and in time, such that local congestion increases are episodic.[1]

Although the literature strongly focuses on the effects of debris-generating fragmentation events in low-Earth orbit (LEO), several previous studies have been devoted to quantifying increases in collision risk driven by fragmentations in the GEO ring. Yasaka utilizes momentum and energy principles to model hyper-velocity impacts, and shows that the resulting fragment cloud remains close to the GEO altitude, and spreads longitudinally to all regions of the GEO ring in weeks.[30] Oltrogge and Finkleman consider a probable conjunction scenario at GEO to show that the fragment energy distribution resulting from breakup is sufficient for permeating all orbit regimes from re-entry through super-synchronous.[31] Hansen and Sorge indicate that although close approach velocities for the GEO regime are in general lower than in the LEO arena, a low-energy breakup over one of the gravitational wells could be a worst-case scenario in that resonance is preserved for most of the fragment population, serving to increase collision risk with operational assets at these longitudes.[32] Though the tools that the authors of these previous studies use for characterizing breakup events at GEO differ, the independent conclusions of each study agree that fragmentations at the GEO altitude have long-term consequences that are detrimental to the sustainability and continued usefulness of this unique orbital regime and driver for space development.

### 1.3 Research Overview and Scope

This thesis answers aspects of the following fundamental questions of interest to the GEO operator community, each expounding a dimension of long-term GEO sustainability:

(1) How severe is the longitude-dependent GEO congestion arising from the present-day, large-scale, unclassified, and trackable debris population? If 5-10 derelict objects at GEO could be removed immediately, which derelicts would be targeted?

(2) What are the effects of critical debris growth mechanisms, namely nominal launch traffic and fragmentation events, on longitude-dependent congestion at GEO? How does adherence to end-of-life mitigation standards affect derelict growth at GEO?

(3) What can be done *now* to limit derelict growth at GEO? If a low-thrust, tug removal system is envisioned, what trajectory guidance and control techniques are needed both for re-orbiting of debris and avoiding collisions, if demanded autonomously?

This thesis is thus organized into three core research goals reflective of this set of questions:

(1) *Research Goal 1 (Chapters 2-3)*: Forecasting longitude-dependent congestion at GEO arising from the current debris population, and investigating the mechanisms behind the wave-like latitudinal synchronization exhibited by the debris population.

(2) *Research Goal 2 (Chapters 4-5)*: Forecasting longitude-dependent congestion at GEO arising from nominal launch traffic, mitigation, and on-orbit fragmentation events.

(3) *Research Goal 3 (Chapters 6-7)*: Evaluating the conjunction challenges for low-thrust GEO debris removal maneuvers, and developing a guidance method for low-thrust, online debris avoidance during orbit raising to super-synchronous disposal orbits.

The scope—and specific tasks—relevant to each of these research goals are detailed below.

### 1.3.1 Research Goal 1

In Chapter 2, this thesis forecasts longitude-dependent debris congestion trends arising from the present-day, large-scale debris population in the GEO regime, using publicly-available tracking data to provide representative initial conditions for the population. This

is illustrative of the localized congestion that would result in the short-term if no additional debris were generated in this regime, and can be used to identify the subset of this derelict population that is consistently the most threatening to operational assets in the GEO arena for purposes of active debris removal (ADR) target selection. Furthermore, the latitudinal synchronization exhibited by the GEO debris population is investigated in Chapter 3, and explained by inclination and node variations driven by luni-solar perturbations at the GEO altitude. From this bottom-up, analytic theory, insights into top-down, operational observations of "macroscopic" GEO debris behavior are developed, which have implications for flight safety, anomaly resolution, sensor tasking, and space situational awareness at GEO.

Specific research tasks for accomplishing this thesis objective are provided as follows:

(1) Develop custom software to read TLE files, propagate GEO debris population forward in time, and determine near-miss events for each longitude slot in GEO ring.

(2) Characterize "congestion culprits" at GEO: the derelicts that dominate debris congestion both globally around GEO and in a localized, longitude-dependent sense.

(3) Develop risk functions to determine the most threatening subset of the large-scale GEO debris population in terms of proximity to the GEO ring and relative velocity.

(4) Merge theory of GEO orbit evolution with observational data to explain apparent anomalous behavior of derelicts not conforming to macroscopic synchronization.

### 1.3.2 Research Goal 2

The effects of two dominant debris growth mechanisms—nominal launch traffic and on-orbit fragmentation events—on longitude-dependent debris congestion at GEO are individually assessed in Chapters 4-5, to depict (a) the consequences of improperly-executed mitigation efforts with operational satellites reaching end-of-life, and (b) the consequences of on-orbit explosions and collisions in the GEO ring from a longitude-dependent perspec-

tive. Each of these research thrusts motivates a growing need to synthesize, demonstrate, and implement an environment remediation system tailored specifically for the GEO ring.

Specific research tasks for accomplishing this thesis objective are provided as follows:

(1) Use historical and projected GEO launch data to construct probability models that describe where GEO satellites are likely to reside in longitude and element space.

(2) Develop representative launch traffic models and implement population augmentation in software to characterize long-term debris congestion over 50 year period.

(3) Evaluate longitude-dependent effects of fragmentation events (i.e., explosions and collisions) on localized congestion—and longitude slot safety—in the GEO regime.

### 1.3.3 Research Goal 3

In Chapters 6-7, this thesis addresses two dimensions of the debris removal challenge by surveying (a) the number of conjunction events with the current debris population that could be experienced during a typical re-orbit to a super-synchronous disposal orbit, and (b) an autonomous guidance technique required by a low-thrust, tug-based ADR system to properly dispose of GEO objects while preventing collisions with the surrounding derelict population. This is a challenging effort, because contactless ADR concepts in the literature (highlighted further in Chapter 6) are constrained by mN thrust levels, preventing a high-thrust avoidance maneuver if one were necessary to mitigate a collision in the short-term. Therefore, with such low-thrust levels, it is likely necessary to detect upcoming collisions multiple revolutions in advance, to provide the guidance and control system enough lead time to safely adjust the thrust profile of the removal tug. Furthermore, to warrant the cost-effectiveness of such an ADR system, it should be designed with simple-yet-robust autonomy in mind, to minimize human-in-the-loop (e.g., ground intervention) where possible.

Specific research tasks for accomplishing this thesis objective are provided as follows:

(1) Harness TLE data and custom debris propagation tools to quantify how frequently near-miss events occur for a tug-based ADR system during a typical, spiraling re-orbit trajectory from the GEO altitude to a compliant disposal orbit 300 km above.

(2) Develop a simple-yet-robust guidance strategy with the autonomy of the system in mind, to appropriately alter the magnitude and/or direction of the thrust profile to safely mitigate an upcoming conjunction event multiple revolutions in advance.

(3) Evaluate the tradeoff between tug thrust level and detection time for the developed guidance strategy, to assess performance with perfect tug/debris state knowledge.

## 1.4 Research Contributions

The content of this thesis has been primarily drawn from the two lists of publications below, which were independently produced in support of the above thesis research goals.

### 1.4.1 Contributed Journal Publications

Relevant articles submitted, peer-reviewed, and published in scholarly journals are:

(1) Anderson, P. V. and Schaub, H., "Methodology for Characterizing High-Risk Orbital Debris in the Geosynchronous Orbit Regime," *In preparation for publication in Advances in Space Research (Elsevier).*

(2) Anderson, P. V. and Schaub, H., "Conjunction Challenges of Low-Thrust Geosynchronous Debris Removal Maneuvers," *In preparation for publication in Acta Astronautica (Elsevier).*

(3) Anderson, P. V. and Schaub, H., "Longitude-Dependent Effects of Fragmentation Events in the Geosynchronous Orbit Regime," *Acta Astronautica*, Vol. 105, No. 1, 2014, pp. 285-297. doi: `http://dx.doi.org/10.1016/j.actaastro.2014.09.011`

(4) Anderson, P. V. and Schaub, H., "Local Debris Congestion in the Geosynchronous Environment with Population Augmentation," *Acta Astronautica*, Vol. 94, No. 2, 2014, pp. 619-628. doi: http://dx.doi.org/10.1016/j.actaastro.2013.08.023

(5) Anderson, P. V. and Schaub, H., "Local Orbital Debris Flux Study in the Geostationary Ring," *Advances in Space Research*, Vol. 51, No. 12, 2013, pp. 2195-2206. doi: http://dx.doi.org/10.1016/j.asr.2013.01.019

### 1.4.2 Contributed Conference Publications

Relevant articles submitted, accepted, and presented at technical conferences are:

(1) Anderson, P. V., McKnight, D., Di Pentino, F., and Schaub, H., "Operational Considerations of GEO Debris Synchronization Dynamics," *Submitted to the 66th International Astronautical Congress, Jerusalem, Israel, October 2015.*

(2) Anderson, P. V. and Schaub, H., "Methodology for Characterizing High-Risk Orbital Debris in the Geosynchronous Orbit Regime," 25th AAS/AIAA Space Flight Mechanics Meeting, Williamsburg, VA, January 2015.

(3) Anderson, P. V. and Schaub, H., "Conjunction Challenges of Low-Thrust Geosynchronous Debris Removal Maneuvers," 25th AAS/AIAA Space Flight Mechanics Meeting, Williamsburg, VA, January 2015.

(4) Schaub, H., Jasper, L., Anderson, P. V., and McKnight D., "Cost and Risk Assessment for Spacecraft Operation Decisions Caused by the Space Debris Environment," 65th International Astronautical Congress, Toronto, Canada, October 2014.

(5) Jasper, L., Anderson, P. V., and Schaub, H., "Economic and Risk Challenges of Operating in the Current Space Debris Environment," Third Workshop on Space Debris Modeling and Remediation (CNES-HQ), Paris, France, June 2014.

(6) Anderson, P. V. and Schaub, H., "Characterizing Localized Debris Congestion in the Geosynchronous Orbit Regime," 24th AAS/AIAA Space Flight Mechanics Meeting, Santa Fe, NM, January 2014.

(7) Anderson, P. V. and Schaub, H., "Longitude-Dependent Effects of Fragmentation Events in the Geosynchronous Orbit Regime," 24th AAS/AIAA Space Flight Mechanics Meeting, Santa Fe, NM, January 2014.

(8) Anderson, P. V. and Schaub, H., "Local Debris Congestion in the Geosynchronous Environment with Population Augmentation," Sixth European Conference on Space Debris, Darmstadt, Germany, April 2013.

(9) Anderson, P. V. and Schaub, H., "Local Orbital Debris Flux Study in the Geostationary Ring," AIAA/AAS Astrodynamics Specialist Conference, Minneapolis, MN, August 2012.

# Chapter 2

## *Research Goal 1(a)*: Forecasting longitude-dependent congestion at GEO arising from the current debris population

### 2.1 Overview of Research Goal

Using publicly-available tracking data provided by the U.S. Strategic Command, and a classification system published by the European Space Agency,[33] this chapter illustrates a five-year, localized congestion forecast at GEO for large-scale, trackable, and unclassified resident space objects (RSO) with up-to-date two-line element (TLE) sets as of March 2014. Small-scale sources such as explosion and collision events, although treated in Chapter 5, are not considered in this chapter, nor are other debris growth mechanisms, such as ejection of solid rocket motor (SRM) slag or shedding of multi-layered insulation (MLI).[6] The results of this congestion forecast are leveraged to characterize which classes of debris objects contribute the most to longitude-dependent risk levels, globally and over a specified subset of longitude slots. In particular, methodology for identifying the derelicts that contribute the largest percentages to the total risk level accumulated either globally or locally during the forecasting period is presented. For ADR initiatives geared towards slot clean-up at particular longitudes, information such as that determined from debris simulations using a localized congestion metric to evaluate longitude-dependent risk is especially useful in helping to identify which individual objects should be removed to maximize reduction in risk—either globally or across a subset of longitude slots—namely, in the vicinity of the two gravitational wells at 75°E and 105°W, which are dense with operational assets.[2]

The results of this work should therefore be harnessed in tandem with long-term debris prediction studies, such as that performed in Chapter 4, to provide recommendations for architecture and design of potential ADR demonstration missions in the GEO regime. Studies led by the NASA Orbital Debris Program Office use the product of debris mass and probability of collision at a desired epoch as selection criterion for identifying the top ADR targets in the LEO regime.[34] ADR target selection studies for the GEO ring have received far less attention than equivalent ADR target studies for LEO.[34–36] This chapter seeks to begin filling this void in the literature by formulating methodology for identifying the top GEO ADR targets, based on a torus intersection metric and independent of the probability of collision measure often used in conjunction assessment. Note that this torus intersection metric does not claim that these high-risk derelicts might actually collide with specific operational satellites; rather, the methodology presented in this chapter identifies the specific derelicts that contribute the most significant macroscopic risk to the GEO orbit in general.

## 2.2 Current RSO Population at GEO

The RSO population in the GEO ring is classified under a taxonomy used by the European Space Agency's DISCOS database (Database and Information System Characterising Objects in Space).[33] For GEO objects, seven orbit categories are defined to classify the type of orbits for these objects – two controlled classes, one drifting class, three libration classes, and one indeterminate class. Table 2.1 provides a description of this classification system. Note that only uncontrolled debris objects are assumed to contribute to localized congestion in this thesis, as operational GEO assets have the capability to execute dedicated collision avoidance maneuvers if deemed necessary. GEO objects are selected according to the three criteria given in the European Space Agency's *Classification of Geosynchronous Objects* reports:[33]

- Eccentricity smaller than 0.2 ($e < 0.2$)

- Inclination smaller than 70° ($i < 70°$)
- Mean motion between 0.9 and 1.1 revolutions per sidereal day ($0.9 < n < 1.1$)[1]

Table 2.1: Orbit classifications for geosynchronous objects used in this thesis.

| Class | Type | Description |
|---|---|---|
| C1 | Controlled | Longitude/inclination control (E-W/N-S control) |
| C2 | Controlled | Longitude control only (E-W control only) |
| D | Drifting | Circulating above/below/through GEO ring |
| L1 | Librating | Libration about Eastern stable point at 75°E |
| L2 | Librating | Libration about Western stable point at 105°W |
| L3 | Librating | Libration about Eastern and Western stable points |
| IN | Indeterminate | Unknown status (e.g., recent TLE set not available) |

Orbital data is obtained from the publicly-available two-line element (TLE) sets provided by the U.S. Strategic Command (USSTRATCOM).[2] For this study, a reference TLE set obtained on 28 February 2014 is employed; the class distribution for the 1145 objects meeting the above GEO criterion in this TLE set is shown in Figure 2.1. TLE data are provided in the form of "doubly-averaged" Keplerian elements with mean motion instead of semi-major axis,[11] transformed into Cartesian states in the true equator, mean equinox (TEME) frame using SGP-4[37,38] theory.[3] Because of the limited accuracy of TLE sets,[40] these data are not intended for analyses that require highly-accurate orbit prediction capabilities. As the purpose of this research objective is to forecast longitude-dependent congestion upon a macroscopic scale—not on a specialized, satellite-by-satellite basis—the accuracy of these data is sufficient for the scope of this thesis.[4] For high-accuracy applications, multiple TLE sets may be treated as pseudo-observations in an initial orbit determination routine using a filtering algorithm to recover osculating orbits suitable for higher-fidelity propagation.[11]

[1] This mean motion range corresponds to the semi-major axis range of [-2596,3068] km relative to GEO, such that longitudinal drift rates for objects included in the study are at a maximum of ±36° per solar day.
[2] Publicly-available TLE data sets are available for download from `https://www.space-track.org/`
[3] ANSI-C implementation of SGP-4 is available at `http://www.sat.dundee.ac.uk/~psc/sgp4.html`[39]
[4] Numerical justification for using TLE sets to quantify local GEO congestion is provided in Reference 2.

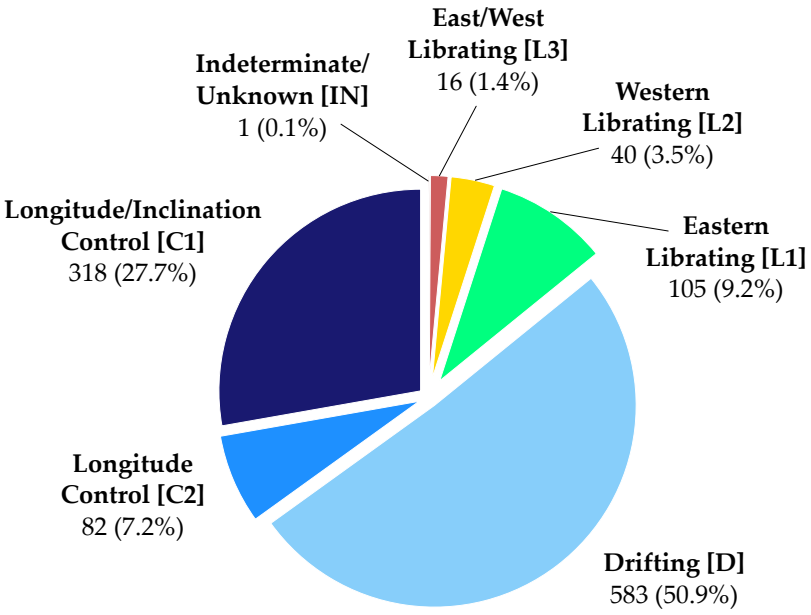


Figure 2.1: Orbit classifications for 28 February 2014 TLE set.

As only objects larger than approximately 0.8-1.0 m in effective diameter are actively tracked at the GEO altitude,[33] only objects at least of this size are considered in this study.[5] Since this research incorporates the trackable, catalogued, and unclassified GEO population with recent TLE data, the findings of this study serve to illustrate a conservative lower bound of the actual debris congestion and risk situation at GEO. This congestion and risk information is then harnessed to identify which large-scale derelicts currently at GEO contribute the most to risk levels across this regime, both globally and in the vicinity of the two gravitational wells. Since risk to operational geostationary satellites is the primary concern of this thesis, debris-debris collision risk among the 745 uncontrolled objects is not treated.

The Eastern librating (L1) and Western librating (L2) RSOs oscillate within the Earth-fixed frame around their respective gravitational wells with a libration period of 816 days at minimum for small amplitudes.[11] Using tabulated data in Reference 33 in tandem with analytic libration theory from Reference 4, a histogram of the libration periods for the 145

[5] USSTRATCOM collects tracking data for GEO with the GEODSS (Ground-Based Electro-Optical Deep-Space Surveillance) and MOTIF (Maui Optical Tracking and Identification Facility) installations, part of the Space Surveillance Network (SSN).[11]

L1/L2 derelicts included in this study is shown in Figure 2.2. The median of this libration period distribution is approximately 2.6 years, such that a 5-year time frame is used for this study to capture two mean cycles of the libration motion. In this manner, bias introduced in both global and localized risk results towards particular classes of debris is minimized. See Appendix A for an overview of libration motion at GEO and why it physically occurs.

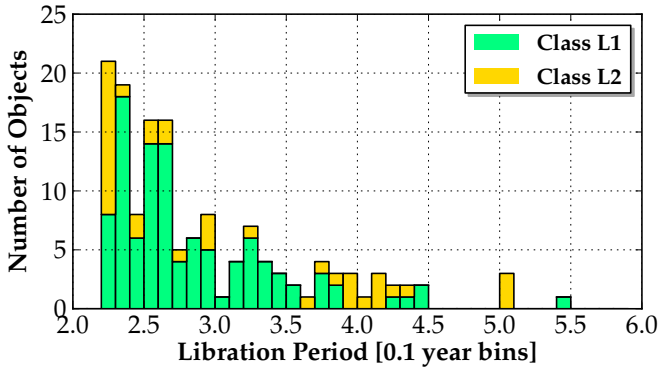


Figure 2.2: Libration periods for L1/L2 objects included in study.

## 2.3 Methodology for Forecasting Longitude-Dependent Congestion at GEO

### 2.3.1 Formulation of Near-Miss Event Metric

Longitude-dependent debris congestion at GEO is investigated by tracking *near-miss events* for each of the GEO longitude slots over a specified forecasting interval, determined by constructing a torus with major radius $r_{\text{GEO}} = 42164$ km and minor radius $\tilde{r}$, partitioned into longitudinal cells of width $\Delta\lambda = 1.0^\circ$ (see Figure 2.3). The minor radius $\tilde{r}$ is the radius of the circular torus cross-section, and provides a means for evaluating debris congestion levels occurring within desired distances of the GEO longitude slots, i.e., a larger minor radius $\tilde{r}$ captures more near-miss events. Furthermore, this torus formulation is a natural choice for counting near-misses for these non-inertial cells, as torus geometry is invariant as seen by both the Earth-centered, inertial frame and Earth-centered, Earth-fixed frame,

in which these longitude slots are stationary.[13]

Near-miss events are detected during propagation of a derelict object by checking for the transversal of this GEO torus boundary at each time step during numerical integration, and between these primary time steps using an interpolation method if higher resolution is desired. Mathematically, a near-miss event occurs if[13]

$$\left(r_{\text{GEO}} - \sqrt{r_X^2 + r_Y^2}\right)^2 + r_Z^2 - \tilde{r}^2 < 0 \tag{2.1}$$

is satisfied, where $(r_X, r_Y, r_Z)^T$ denotes the RSO position vector expressed in Earth-centered inertial (ECI) frame components. The longitude of intersection $\lambda_{\text{CPE}}$ is thus determined as

$$\lambda_{\text{CPE}} = \arctan\left(\frac{r_Y}{r_X}\right) - \alpha_G \tag{2.2}$$

where $\alpha_G$ is the right ascension of Greenwich (a.k.a. Greenwich sidereal time), determined at the current simulation epoch via the well-known sidereal time approximation[38,41]

$$J_0 = 367t_y - \text{floor}\left(\frac{7}{4}\left[t_y + \text{floor}\left(\frac{t_m + 9}{12}\right)\right]\right) + \text{floor}\left(\frac{275t_m}{9}\right) + t_d + 1721013.5 \tag{2.3a}$$

$$T_0 = \frac{J_0 - 2451545}{36525} \tag{2.3b}$$

$$\alpha_{G,0} = 100.4606184 + 36000.77004\, T_0 + 0.000387933\, T_0^2 - 2.583\left(10^{-8}\right) T_0^3 \text{ [deg]} \tag{2.3c}$$

$$\alpha_G = \alpha_{G,0} + 360.98564724\left(\frac{t_h}{24}\right) \text{ [deg]} \tag{2.3d}$$

where current propagation time is expressed with $(t_y, t_m, t_d, t_h)$, corresponding to the year, month, day, and hour (e.g., terrestrial time) of the current simulation epoch. When a torus-intersection is detected via Equation (2.1), the longitude of intersection $\lambda_{\text{CPE}}$ is determined with Equation (2.2), and the total near-miss count for the corresponding cell is advanced. Again, note that because of the convenient invariance of this torus geometry, inertial frame coordinates obtained during numerical integration need not be converted into the rotating Earth-centered, Earth-fixed reference frame to determine longitudinal cell intersections.

To ensure that similar intersection events are not accounted for more than once during propagation—e.g., in the case of repeated intersections occurring over subsequent time

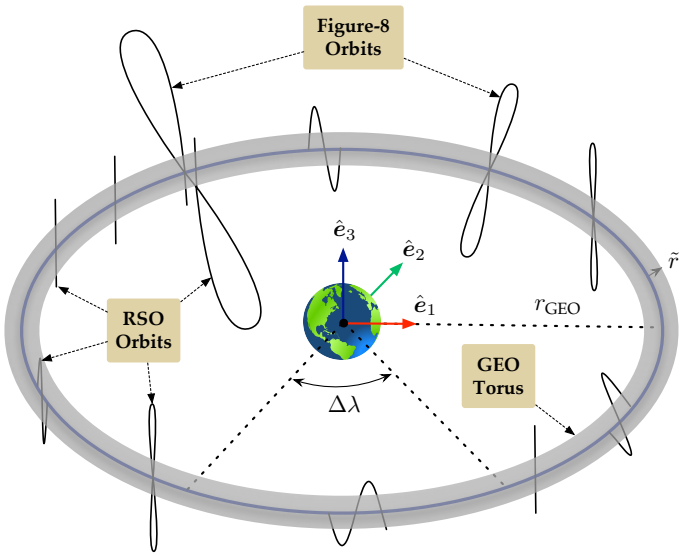


Figure 2.3: GEO torus concept for tracking near-miss events.

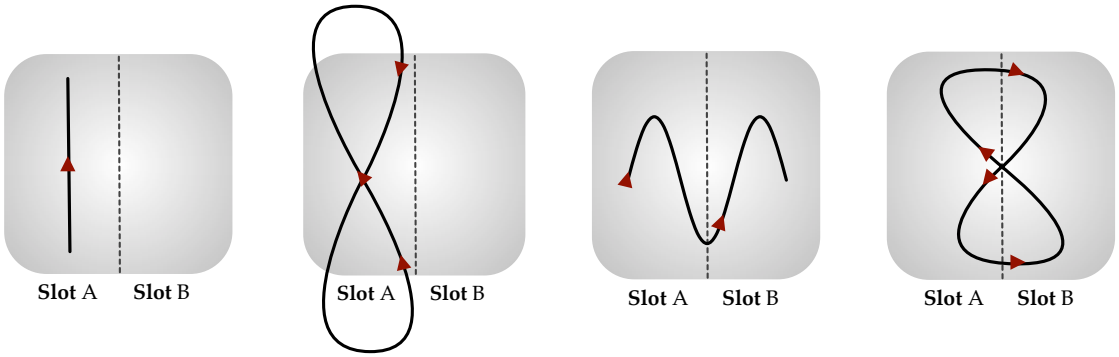


(a) 1 event per cell. (b) 3 events per cell. (c) 1 event per cell. (d) 2 events per cell.

Figure 2.4: Examples of counting logic that eliminates redundancy in intersection checks.

steps—counting logic is employed before any cell intersection counter is updated to screen the event for redundancy. Figure 2.4 illustrates several examples as to how near-miss intersection events are counted during numerical simulations. Relative to an Earth-fixed observer, orbits that reside entirely within a particular torus cell, as depicted in Figure 2.4(a), are counted only once during the specified near-miss tracking interval.[6] If an object exits

[6] Arbitrary near-miss tracking intervals are predefined to catalog intersections in consistent, reoccurring time frames. For this thesis, near-miss events are tracked in intervals of one solar day, such that following each day of propagation, torus cell counts and information for every near-miss occurring over the previous day are output to data files. Torus cell counts are then zeroed to initialize the next near-miss tracking interval.

and later re-enters the same torus cell, however, additional near-miss events are counted following every re-entry, as illustrated in Figure 2.4(b). Furthermore, additional near-miss events are counted if the relative orbit drifts into a neighboring slot during the near-miss tracking interval, such as in Figures 2.4(c)-2.4(d). This counting scheme ensures that near-miss events are evaluated for each of the GEO longitude slots in a logical, consistent, and non-redundant manner over the entirety of the forecasting period. The full algorithm for quantifying near-miss events using the torus intersection metric is provided as follows.[13]

#### 2.3.1.1 Algorithm for Implementation of Torus Intersection Metric

Let $t_i$ be the current propagation epoch of the $i^{\text{th}}$ RSO, and let $t$, $t_{\text{int}}$, and $t_f$ denote integration time, near-miss tracking interval length, and final simulation time, respectively. Define $N_{\text{RSO}}$ as the number of GEO objects extracted from the TLE set, and $N_{\text{CPE}}|_{\lambda_{\text{bin}}}$ as the number of near-miss events for the torus cell indexed by longitude bin $\lambda_{\text{bin}}$. Furthermore, let $\mathcal{C}$ denote the subset of all class C1/C2 objects, and let $\mathcal{D}, \mathcal{L}$, and $\mathcal{I}$ be the subsets of all class D, L1/L2/L3, and IN objects, respectively. Implementation pseudocode is as follows:

**while** $t_i < t_f$ **do**
  **for** $i = 1 \rightarrow N_{\text{RSO}}$ **do**
    Intersection flag $\leftarrow 0$
    Longitude flag $\leftarrow -1$
    **if** $i \in \mathcal{D} \cup \mathcal{L} \cup \mathcal{I}$ **then**
      **while** $t < t_{\text{int}}$ **do**
        Propagate: $t \leftarrow t + \Delta t \Rightarrow \boldsymbol{r}_i = (r_X, r_Y, r_Z)^T$
        **if** $(r_{\text{GEO}} - \sqrt{r_X^2 + r_Y^2})^2 + r_Z^2 - \tilde{r}^2 < 0$ **then**
          $t_h \leftarrow t_i + t/3600$
          Equations (2.3a)-(2.3d) $\Rightarrow \alpha_G$
          $\lambda_{\text{CPE}} = \texttt{atan2}(r_Y, r_X) - \alpha_G$
          $\lambda_{\text{bin}} = \texttt{floor}(\lambda_{\text{CPE}})$
          **if** Intersection flag = 0 || Longitude flag $\neq \lambda_{\text{bin}}$ **then**
            Increment: $N_{\text{CPE}}|_{\lambda_{\text{bin}}} \leftarrow N_{\text{CPE}}|_{\lambda_{\text{bin}}} + 1$

15: Longitude flag $\leftarrow \lambda_{\text{bin}}$
16: **end if**
17: **end if**
18: **if** $(r_{\text{GEO}} - \sqrt{r_X^2 + r_Y^2})^2 + r_Z^2 - \tilde{r}^2 < 0$ **then**
19: Intersection flag $\leftarrow 1$
20: **else**
21: Intersection flag $\leftarrow 0$
22: **end if**
23: **end while**
24: $t_i \leftarrow t_i + t_{\text{int}}$
25: Update RSO fields
26: **else** $(i \in \mathcal{C})$
27: $t_i \leftarrow t_i + t_{\text{int}}$
28: Update $\boldsymbol{r}_i \leftarrow \lambda_i$ maintained
29: Update RSO fields
30: **end if**
31: **end for**
32: Output $N_{\text{CPE}}|_{\lambda_{\text{bin}}} \; \forall \; \lambda_{\text{bin}} \in [0°, 360°)$
33: $N_{\text{CPE}}|_{\lambda_{\text{bin}}} = 0 \; \forall \; \lambda_{\text{bin}} \in [0°, 360°)$
34: **end while**

### 2.3.2 Propagator and Implementation

A custom special perturbations propagator implemented in ANSI-C and parallelized with OpenCL[7] is called to propagate the uncontrolled RSO population forward in time to determine torus intersection events. A lower-fidelity, albeit representative force model for the GEO environment is used for the benefit of dramatically-reduced simulation run times. In this formulation, two-body equations of motion are numerically integrated under $4 \times 4$ EGM-96 gravitation, luni-solar perturbations, and solar radiation pressure (SRP), modeled with the standard cannonball assumption[38] and attenuated via the occultation algorithm

[7] *OpenCL 1.2 Specification* is available from Khronos Group at: `http://www.khronos.org/registry/cl/`.

given in Reference 42. Specifically, the equations of motion for each uncontrolled RSO are

$$\ddot{\boldsymbol{r}} = -\frac{\mu_{\oplus}}{r^3}\boldsymbol{r} + \boldsymbol{a}_{\oplus} + \boldsymbol{a}_{\mathfrak{D}} + \boldsymbol{a}_{\odot} + \boldsymbol{a}_{\text{SRP}} \tag{2.4}$$

where the first term denotes two-body acceleration, $\boldsymbol{a}_{\oplus}$ is the perturbation due to the non-sphericity of Earth, $\boldsymbol{a}_{\mathfrak{D}}$ and $\boldsymbol{a}_{\odot}$ are the third-body perturbations from the Moon and Sun, respectively, and $\boldsymbol{a}_{\text{SRP}}$ is the SRP perturbation. Solar pressure is modeled using the inverse-square diffusion formulation of the solar luminosity $L_{\odot} \approx 3.839 \times 10^{26}$ J/s, with coefficient of reflectivity $c_r \equiv 1.5$ and a GEO-representative area-to-mass ratio $A_{\odot}/m = 0.04$ m$^2$/kg.[8] This GEO forcing model is in agreement with the results of Reference 32, which ranks the importance of incorporating various environmental perturbations in GEO forcing models for debris analysis over time scales ranging from 1 week to 10 years. Appendix A provides a detailed description of the specific computations for each perturbation in Equation (2.4).

In higher-fidelity force models, coordinate transformations between Earth-fixed and Earth-inertial frames use high-accuracy Earth orientation parameters (EOP) to account for precession, nutation, and polar motion – software suites such as the SPICE toolkit can be used to perform these intensive coordinate transformations.[9] In this parallel propagator, however, a lower-fidelity transformation that accounts strictly for $z$-axis rotation by Greenwich sidereal time is used for increased speeds at run time. Further, instead of extracting Moon and Sun vectors from JPL's DE-421 ephemerides, this routine uses lower-precision formulas for the geocentric positions of these bodies, given in the *Astronomical Almanac*.[44] Reference 2 provides verification of this lower-fidelity force model by comparing localized congestion results over a 5-year period with those obtained under higher-fidelity forcing.

The propagator uses an eighth-order, predictor-corrector Gauss-Jackson integrator[45] initialized with the Prince-Dormand 8(7) algorithm for integrating the equations of motion in Equation (2.4). During initial propagation of the uncontrolled debris field to the fore-

[8] Reference 43 indicates that this ratio is representative for operational and derelict satellites at GEO; this area-to-mass ratio is thus used in the SRP computation for all large-scale derelicts considered in this chapter.

[9] The SPICE toolkit is available from NASA/JPL at: `http://naif.jpl.nasa.gov/naif/toolkit.html`.

cast start date, and during near-miss event detection over the prediction span, a ten-minute time step is specified for sufficient fidelity in capturing near-miss events. To increase resolution without significantly increasing run times, a Lagrange interpolation method is used to detect torus intersections in one-minute increments between primary ten-minute steps.

### 2.3.3 Risk Functions for GEO-Relative Position and Velocity

To begin identifying the particular uncontrolled derelicts responsible for the highest levels of both global and localized risk in the GEO regime, the GEO-relative position and velocity for an object at torus intersection must be translated into a risk metric that can be applied to categorize and rank the GEO debris population based upon levels of globally- and locally-contributed risk. It is important to note that the number of near-miss events alone for each object over the duration of the forecasting period is an insufficient measure for evaluating both global and localized risk, since the proximity of these near-miss events to the GEO altitude—and the GEO-relative velocity with which these near-misses occur—are not explicitly taken into account. For this study, each near-miss event is assigned a level of combined risk that is based upon the GEO-relative state of the responsible debris object at the time of torus intersection. Position and velocity risk factor functions are employed to individually weight (a) *how close* the object comes to the GEO altitude, and (b) *how fast* the object is traveling relative to local GEO orbit velocity.

Specifically, the position and velocity risk functions selected for this study are:

$$R_r(r) = \left(\frac{\tilde{r} - r}{\tilde{r}}\right)^2, \quad 0 \leq r \leq \tilde{r} \tag{2.5}$$

$$R_v(v) = 1 - e^{-3v/\bar{v}}, \quad v \geq 0 \tag{2.6}$$

where $r$ and $v$ are the GEO-relative position and velocity magnitudes, respectively. The position risk factor function in Equation (2.5) is of quadratic form, rising smoothly from $R_r(\tilde{r}) = 0$ at the torus boundary to $R_r(0) = 1$ at the GEO altitude. The velocity risk function in Equation (2.6) is of an exponential form, selected to rapidly saturate to $R_v(v) \to 1$

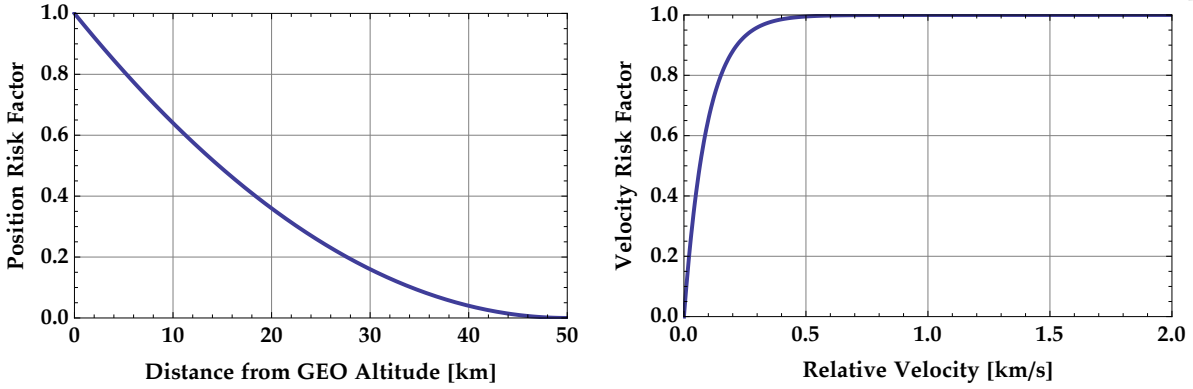


(a) Quadratic form used for position risk factor. (b) Exponential form used for velocity risk factor.

Figure 2.5: Functions selected for computing combined risk factor of each near-miss event.

when the GEO-relative velocity surpasses a defined threshold, beyond which collision velocities are considered catastrophic. In this manner, all relative velocities beyond this critical threshold are weighted nearly equally – collisions with uncontrolled derelicts traveling with catastrophic relative speeds have serious and likely mission-impacting consequences, regardless of where these speeds lie above the critical threshold. The position and velocity risk factor functions defined in Equations (2.5)-(2.6) are illustrated in Figure 2.5.

From Equation (2.1), the GEO-relative position magnitude $r$ is given by

$$r = \sqrt{\left(r_{\text{GEO}} - \sqrt{r_X^2 + r_Y^2}\right)^2 + r_Z^2} \tag{2.7}$$

The GEO-relative velocity is computed by differencing the object's inertial velocity vector at torus intersection with the local, two-body orbit velocity vector of a hypothetical GEO satellite stationed at the longitude of intersection, expressed in inertial frame components:

$$\boldsymbol{v}_{\text{GEO}} = \left[-\sqrt{\frac{\mu_\oplus}{r_{\text{GEO}}}}\sin(\lambda_{\text{CPE}} + \alpha_G), \sqrt{\frac{\mu_\oplus}{r_{\text{GEO}}}}\cos(\lambda_{\text{CPE}} + \alpha_G), 0\right]^T \tag{2.8}$$

The GEO-relative velocity is scaled by the "time-constant-like" parameter $\bar{v}$ in the velocity risk factor function, such that when $v = \bar{v}$, the risk function $R_v(\bar{v}) = 1 - e^{-3} \approx 0.950$ and begins saturating.[10] For this study, $\bar{v}$ is derived from the NASA Standard Breakup Model

[10] The parameter $n$ in a more general function of the form $1 - e^{-nv/\bar{v}}$ can be selected to adjust the value of the velocity risk at $v = \bar{v}$ explicitly, i.e., for a desired velocity threshold risk $R_v(\bar{v})$, then $n = -\ln(1 - R_v(\bar{v}))$.

as the relative speed threshold above which collisions are "catastrophic," assuming equivalent masses for the target and impactor:[46]

$$\tilde{E}_p^* = \frac{1}{2}\bar{v}^2 \rightarrow \bar{v} = \sqrt{2\tilde{E}_p^*} \approx 0.2828 \text{ km/s} \tag{2.9}$$

where $\tilde{E}_p^* \equiv 40$ kJ/kg is the defined specific energy threshold for a catastrophic collision.[11] After the GEO-relative position and velocity for the near-miss event are computed, the corresponding risk factor functions in Equations (2.5)-(2.6) are evaluated, and the *combined risk factor* given by the product $R_r(r)R_v(v)$ is evaluated. This combined risk factor for the near-miss event is on the unit interval [0,1] and provides a metric for gauging how "threatening" the near-miss is for a hypothetical GEO satellite stationed on the longitude of intersection. Under this metric, uncontrolled derelicts that closely pass the GEO altitude—and have catastrophic-collision-inducing relative speeds when doing so—will, in general, have a higher combined risk for near-miss events detected during propagation. Note that both close proximity and sufficient relative speed must be present in order for a near-miss event to be considered high-risk under this metric, e.g., higher-speed events near the torus boundary and lower-speed events closer to the GEO altitude are both deweighted in the combined risk factor.

It is important to note that object mass is not considered in this combined risk factor, as it is used in the NASA Orbital Debris Program Office's studies to identify top active debris removal (ADR) targets for the LEO regime.[34] Mass information is not included within the publicly-available TLE data source harnessed in this study. If approximate mass information is available, an auxiliary mass function can be used to weight the combined risk factor, or each object's mass can be in-built by using a kinetic energy of the form $\frac{1}{2}mv^2$ in Equation (2.6) directly, i.e., by replacing relative speed risk with kinetic energy risk. With these modifications, the combined risk for more massive derelicts will be emphasized, in a similar manner that probabilities of collision are scaled by LEO object mass in Reference 34.

## 2.4 Results of Longitude-Dependent Congestion and Risk Forecast at GEO

As a precursor to identifying which classes of GEO debris contribute the most to both global and localized risk levels in this regime, a 5-year macroscopic congestion forecast is performed with the minor radius $\tilde{r} = 50$ km, using the baseline object population in the 28 February 2014 TLE set. Controlled assets (C1/C2) are assumed to maintain their specified longitude slots, while the 745 uncontrolled objects extracted from this set are propagated forward in time and incorporated in the near-miss study. Note that this simulation is only investigating the congestion generated by the current debris population over a 5-year time frame. Nominal population growth, fragmentation events, solid rocket motor (SRM) slag, multi-layered insulation (MLI) shedding, and other debris growth mechanisms treated in Reference 6, for example, are not treated in this simulation. The objective for this research is to investigate which classes of large-scale derelicts currently at GEO contribute the most to risk levels across this regime, and determine the highest-risk derelicts in these classes.

### 2.4.1 Localized Congestion, Velocity, and Risk Results

The localized debris weather forecast at GEO for the 5-year analysis period is shown in Figure 2.6(a), which illustrates the number of near-miss events per day at 50 km for each of the longitude slots at GEO. Accumulation of uncontrolled derelicts around the gravitational wells at 75°E and 105°W is well-known, and discussed in References 47 and 48, for example. This is particularly troublesome, because operational GEO satellites are typically inserted into longitude slots near these debris-critical longitudes,[2] and the probability of collision in the vicinity of these gravitational wells is seven times larger than in surrounding regions at GEO.[1,8] From Figure 2.6(a), controlled assets in the longitude slots neighboring the two gravitational wells are subject to 4-8 close calls per day at a miss distance of 50 km – this is a factor of four increase over less congested longitudes (e.g., Atlantic and Pacific Oceans), which experience a maximum of 1-2 near-misses per day at 50 km. Note

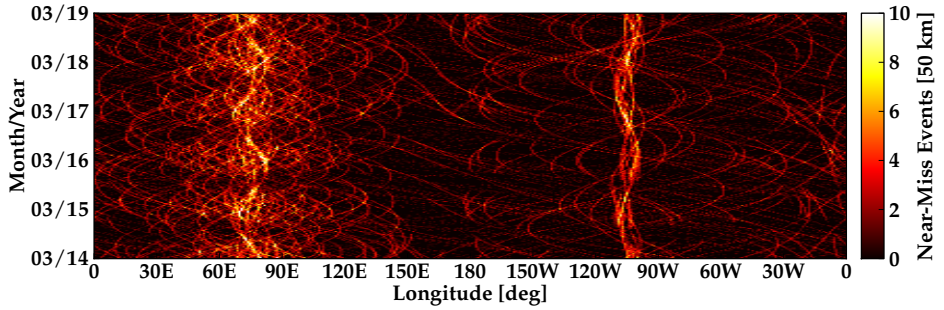


(a) Near-miss events per day at 50 km during 5-year forecasting period.

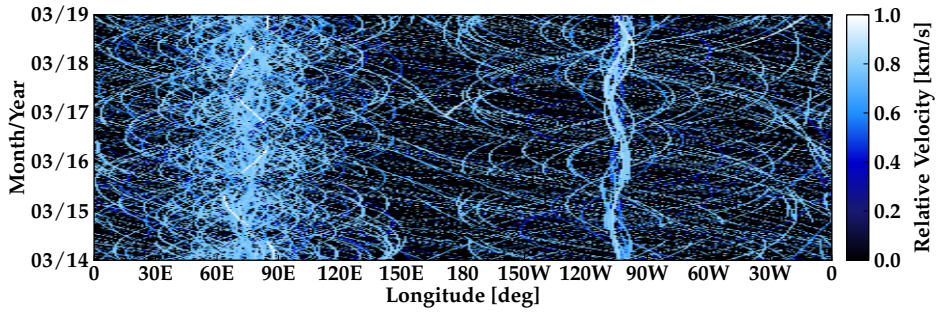


(b) Maximum relative velocities of near-miss events during forecasting period.

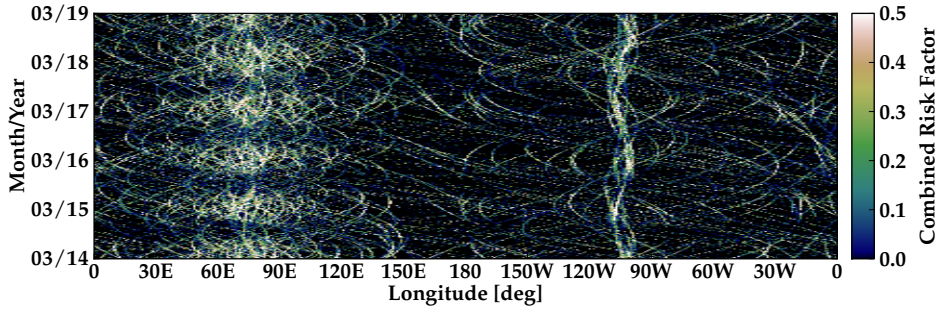


(c) Maximum combined risk factor of near-miss events during forecasting period.

Figure 2.6: Three portraits of longitude-dependent congestion in the GEO ring, generated by the large-scale, trackable, and unclassified GEO debris population on 28 February 2014.

that the number of near-misses during the forecasting period for any longitude slot is not equivalent to the probability of collision $\mathcal{P}_c$ used in operational conjunction assessment.[11]

Regions of increased near-miss events in Figure 2.6(a) are a result of (1) multiple objects with single near-miss events per day, (2) single objects with multiple near-miss events per day, or (3) a combination of both of these possibilities, in which overlapping Earth-relative

[11] For discussions as to the impact of the debris population on longitude-dependent probability of collision at GEO, see Reference 1.

debris motions (cf. Figure 2.3) induce the spatially-dense regions observed in Figure 2.6(a).

Individual orbit class contributions to the localized congestion forecast in Figure 2.6(a) are illustrated in Figure 2.7 for drifting (D), Eastern librating (L1), Western librating (L2), and East/West librating (L3) objects. The near-linear traces exhibited by the class D objects in Figure 2.7(a) demonstrate the longitudinal drift magnitudes of the responsible objects – traces with a positive slope indicate eastward drift (below GEO altitude), and traces with a negative slope indicate westward drift (above GEO altitude). Curvilinear traces of objects classified as drifting in Reference 33 indicate that these objects are now exhibiting librating class behavior, or were misclassified when initially catalogued due to insufficient tracking data, uncertainties in the orbit determination process, force model approximations, etc.[40] As anticipated, increased densities of near-miss events per day near the gravitational wells result from dominant contributions by the class L1 and L2 objects, shown in Figures 2.7(b)-2.7(c) and illustrative of the libration period distribution in Figure 2.2. Class L3 behavior in Figure 2.7(d) results from a longitude of abandonment near the unstable equilibrium at 165°E – initial potential energy in this region is large enough to propel the derelict through the first gravitational well, over the "potential hill" at 15°W, and through the second gravitational well before reversing the direction of motion in longitude to complete the cycle.[11]

It is interesting to highlight that although the number of near-miss events for a particular longitude slot may be relatively benign on a daily basis, the relative velocities—and combined risk factors—with which these near-misses occur may not be. Figure 2.6(b) illustrates worst-case GEO-relative velocities experienced in each 1° longitude slot throughout the forecasting period. This relative velocity forecast shows that even though a longitude slot could experience 1-2 near miss events per day, the maximum relative speed for these near-miss events could be upwards of ∼0.6 km/s (approximately 1340 mph).[12] In general,

[12] Relative velocities are lower in the GEO regime when compared to LEO, since (a) orbit velocity is lower at the GEO altitude, and (b) objects at GEO are, in general, orbiting in the same direction.[32] Compared to the 2009 Iridium-33/Cosmos-2251 collision, which occurred at a relative velocity of upwards of 24,600 mph (∼11 km/s)[49] at LEO, 1340 mph at GEO is a much smaller—but still mission-impacting—collision velocity.

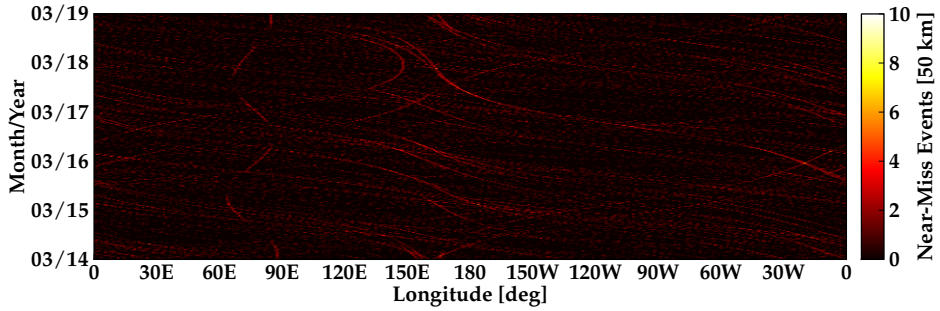


(a) Contribution of drifting (D) objects to near-miss event forecast.

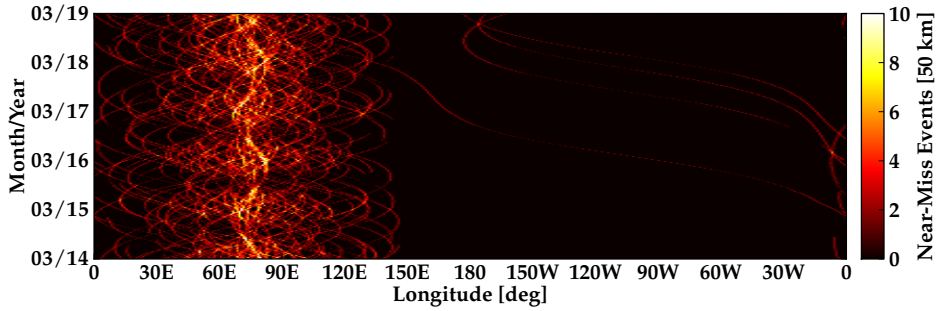


(b) Contribution of Eastern librating (L1) objects to near-miss event forecast.

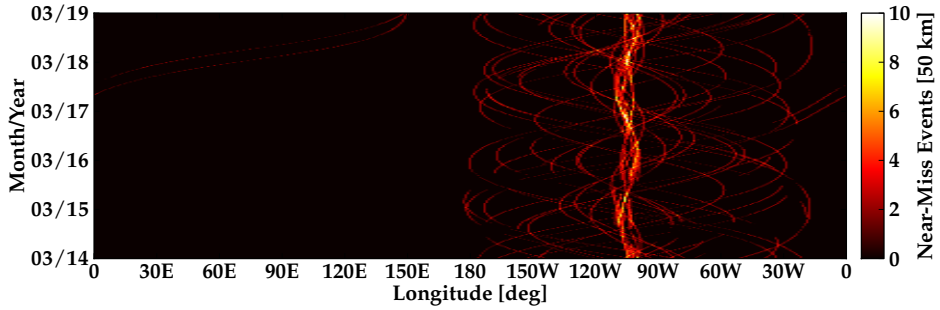


(c) Contribution of Western librating (L2) objects to near-miss event forecast.

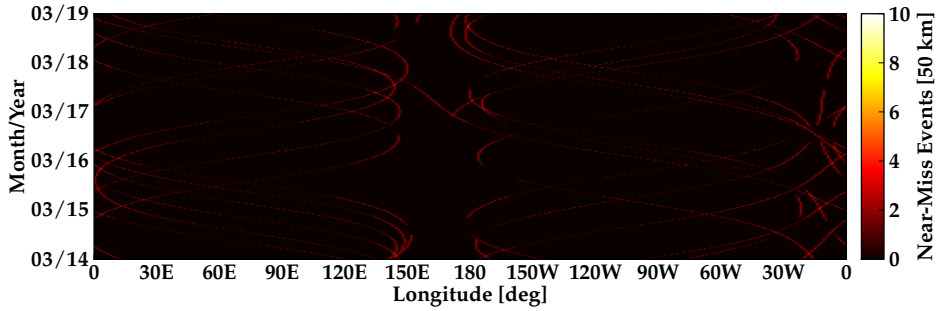


(d) Contribution of East/West librating (L3) objects to near-miss event forecast.

Figure 2.7: Contributions of individual orbit classes to localized congestion at GEO.

higher relative speeds can be attributed to uncontrolled derelicts with higher inclinations, such that relative speeds at the ascending and descending nodes are increased with respect to equatorial GEO orbit velocity, which does not have an out-of-plane component for geostationary orbits. Nonzero eccentricity also serves to increase relative speeds at the nodes, such that near-miss events with higher-inclination and higher-eccentricity objects are more hazardous to operational assets, that is, these objects exhibit higher combined risk factors.

Figure 2.6(c) shows worst-case combined risk factors experienced in each longitude slot throughout the forecasting period. Higher combined risk levels are visible in the vicinity of the gravitational wells, exhibiting a banding phenomenon driven by once-yearly oscillations in the magnitude of the eccentricity vector, induced by the SRP perturbation.[3] In Section 2.5.2, this combined risk forecast is used to validate an identified subset of high-risk derelicts, that is, the combined risk in the neighborhoods of the gravitational wells is attenuated if this high-risk subset of objects is omitted from the 5-year congestion forecast.

Figure 2.8 illustrates the effect of various force model contributions on the combined risk factor forecast in Figure 2.6(c). Figure 2.8(a) provides the resulting risk forecast under 4×4 gravitation only; luni-solar perturbations are then applied in Figure 2.8(b), and SRP is applied in Figure 2.8(c). The inclusion of luni-solar perturbations changes the phase of the L2 congestion band centered on the Western well, and SRP gives rise to the annual banding phenomenon mentioned above. Figure 2.8 corroborates the results of Reference 32, which ranks the importance of incorporating various environmental perturbations in GEO force models for debris analysis over time scales ranging from 1 week to 10 years. For the 5-year time scale used in Figure 2.8, third-body perturbations and SRP are assigned "very high" and "high" importance, respectively.[32]

### 2.4.2 Time-Averaged Congestion, Velocity, and Risk Results

In addition to tracking the number of near-miss events at 50 km occurring daily for each longitude slot over this 5-year analysis period (cf. Figure 2.6), it is of interest to assess

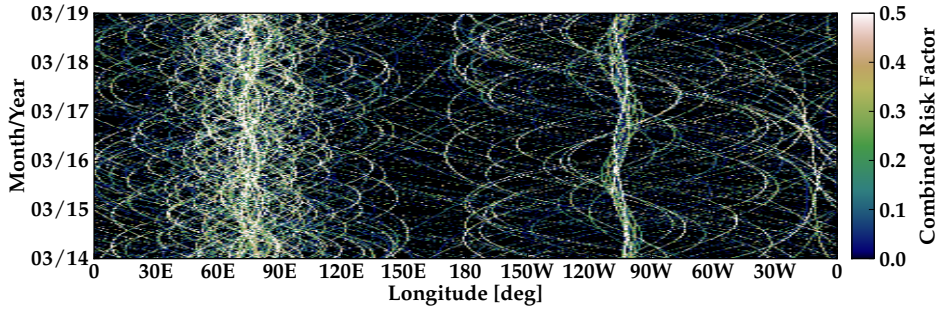


(a) Maximum combined risk (4×4 gravitation only).

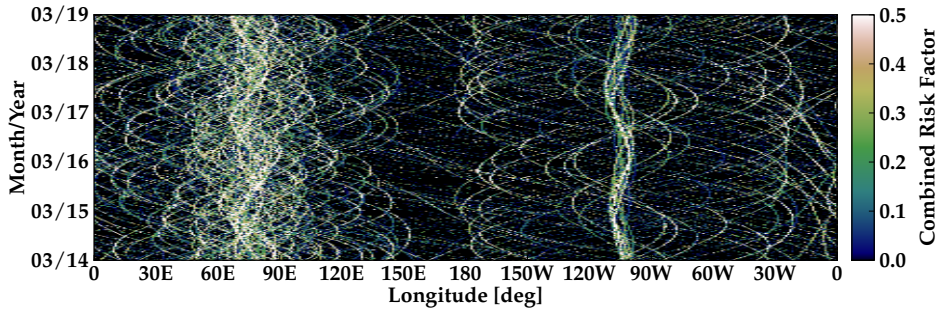


(b) Maximum combined risk (4×4 gravitation and luni-solar perturbations).

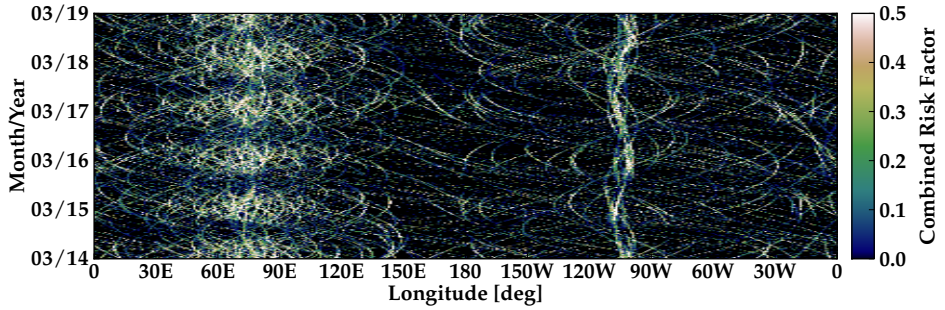


(c) Maximum combined risk (4×4 gravitation, luni-solar perturbations, and SRP).

Figure 2.8: Contributions of dominant GEO perturbations to combined risk forecast.

which classes of uncontrolled objects contribute the most to longitude-dependent congestion, for purposes of recommending which types of objects to remove if a particular longitude slot is to be cleared of debris. Figure 2.9(a) provides the average number of near-miss events per day contributed by objects of each uncontrolled class considered in this study. Longitude slots neighboring the debris-critical gravitational wells at 75°E and 105°W are subject to 3-4 close calls per day on average, while less congested longitude slots experience only 0.5 close calls (at 50 km) per day on average. Congestion contributions in the regions

encompassing the Eastern and Western gravitational wells are dominated by class L1 and L2 objects, which oscillate in the Earth-fixed frame around these stable equilibria with the libration periods shown in Figure 2.2. In addition, the drifting (class D) objects contribute an approximate 0.25 near-misses per day across the entirety of the GEO ring, thereby generating the "background noise" observed in the debris congestion forecast in Figure 2.6(a). Interestingly, the near-miss contributions for class D objects peak at the unstable equilibrium longitudes 165°E and 15°W – the longitudinal rate $\dot{\lambda}$ induced by the $J_{2,2}$ harmonic is at a minimum at these locations,[4] causing drifters to linger longer at these longitudes.[1]

In summary of the localized congestion, relative velocity, and combined risk results shown for the 5-year analysis period in Figure 2.6, Figures 2.9(b)-2.9(d) show the average number of near-miss events at 50 km per day, beneath or above various relative position, relative speed, and combined risk factor thresholds, respectively. For example, the Eastern well at 75°E experiences an average of four near-misses per day at 50 km over the forecast (Figure 2.9(a)), two of which are beneath 40 km in proximity to the GEO ring (Figure 2.9(b)) and greater than 0.75 km/s in relative velocity (Figure 2.9(c)). Although Figure 2.9(c) illustrates that approximately all of the near-miss events occurring at 75°E are above the catastrophic velocity threshold in Equation (2.6), the combined risk summary in Figure 2.9(d) indictates that only one near-miss event per day in this longitude slot is above a combined risk factor of 0.2 on average. The position risk function in Equation (2.5) is de-weighting the risk of these higher-velocity encounters – Figure 2.9(b) shows that the majority of these near-miss events are occurring above 25 km in proximity to GEO, a distance beyond which the position risk function in Equation (2.5) is beneath 0.25 in magnitude (cf. Figure 2.5(a)).

For purposes of slot safety assessment, it is important to consider not only the mean of the number of near-miss events occurring daily for each longitude slot, but the standard deviation for these distributions, as well. Figure 2.10 illustrates the $1\sigma$ number of near-miss events at 50 km for each longitude slot and risk threshold provided in Figure 2.9(d), highlighting the spread of these slot-specific distributions (i.e., generated by tracking the num-

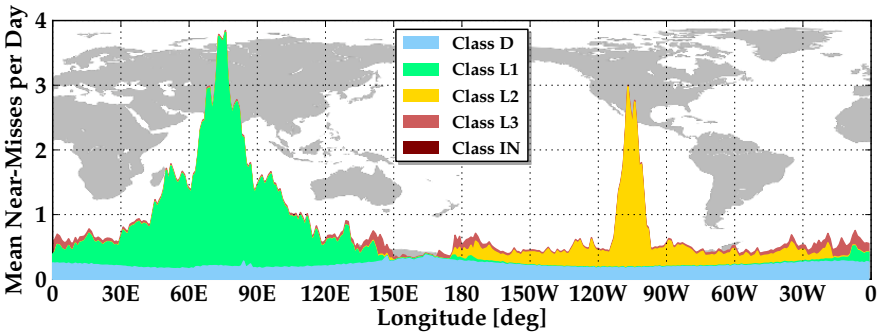


(a) Average number of near-miss events per day at 50 km by object class.

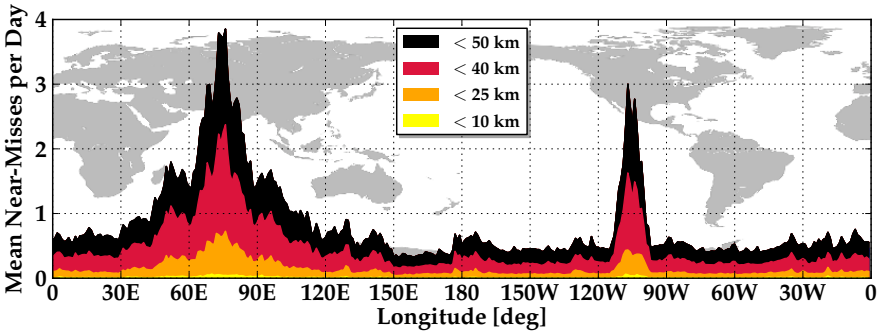


(b) Average number of near-miss events per day with position thresholds.

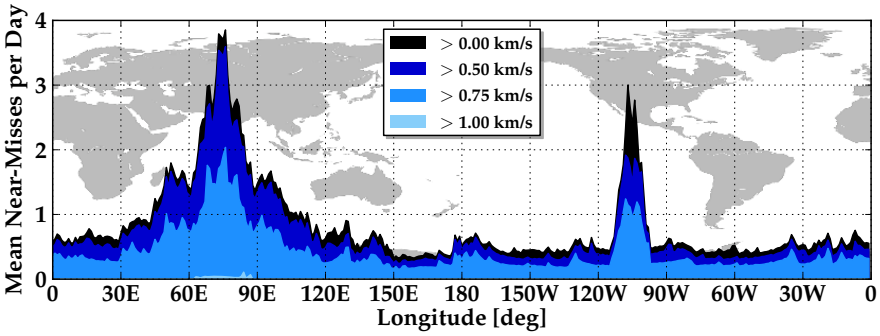


(c) Average number of near-miss events per day with velocity thresholds.

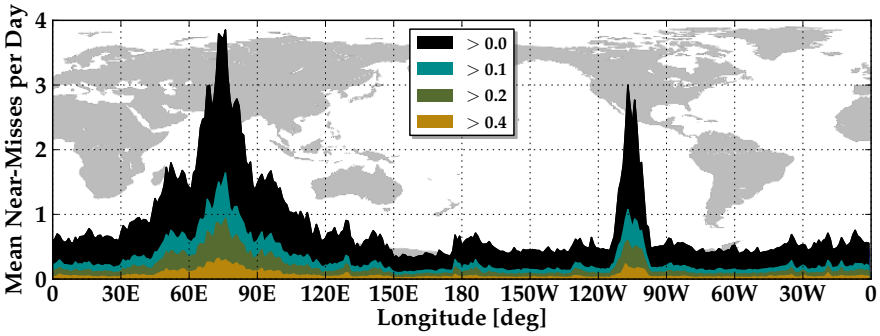


(d) Average number of near-miss events per day with risk factor thresholds.

Figure 2.9: Average number of near-miss events per day at 50 km for each longitude slot, by orbit class and above or beneath various relative position, velocity, and risk thresholds.

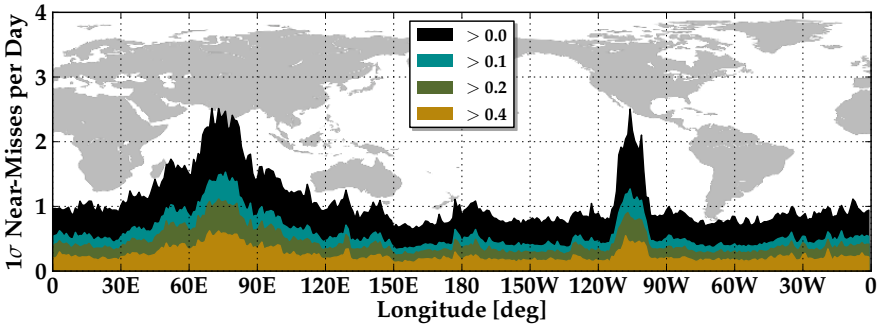


Figure 2.10: Standard deviation of near-miss events per day with risk factor thresholds.

ber of near-misses within each longitude slot, above each risk threshold, on each day over the forecast). Near-miss distributions around the two gravitational wells have a larger $1\sigma$ spread for all risk thresholds, indicating that these congested regions can experience many more near-misses on a given day than the 5-year average of approximately 3-4 near-misses per day shown in Figure 2.9(d). In particular, the near-miss distribution for 75°E extends from 0-13 near-misses per day at 50 km during the 5-year analysis period, highlighting the insufficiency of the time-averaged mean in Figure 2.9(d) in forecasting slot-specific trends.

### 2.4.3 Timing of Near-Miss Events

In addition to the number of near-miss events per day for each GEO longitude slot, and the relative velocities and combined risks with which these near-miss events occur, it is critical to study the time of day at which these near-misses occur. Reference 1 indicates that the equatorial crossing windows of the GEO debris population are synchronized such that collision hazard is both episodic and predictable. To illustrate this concept, Figure 2.11 provides the distribution mean and $1/2/3\sigma$ corridors for the local time of all near-misses occurring across the GEO ring over each day of the first year of the forecasting period, for near-miss events during the ascending (south-to-north) equatorial pass in Figure 2.11(a), and descending (north-to-south) equatorial pass in Figure 2.11(b). The tight distributions shown in Figure 2.11 demonstrate that there exist two predictable windows relative to local

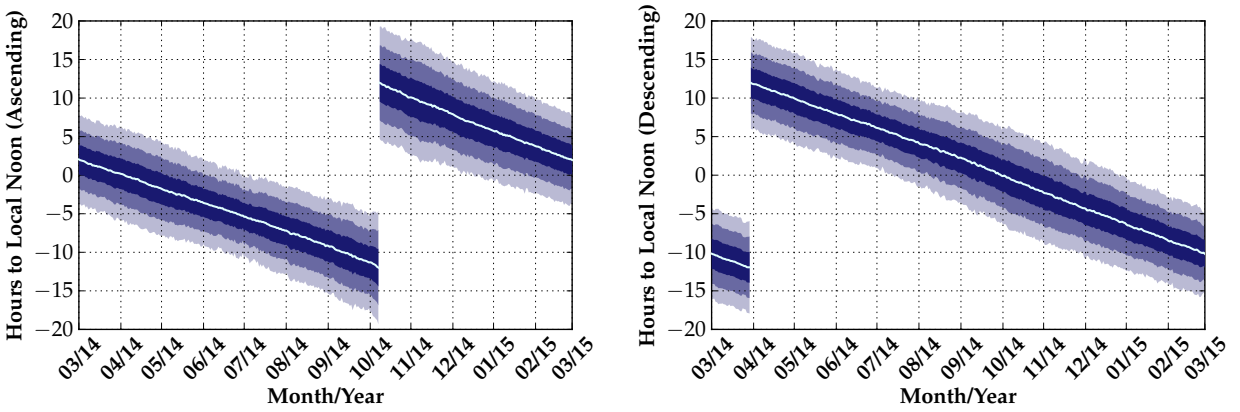


(a) Equator crossing time distribution (ascending). (b) Equator crossing time distribution (descending).

Figure 2.11: Equatorial crossing times for the synchronized debris population at GEO are episodic and dependent upon time of year.[1] Shaded swaths illustrate $1/2/3\sigma$ corridors.

noon during which observational coverage of GEO can be maximized, regardless of longitudinal location around GEO. The equatorial crossing windows vary nearly linearly over the course of the year, and the ascending/descending windows occur 12 hours apart from one another at any point in the year. These time-varying equatorial crossing windows are the Earth-fixed representation of the well-known GEO "pinch points," which are currently static in inertial right ascension and declination coordinates, and are harnessed to optimize sensor tasking for space-based space surveillance (SBSS) systems.[50,51]

Relative to an Earth-fixed observer, the collective motion of the GEO debris population is qualitatively similar to a transverse wave[1] – this motion arises from a clustering in right ascension of the ascending node, driven by luni-solar perturbations dominant at the GEO altitude. The equatorial crossing windows shown in Figure 2.11 are a physical manifestation of this phenomenon, and can be leveraged for maximizing observational coverage of the GEO ring, anomaly correlation, and forecasting of potential conjunction events. With this knowledge, the threat of near-miss events with higher combined risk factors can be mitigated through increased coverage of the desired slot during the episodic windows relative to local noon shown in Figure 2.11. An in-depth discussion of GEO "pinch point"

evolution and its impact on operational geostationary satellites is provided in Chapter 3.

### 2.4.4 Near-Miss Overlap Comparison

To investigate how well the near-miss event metric performs in forecasting longitude-dependent congestion trends at GEO in the short-term, an overlap study is conducted. In this comparison, two five-year predictions are generated – one using the debris population from the 31 August 2011 TLE set, and the other using the population in the 31 August 2013 TLE set. To ensure that controlled objects in the TLE set from 2011 are not misclassified as uncontrolled debris if using the 2014 issue of *Classification of Geosynchronous Objects*,[33] the 2012 issue is instead used for classifying the 2011 TLE population. Thus, for the 31 August 2011 TLE set, 705 of 1053 GEO objects are uncontrolled, and for the 31 August 2013 TLE set, 742 of 1126 are uncontrolled. Each population is propagated forward for five years, and the localized congestion trends in the September 2013-2016 overlapping period are compared.

Figure 2.12 illustrates the results of this overlap comparison by providing the difference in slot-dependent near-miss events per day detected between the 2011 and 2013 predictions. A negative difference indicates that the 2011 propagation *under*-predicted future

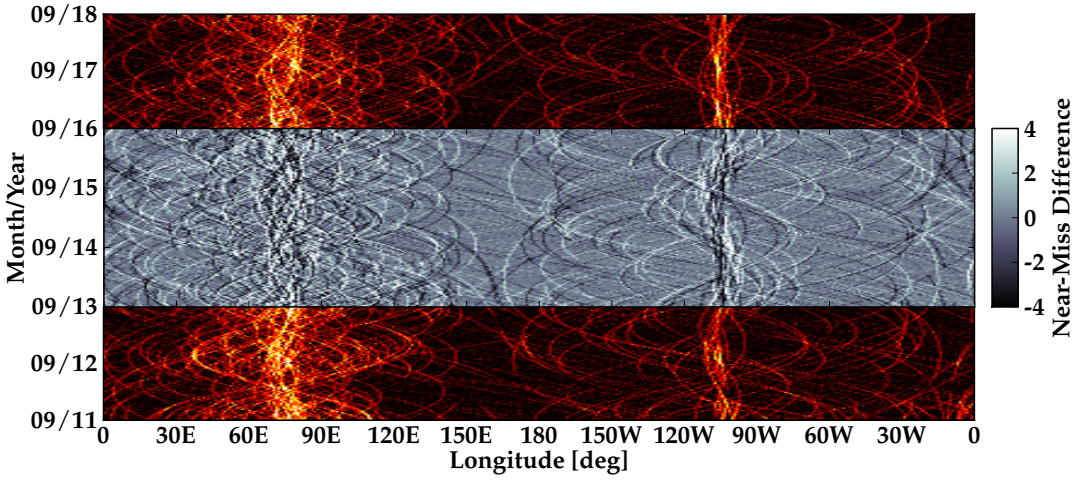


Figure 2.12: Comparison of two overlapping congestion forecasting periods.

localized congestion; conversely, a positive difference indicates that the 2011 propagation *over*-predicted future congestion trends (i.e., more near-miss events per day in a particular longitude slot than forecasted using the 2013 debris population). As shown in Figure 2.12, near-miss differences during the overlapping period vary widely, and are most significant in the vicinity of the gravitational wells. Large congestion differences in certain longitude slots at particular times can be attributed to one or more of the following error sources:

- *Errors in initial conditions.* Publicly-available TLE data sets used to derive the initial conditions of the debris population prior to propagation are not intended for high-accuracy applications, and corresponding uncertainty information for each object is not provided. Even in the absence of propagation errors, a state vector extracted from a later TLE set will differ from the prediction derived from an earlier TLE set due to measurement noise and errors inherent to the orbit determination process.

- *Errors in propagation.* As stated in Section 2.3.2, the propagator used in this chapter includes a lower-fidelity, representative force model for the GEO environment, in which gravity terms larger than fourth degree and order are truncated. Thus, this force model does not provide a high-accuracy description of GEO dynamics, such that unmodeled/mismodeled perturbations combine with initial condition errors to augment slot-dependent congestion differences observed in the overlap period.

- *Errors in population prediction.* Under-prediction occurs when objects listed as controlled in the 2011 population are classified as uncontrolled in the 2013 population. These differences also occur because the debris population increased by 37 objects between the 31 August 2011 and 2013 TLE populations, and the 2011 propagation does not reflect this increase in the number of debris, leading to under-prediction.

Ultimately, the widely-varying congestion differences in Figure 2.12 indicate that the combination of recent TLE sets, shorter prediction spans, up-to-date object classifications, and

higher-fidelity propagation are required to reduce the uncertainties in the number of near-miss events per day experienced in arbitrary longitude slots at arbitrary times. Such high-accuracy congestion predictions could be leveraged to inform GEO operators as to specific times of year—in addition to the specific times of day shown in Figure 2.11—during which conjunction events may be more likely, due to an increase in the number of objects passing through their longitude slots ("storm monitoring" in the debris weather forecast analogy).

## 2.5 Identifying Highest-Risk Debris Objects at GEO

To begin identifying the classes of uncontrolled debris objects in the GEO regime that contribute the most to longitude-dependent congestion—and more importantly, longitude-dependent risk—the results of the 5-year congestion and risk forecast shown in Figure 2.6 are partitioned by debris orbit class. Figure 2.13(a) gives the breakdown of the percentage that each uncontrolled derelict class contributes to the total number of near-miss events at 50 km occurring globally over the entire 5-year analysis period. Figure 2.13(b) provides a breakdown of the percentage that each class contributed to the total combined risk for the near-miss events accumulated globally during the 5-year analysis period. These pie charts are interesting when compared alongside the TLE orbit class breakdown in Figure 2.1. Although drift objects constitute 50.9% of the large-scale, trackable RSO population at GEO, they only contribute 26.3% of the near-miss events at 50 km detected during the forecasting period, which collectively account for 23.8% of the global risk accumulated during this period. Librating objects, on the other hand, contribute a dominating 73.1% of the number of near-misses—accounting for 76.1% of the global accumulated risk—even though these objects collectively make up a mere 14.1% of the RSO population at GEO (that is, 27.1% of the uncontrolled debris population in the 28 February 2014 TLE set). Of significant interest for ADR initiatives are the 105 Eastern librating (L1) derelicts that contribute 49.9% to the globally accumulated risk over the 5-year forecast, that is, 14.1% of the GEO debris population is collectively responsible for nearly 50% of globally accumulated risk around GEO.

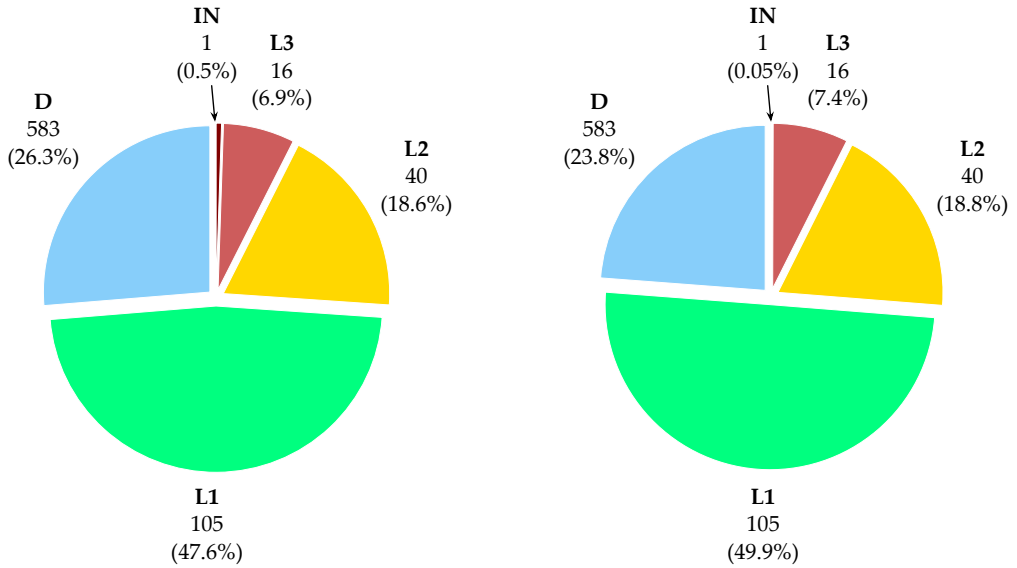


(a) Breakdown of near-miss events.

(b) Breakdown of combined risk factor.

Figure 2.13: Breakdown of number of near-misses and combined risk accumulated globally around the GEO ring during the 5-year forecasting period, by responsible debris class.

### 2.5.1 Global Risk Accumulation Metric

Although Figure 2.13 gives a congestion and risk breakdown by debris class, it does not illustrate the contribution of individual objects within each orbit class to the combined risk globally accumulated during the forecasting period. One measure for identifying the highest-risk objects at GEO is the *global risk accumulation metric*, which utilizes the risk contribution of individual objects to the total risk globally accumulated around GEO during the forecasting period to rank the derelict population from highest to lowest risk level. To compute the global accumulated risk, the combined risk factors for all near-miss events occurring in all longitude slots throughout the 5-year forecasting period are summed into a grand total. Then, the risk contributions of the near-miss events for individual objects to this grand total are applied to sort these derelicts into order of descending global risk contribution. Table 2.2 lists the top 10 highest-risk objects from the 28 February 2014 TLE set, identified using this global risk accumulation metric. Notably, all of these objects are de-

funct payloads that are from the L1/L2 librating classes.[13] The semi-major axes for these high-risk derelicts are within ±15 km of the GEO radius at the beginning of the forecasting period, and the inclinations for these derelicts range from 13°-16° relative to the equatorial plane. Collectively, these top 10 derelicts are responsible for 9.39% of the global combined risk factor accumulated around the GEO ring during the 5-year forecast in Figure 2.6(c).

Table 2.2: Highest-risk derelicts at GEO, based on global risk accumulation (unweighted).

| Rank | Object Name | COSPAR | Class | Country | Slots Affected | % Risk |
|---|---|---|---|---|---|---|
| 1 | Aurora 1 | 1982-105A | L2 | USA | 97-110°W | 0.968% |
| 2 | Cosmos 1366 | 1982-044A | L1 | USSR/Russia | 65-84°E | 0.965% |
| 3 | ASC 1 | 1985-076C | L2 | USA | 79-130°W | 0.961% |
| 4 | Raduga 1-2 | 1990-116A | L1 | USSR/Russia | 49-100°E | 0.958% |
| 5 | Insat 1C | 1988-063A | L1 | India | 57-92°E | 0.949% |
| 6 | GStar 1 | 1985-035A | L2 | USA | 100-108°W | 0.947% |
| 7 | GStar 3 | 1988-081A | L2 | USA | 101-107°W | 0.931% |
| 8 | Telstar 4A | 1993-077A | L2 | USA | 97-113°W | 0.917% |
| 9 | Raduga 26 | 1990-112A | L1 | USSR/Russia | 55-94°E | 0.899% |
| 10 | Cosmos 1897 | 1987-096A | L1 | USSR/Russia | 49-100°E | 0.898% |
| | | | | | **TOTAL** | **9.39%** |

It is critical to emphasize that this top 10 ranking is in effect for the next 5 years only, since it harnesses combined risk factor data for near-miss events detected during a 5-year forecasting period. A well-known effect of luni-solar perturbations on GEO objects is long-term cyclical precession of the orbital plane, in which the inclination of initially equatorial objects rises to 15° and back with a period of approximately 53 years.[3] Thus, in 26 years, the objects listed in Table 2.2 will be in nearly equatorial orbits, such that the relative speeds of these objects at the nodes are decreased. As a result, the combined risk contributions for the near-miss events triggered by these currently highest-risk derelicts will diminish—and successively increase again—over the course of this 53-year inclination cycle (Chapter 3).

Note that although the position and velocity relative to GEO at torus intersection are

[13] As a first-order condition for stable point capture improves as proximity to the GEO radius decreases,[4] this is an intuitive result. Librating objects have semi-major axes that are closer to the synchronous altitude, such that relative position risk in Equation (2.5) is higher, in general, for the near-miss events triggered by objects from these librating classes.

translated into a combined risk factor using Equations (2.5)-(2.6), the longitude at which the near-miss event occurs is not taken into account in the present risk formulation. Since operational GEO satellites are most often inserted into longitude slots in the neighborhood of the gravitational wells,[2] it is useful to consider weighting the combined risk factor by the longitude at which the near-miss event occurs. In this manner, higher-risk near-misses occurring near higher-density longitudes are emphasized, and conversely, higher-risk near-misses at longitudes with low densities of operational assets are de-weighted. An example of one such longitude weighting function is drawn from the wrapped-normal probability density function fit to past, present, and projected satellite longitude data in Section 4.2.[2] This weighting function (illustrated in Figure 2.14) amplifies the risk experienced in longitude slots covering the United States and the Eurasian region, and reduces risk factors over the Atlantic and Pacific Oceans, where operational satellite densities are at a minimum.

Table 2.3 lists the top 10 highest-risk objects from the 28 February 2014 TLE set, identified using the global risk accumulation metric with longitudinal weighting applied. The first column provides the rank for each object under longitudinal weighting, and the number of places that these objects rose or fell in the unweighted top 10 ranking in Table 2.2 as a result. The emphasis of the Eastern well over the Western well (cf. Figure 2.14) increases the ranking of Eastern librating (class L1) objects in the ranked population – Aurora 1, the highest-risk L2 object in the unweighted top 10 ranking, falls three places in the weighted top 10 ranking. Furthermore, two L2 payloads from Table 2.2—ASC 1 and Telstar 4A—fall out of the top 10 ranking completely when longitudinal weighting is applied. Collectively, the top 10 objects under longitudinal weighting are responsible for 11.53% of the total combined risk factor accumulated around GEO during the 5-year forecast, a higher percentage than the 9.39% collectively contributed by the top 10 objects in the unweighted ranking.

To summarize the effect of the global risk accumulation metric in identifying objects with the highest cumulative risk over the analysis period—that is, the objects that consistently come close to the GEO altitude at consistently high relative velocities—Figure 2.15(a)

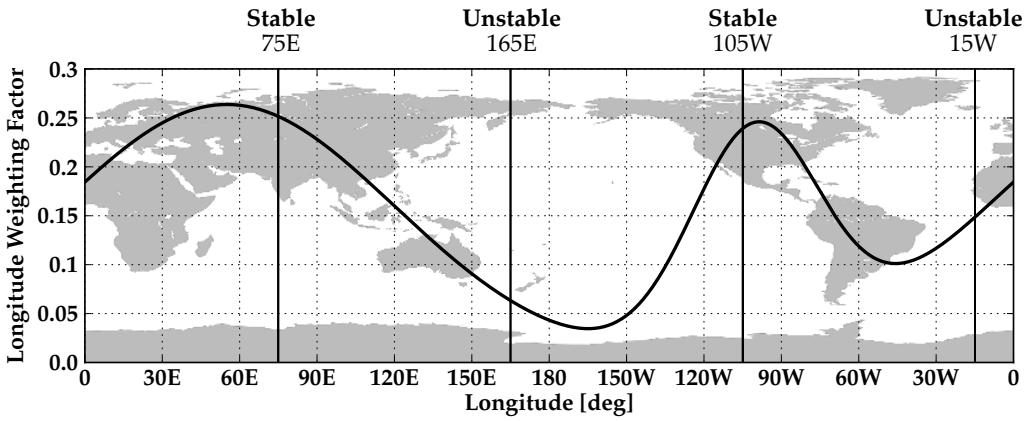


Figure 2.14: Longitude weighting function based upon operational satellite densities.[2]

Table 2.3: Highest-risk derelicts at GEO, based on global risk accumulation (weighted).

| Rank | Object Name | COSPAR | Class | Country | Slots Affected | % Risk |
|---|---|---|---|---|---|---|
| 1 (↑1) | Cosmos 1366 | 1982-044A | L1 | USSR/Russia | 65-84°E | 1.226% |
| 2 (↑3) | Insat 1C | 1988-063A | L1 | India | 57-92°E | 1.198% |
| 3 (↑1) | Raduga 1-2 | 1990-116A | L1 | USSR/Russia | 49-100°E | 1.183% |
| 4 (↓3) | Aurora 1 | 1982-105A | L2 | USA | 97-110°W | 1.168% |
| 5 (↑1) | GStar 1 | 1985-035A | L2 | USA | 100-108°W | 1.149% |
| 6 (↑1) | GStar 3 | 1988-081A | L2 | USA | 101-107°W | 1.131% |
| 7 (↑2) | Raduga 26 | 1990-112A | L1 | USSR/Russia | 55-94°E | 1.125% |
| 8 (↑2) | Cosmos 1897 | 1987-096A | L1 | USSR/Russia | 49-100°E | 1.117% |
| 9 (↑3) | Cosmos 1961 | 1988-066A | L1 | USSR/Russia | 68-82°E | 1.117% |
| 10 (↑3) | Luch 1-1 | 1995-054A | L1 | USSR/Russia | 72-77°E | 1.116% |
| | | | | | **TOTAL** | **11.53%** |

gives contributed percent of global accumulated risk factor as a function of top percent of the ranked debris population, with and without longitudinal weighting. Recalling that the debris population is ranked in order of descending global risk contribution, Figure 2.15(a) shows that 60% of the derelicts (453 objects) do not contribute any risk to the accumulated total, i.e., near-miss events for these derelicts are not triggered over the 5-year forecasting period. Without longitudinal weighting, the top 70 ranked objects are collectively responsible for 50% of global risk experienced during the forecasting period. Under longitudinal weighting, this cumulative trend line becomes steeper, such that the top 59 ranked objects

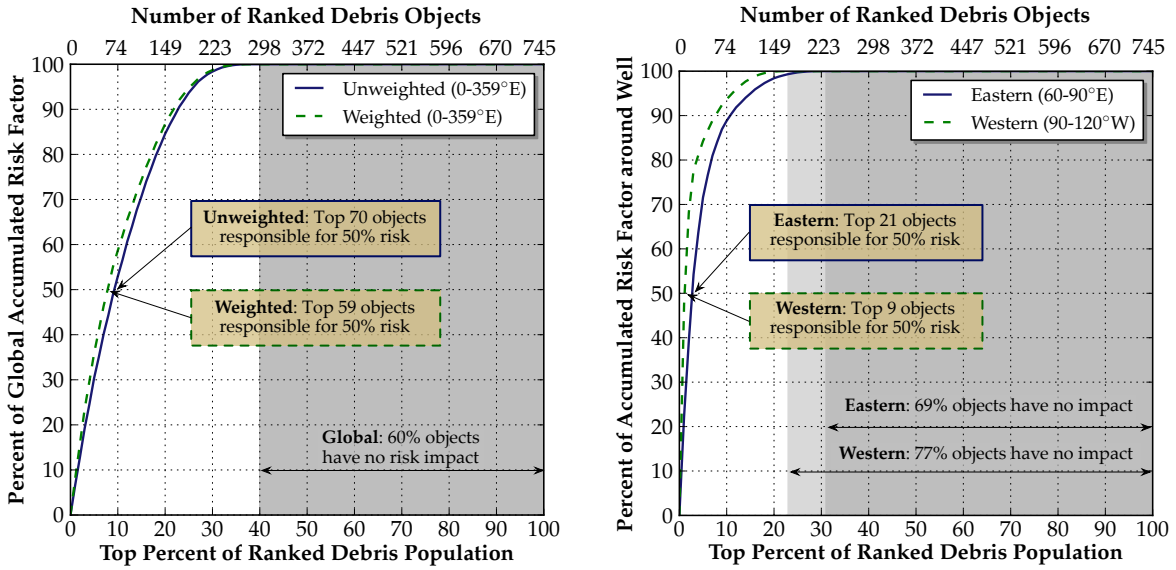


(a) Summary of global accumulated risk at GEO. (b) Summary of local accumulated risk at GEO.

Figure 2.15: Percent of accumulated risk total as a function of top percent of ranked debris population, which highlights accumulated risk contributions from high-ranking subsets.

are responsible for 50% of global accumulated risk. Comparing Tables 2.2-2.3, this results from increased risk contributions for the top ranked objects under longitudinal weighting.

### 2.5.2 Local Risk Accumulation Metric

If identifying the derelicts that contribute the highest accumulated risk to a particular subset of GEO longitude slots is desired, the *local risk accumulation metric* can be evaluated. In contrast to the global accumulation metric, which sums the combined risk factors for all near-miss events occurring across all longitude slots during the analysis period, local risk accumulation uses the sum of combined risk for only those near-miss events occurring in a subset of longitude slots during the analysis period. The local risk accumulation metric is useful for identifying the objects that contribute the highest cumulative risk in the vicinity of the two debris-critical gravitational wells. Tables 2.4-2.5 delineate the top 10 highest-risk contributors to the total accumulated risk over $\pm 15^\circ$ longitude intervals centered upon the Eastern and Western gravitational wells, respectively. Note that these 10 ranked objects in

Table 2.4: Highest-risk debris objects near Eastern gravitational well, based on local risk accumulation on [60,90°E]. Shaded rows indicate objects that are both globally high-risk (that is, included within the unweighted top 10 ranking in Table 2.2) and locally high-risk.

| Rank | Object Name | COSPAR | Class | Country | Slots Affected | % Risk |
|---|---|---|---|---|---|---|
| 1 | Cosmos 1366 | 1982-044A | L1 | USSR/Russia | 65-84°E | 3.636% |
| 2 | Cosmos 1961 | 1988-066A | L1 | USSR/Russia | 68-82°E | 3.290% |
| 3 | Luch 1-1 | 1995-054A | L1 | USSR/Russia | 72-77°E | 3.279% |
| 4 | SIRIO 1 | 1977-080A | L1 | Italy | 72-77°E | 3.115% |
| 5 | Comstar 4 | 1981-018A | L1 | USA | 69-80°E | 3.094% |
| 6 | Cosmos 2133 | 1991-010A | L1 | USSR/Russia | 67-82°E | 2.971% |
| 7 | Raduga 12 | 1983-028A | L1 | USSR/Russia | 63-85°E | 2.921% |
| 8 | Raduga 14 | 1984-016A | L1 | USSR/Russia | 61-87°E | 2.637% |
| 9 | Cosmos 2085 | 1990-061A | L1 | USSR/Russia | 67-82°E | 2.504% |
| 10 | Raduga 26 | 1990-112A | L1 | USSR/Russia | 55-94°E | 2.490% |
| | | | | | **TOTAL** | **29.94%** |

Table 2.4 contribute 29.94% of the total risk accumulated in [60°E, 90°E] during the 5-year period, while the 10 ranked objects in Table 2.5 contribute 57.54% of the risk accumulated in [90°W, 120°W] during this period. This has significant implications for ADR initiatives seeking to attenuate longitude-dependent risk in the vicinity of the Western well, as almost 60% of the combined risk accumulated over this region of GEO is attributed to the top 10 objects in Table 2.5 alone. Note again that this localized risk measure is not associated with the probability of collision $\mathcal{P}_c$ metric commonly used in conjunction assessment, and thus should not be treated as equivalent with this statistical metric over any analysis time frame.

Figure 2.15(b) shows percent contributed to the accumulated risk around each well as a function of the top percent of the ranked debris population. From this chart, 69% of derelicts (515 objects) do not contribute to accumulated Eastern well risk, and 77% of derelicts (574 objects) do not contribute to accumulated Western well risk. As a result, these cumulative trend lines for the local accumulated risk in the vicinity of the gravitational wells in Figure 2.15(b) are steeper than those for the globally accumulated risk in Figure 2.15(a). In particular, the top 21 highest-risk derelicts near the Eastern well—and the top 9 highest-risk objects near the Western well (cf. Table 2.5)—are responsible for 50% of the localized

Table 2.5: Highest-risk debris objects near Western gravitational well, based on local risk accumulation on [90,120°W]. Shaded rows indicate objects that are both globally high-risk (that is, included within the unweighted top 10 ranking in Table 2.2) and locally high-risk.

| Rank | Object Name | COSPAR | Class | Country | Slots Affected | % Risk |
|---|---|---|---|---|---|---|
| 1 | Aurora 1 | 1982-105A | L2 | USA | 97-110°W | 8.215% |
| 2 | GStar 1 | 1985-035A | L2 | USA | 100-108°W | 8.037% |
| 3 | GStar 3 | 1988-081A | L2 | USA | 101-107°W | 7.902% |
| 4 | Telstar 4A | 1993-077A | L2 | USA | 97-113°W | 7.780% |
| 5 | GOES 3 | 1978-062A | L2 | USA | 99-109°W | 5.449% |
| 6 | LES 8 | 1976-023A | L2 | USA | 97-111°W | 5.364% |
| 7 | LES 9 | 1976-023B | L2 | USA | 99-111°W | 4.821% |
| 8 | ASC 1 | 1985-076C | L2 | USA | 79-130°W | 3.630% |
| 9 | NATO IIB | 1971-009A | L2 | USA | 102-108°W | 3.218% |
| 10 | Solidaridad 1 | 1993-073A | L2 | Mexico | 100-111°W | 3.124% |
| | | | | | **TOTAL** | **57.54%** |

risk observed in the 30° longitude regions centered on each gravitational well, respectively.

To show how removal of the top contributing objects in Tables 2.4-2.5 attenuates localized risk in the vicinity of the gravitational wells over the forecasting period, Figure 2.16 provides the mean number of near-miss events per day at 50 km above various combined risk levels, with the full GEO debris population in the 28 February 2014 TLE (Figure 2.9(d)), with the top 5 derelicts in Tables 2.4-2.5 removed (Figure 2.16(a)), and with all 10 derelicts in Tables 2.4-2.5 removed (Figure 2.16(b)). As Figure 2.16 illustrates, removal of the highest cumulative risk objects in the vicinity of the gravitational wells serves to attenuate localized risk in these critical regions. In particular, Figure 2.16(b) illustrates that removal of the 10 derelicts in Table 2.5 not only generates a ∼50% reduction in the mean number of near-miss events occurring around the Western well, but nearly eliminates any near-miss events with combined risk factors greater than 0.4 during the five-year forecasting period.

### 2.5.3 Absolute Worst-Case Risk Metric

The global and local risk accumulation metrics use the sum of the combined risk factors for near-miss events detected across all longitude slots—or a defined subset thereof—

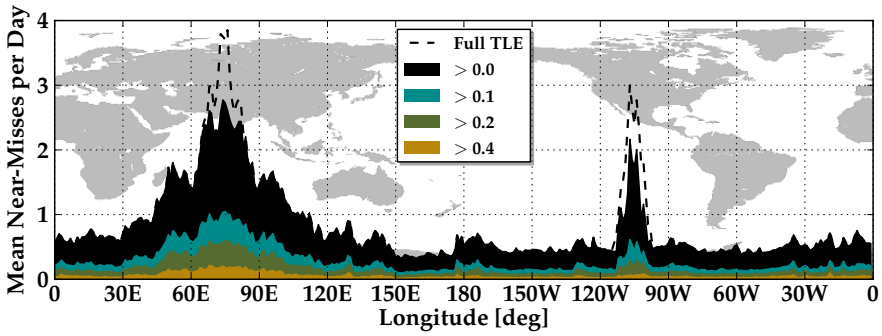


(a) Mean number of near-misses with risk factor thresholds (top 5 removed).

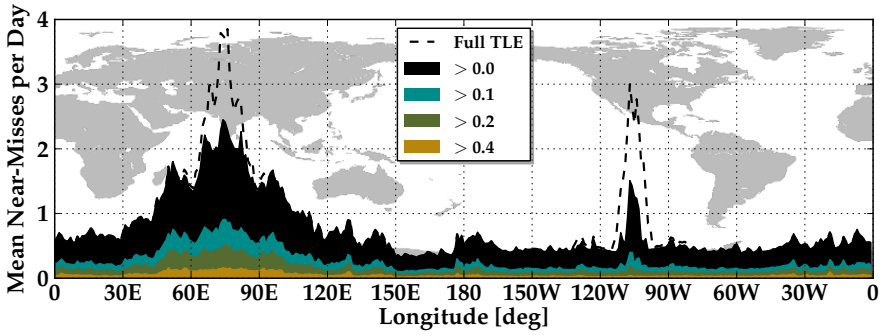


(b) Mean number of near-misses with risk factor thresholds (top 10 removed).

Figure 2.16: Removal of highest-risk debris objects (Tables 2.4-2.5) from 28 February 2014 TLE attenuates localized risk for operational assets positioned near the gravitational wells.

over the forecasting period. Though these two measures are useful for identifying the GEO debris objects responsible for the highest levels of *cumulative* risk experienced either globally or locally at GEO, these metrics do not guarantee that the derelicts responsible for the highest *absolute* risk events will be identified in the ranking scheme. Thus, instead of ranking the debris population by individual risk contribution to a globally or locally accumulated risk total, the *absolute worst-case risk metric* ranks these debris objects by the maximum single-event risk factor each object contributed over the duration of the forecasting period.

Table 2.6 compares the top 5 globally highest-risk objects, identified via (a) the global accumulation metric (cf. Table 2.2), and (b) the absolute worst-case metric. Although risk contributions for the accumulated risk subset are the highest of the population, the worst-case risk events for these objects are not as severe as the worst-case events for the absolute

risk subset. Conversely, the absolute risk subset captures the highest single-event risks observed during the analysis period, but the cumulative risk contributions for these objects are far beneath the contributions of the accumulated risk subset. Comparing the number of near-misses for the accumulated risk subset with the number of near-misses for the absolute risk subset (cf. Table 2.6), this is largely a consequence of the number of events that the derelicts in each subset are responsible for over the duration of the forecasting period.

Table 2.6: Comparison between top five highest-risk objects, based on two ranking criteria.

| | Rank | Object Name | COSPAR | Class | Events | Contribution | Worst Risk |
|---|---|---|---|---|---|---|---|
| Accumulated | 1 | Aurora 1 | 1982-105A | L2 | 3666 | 0.968% | 0.886 |
| | 2 | Cosmos 1366 | 1982-044A | L1 | 3668 | 0.965% | 0.952 |
| | 3 | ASC 1 | 1985-076C | L2 | 3593 | 0.961% | 0.929 |
| | 4 | Raduga 1-2 | 1990-116A | L1 | 3400 | 0.958% | 0.911 |
| | 5 | Insat IC | 1988-063A | L1 | 3568 | 0.949% | 0.884 |
| Absolute | 1 | Syncom 2 | 1963-031A | D | 1753 | 0.438% | 0.993 |
| | 2 | IUS stage 2 | 1991-054D | L3 | 1293 | 0.264% | 0.990 |
| | 3 | LES 9 | 1976-023B | L2 | 2443 | 0.568% | 0.981 |
| | 4 | Raduga 7 | 1980-081A | L2 | 1960 | 0.311% | 0.980 |
| | 5 | Satcom 3R | 1981-114A | D | 2121 | 0.511% | 0.979 |

As the longitude interval applied for local risk accumulation decreases in length, the percent contribution and worst risk differences between the accumulated risk and absolute risk subsets are amplified, i.e., the worst single-event risk for the highest accumulated risk object in a single longitude slot at GEO could be significantly smaller than the worst single-event risk in that slot for the highest absolute risk object. Therefore, depending upon the objectives for a particular ADR initiative—that is, whether the effort is geared towards reducing cumulative or absolute risk in a particular subset of longitude slots—two different methodologies are presented to identify the highest-risk target objects for either objective.

## 2.6 Conclusions from Research Goal

In this chapter, forecasting localized debris congestion in the GEO ring is performed to determine how many near-miss events at 50 km occur upon a daily basis for each of the

GEO longitude slots over a 5-year analysis period. The GEO-relative position and velocity at torus intersection for each near-miss event are translated into a combined risk factor that gauges how threatening the near-miss is for a hypothetical GEO satellite positioned at the longitude of intersection. Three methods for identifying the highest-risk debris objects at GEO are presented to establish a framework for determining the top ADR targets at GEO. Two methods use the contribution to a combined risk total, accumulated either globally or over a subset of longitude slots, to rank the debris population from highest to lowest risk; the third method considers maximum single-event risk as the metric for ranking derelicts.

Simulation results show that the librating class objects—especially those of the Eastern librating class—are the most responsible for both global and localized risk levels, especially in longitude slots surrounding the two gravitational wells at 75°E and 105°W. In the vicinity of the Eastern well, the top 21 ranked objects account for 50% of the accumulated risk in this region over the 5-year forecasting period, and in the vicinity of the Western well, the top 9 ranked objects are responsible for 50% of locally-accumulated risk. Therefore, the results of this chapter have important implications for ADR initiatives aimed at attenuating orbit debris risk, either globally or locally, across the GEO ring. Removal of the top 10 highest cumulative risk objects by the Western well leads to a 50% reduction in the mean number of near-miss events per day occurring in this region, and nearly eliminates all near-miss events in this region occurring with critical risk factors—those that could potentially warrant evasive action by operators. This chapter serves to illustrate localized, longitude-dependent congestion arising from the current GEO debris population, investigate which classes of debris objects are most responsible for congestion contributions, and ultimately, spearhead a dialogue concerned with identifying highest-risk GEO debris for purposes of ADR target selection in this regime.

## 2.7 Continuing Research Questions

For continuing research in this area, the following research questions are of interest:

(1) The torus minor radius $\tilde{r} = 50$ km is used in this chapter as an approximate upper bound at which precise conjunction assessment could potentially be considered in the GEO regime. How does this radius compare with the threshold distance—and probability of collision—below and above which GEO operators plan and execute a dedicated or multi-purpose avoidance maneuver to reduce debris collision risk? Can this information be leveraged to estimate a $\Delta v$ budget from a daily near-miss event average (Figure 2.9) forecasted for the operational longitude slot of interest?

(2) The near-miss event metric and longitude-dependent congestion results presented in this chapter illustrate inhomogeneity of asset-debris conjunction risk at the GEO altitude – debris-debris collision risk, however, is not addressed. Could particular objects not ranked highly under global risk accumulation still be considered high-risk, inasmuch as these objects consistently make close approaches with neighboring debris? Can such "environment criticality" be incorporated into risk rankings?

(3) Can the combined risk factor developed in this chapter for ranking the debris population be further refined to take into account other factors of interest for ADR target selection, such as mass, debris-debris conjunction potential, or attitude rates?

# Chapter 3

## *Research Goal 1(b)*: Investigating the synchronization of the GEO debris population

### 3.1 Overview of Research Goal

Visualizations of the GEO debris population from the slot-relative perspective of the Earth-centered, Earth-fixed frame demonstrate that the collective once-daily motion of this population is similar to a transverse wave that circulates around GEO with a period of one sidereal day.[1] Thus, daily latitude cycles for uncontrolled objects neighboring one another in longitude are not, in general, out-of-phase. Figure 3.1, which provides the distribution of the 28 February 2014 TLE population in longitude/latitude coordinates at four different times during 01 March 2014, shows this correlation in the latitude cycle – as time advances, the peak and trough of this transverse "debris wave" shift westward linearly in longitude. As will be shown in this chapter, apparent latitudinal synchronization of this debris population is driven by the combination of inclination and clustering in right ascension of the ascending node (RAAN), the second of which results from operators leveraging naturally-occurring luni-solar perturbations to reduce costly north-south station-keeping effort.[50]

Upon close inspection of Figure 3.1 (and especially if animating Figure 3.1 using one frame per minute of propagation time), eight objects in the population qualitatively appear to be out-of-sync with the transverse latitude cycle exhibited by the rest of the population. That is, when the local debris populations at the longitudes of these "outliers" are rising in latitude from south to north through the equatorial plane, these objects are descending in latitude from north to south, against the flow of the synchronous patterns of life nominally

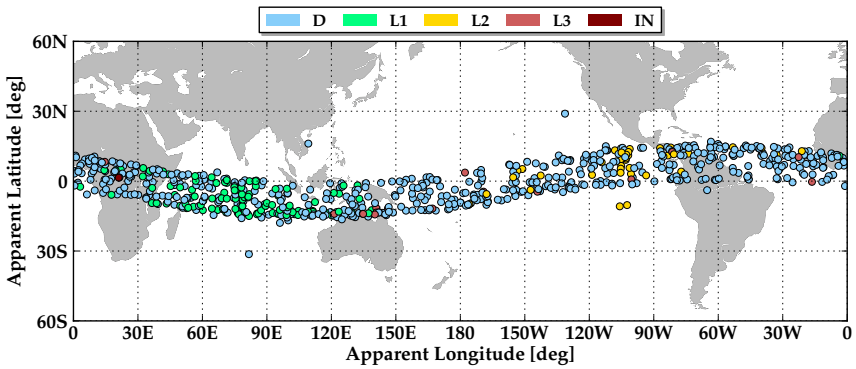


(a) Longitude/latitude distribution of debris population (00:00:00 Zulu).

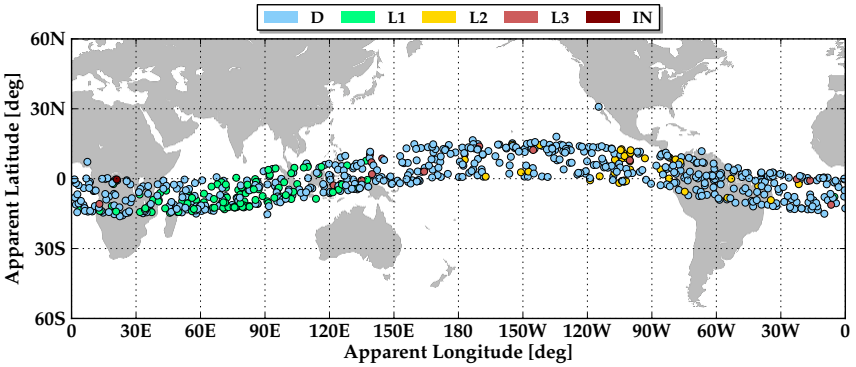


(b) Longitude/latitude distribution of debris population (06:00:00 Zulu).

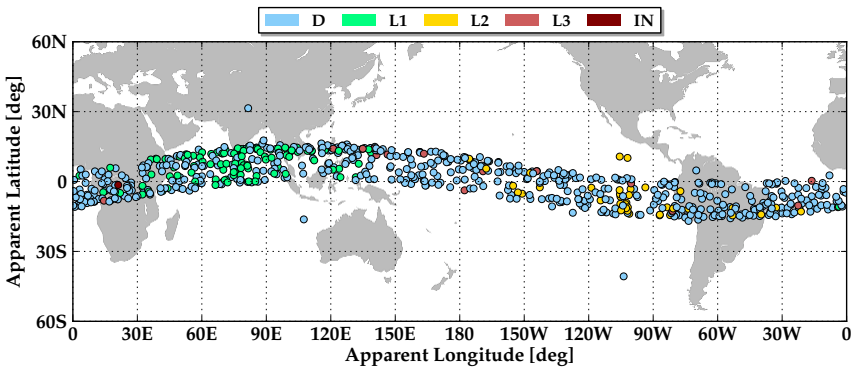


(c) Longitude/latitude distribution of debris population (12:00:00 Zulu).

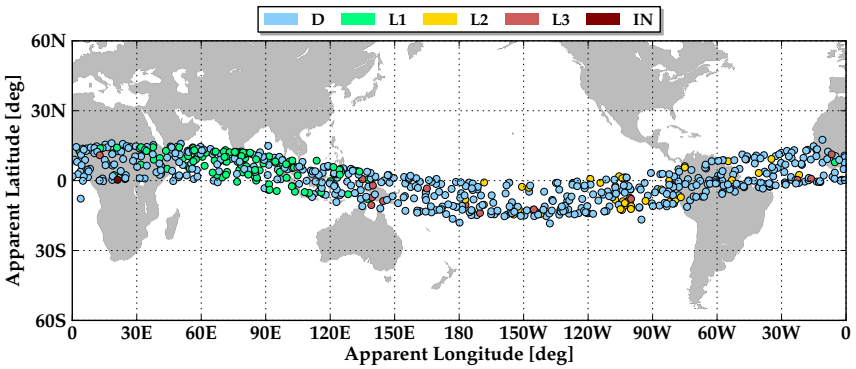


(d) Longitude/latitude distribution of debris population (18:00:00 Zulu).

Figure 3.1: Longitude/latitude distribution of GEO debris population on 01 March 2014, shown in six-hour intervals to illustrate the "wave-like" behavior of the debris population.

observed for derelict motion at GEO. This discrepancy in the latitude cycle indicates that the descending nodes of the outliers are currently located near the ascending nodes of the derelicts clustered in nearby longitude slots. This chapter is thereby borne out of the quest to characterize the apparent anomalous motion of these eight "outlying" objects, by studying whether such asynchronicity in latitude can arise under well-known RAAN dynamics at GEO driven by the coupling between luni-solar perturbations and Earth's oblateness.[3]

Specifically, this chapter provides a unifying summary of bottom-up analytical theory with top-down observational data to highlight the common linkage between these two dimensions of GEO debris behavior. The relevance of naturally-occurring patterns of life at GEO to current and future operations in the GEO arena is discussed, and long-term implications of these tendencies to space situational awareness in this arena are highlighted.

## 3.2 Inclination and RAAN Variations Induced by Luni-Solar Perturbations

The "doubly-averaged"[1] differential equations of motion governing inclination $i$ and right ascension of the ascending node (RAAN) $\Omega$ variations induced by luni-solar perturbations prominent at the GEO altitude are—for near-circular orbits only—given by[3,48]

$$\frac{\mathrm{d}i}{\mathrm{d}t} = \sum_{j=1}^{2} \frac{3}{8}\gamma_j \Big[ \cos(i)\sin(2i_j)\sin(\Omega-\Omega_j) + \sin(i)\sin^2(i_j)\sin(2(\Omega-\Omega_j)) \Big] \tag{3.1}$$

$$\begin{aligned} \frac{\mathrm{d}\Omega}{\mathrm{d}t} = -\frac{3}{2}J_2\left(\frac{R_\oplus}{a}\right)^2 n\cos(i) + \sum_{j=1}^{2}\frac{3}{16}\left(\frac{\gamma_j}{\sin(i)}\right)\Big[ \sin(2i)\left(1-3\cos^2(i_j)\right) \\ + 2\cos(2i)\sin(2i_j)\cos(\Omega-\Omega_j) + \sin(2i)\sin^2(i_j)\cos(2(\Omega-\Omega_j)) \Big] \end{aligned} \tag{3.2}$$

where the summations are performed over the Sun and the Moon, respectively, with $\gamma_j \equiv n_j^2 R_m/n$ for third-body mass ratios $R_m = 1$ for the Sun and $R_m = 1/82.3$ for the Moon.[48] In this formulation, $i$, $\Omega$, $n$, and $a$ denote the inclination, RAAN, mean motion, and semi-major axis of the uncontrolled derelict, respectively, while $i_j$, $\Omega_j$, and $n_j$ denote third-body

[1] Termed "doubly" averaged because the complete equations of motion for inclination and RAAN have been averaged once over the true anomaly $f$ (a fast variable), and a second time over the argument of perigee $\omega$ (a slow variable), such that daily, monthly, and yearly periodic variations in $i$ and $\Omega$ have been removed.[3]

inclination with respect to the equatorial plane, third-body RAAN with respect to the line of Aries, and third-body mean motion (i.e., approximately one revolution per year for the Sun and one revolution per sidereal month for the Moon). Note that the coupling between luni-solar perturbations and central body oblateness is incorporated in Equation (3.2) via the well-known term that describes secular drift in $\Omega$ induced by the $J_2$ zonal harmonic.[38]

Equations (3.1)-(3.2) offer insight into the long-term evolution of uncontrolled orbits in the GEO regime. In particular, Equation (3.1) indicates that inclination drift will be zero inasmuch as $\Omega - \Omega_j = 0^\circ$ or $\Omega - \Omega_j = 180^\circ$, i.e., the line of nodes for the uncontrolled object is aligned with that of the third body.[3] Without routine north-south station-keeping maneuvers, Equations (3.1)-(3.2) combine to drive a long-term, cyclical precession of the orbit plane, in which correlated motions of RAAN and inclination over an approximate 53-year period are analogous to the precession and nutation of a gyroscope.[50] Physically, out-of-plane force components acting on the uncontrolled object torque the orbit plane along the line of nodes, resulting in the angular momentum vector precessing about an intermediate axis displaced approximately 7.4° from Earth's rotation axis towards the ecliptic pole.[50,52]

The long-term, coupled inclination and RAAN variations described in Equations (3.1)-(3.2) are visualized with the well-known phase portrait in Figure 3.2(a), which provides the clockwise trajectories that uncontrolled objects will traverse in this inclination and RAAN phase space. Objects beginning with low inclination and a RAAN within Quadrants I or IV will experience a periodic, egg- or triangular-shaped (Type I) progression within this phase space, while objects initialized with a RAAN in Quadrants II and III experience a periodic, bell-shaped (Type II) progression.[50] For Type I motion, the node advances and regresses through the minimum and maximum inclinations of the cycle, respectively, each occurring at $\Omega = 0^\circ$. For Type II motion, the node continually regresses from minimum to maximum inclinations – nodal advancement is not experienced along these bell-shaped progressions.

The thick, red line in Figure 3.2(a) highlights the "separatrix-like," triangular-shaped boundary between Type I/II progressions,[53] informally termed the conga-line trajectory[2]

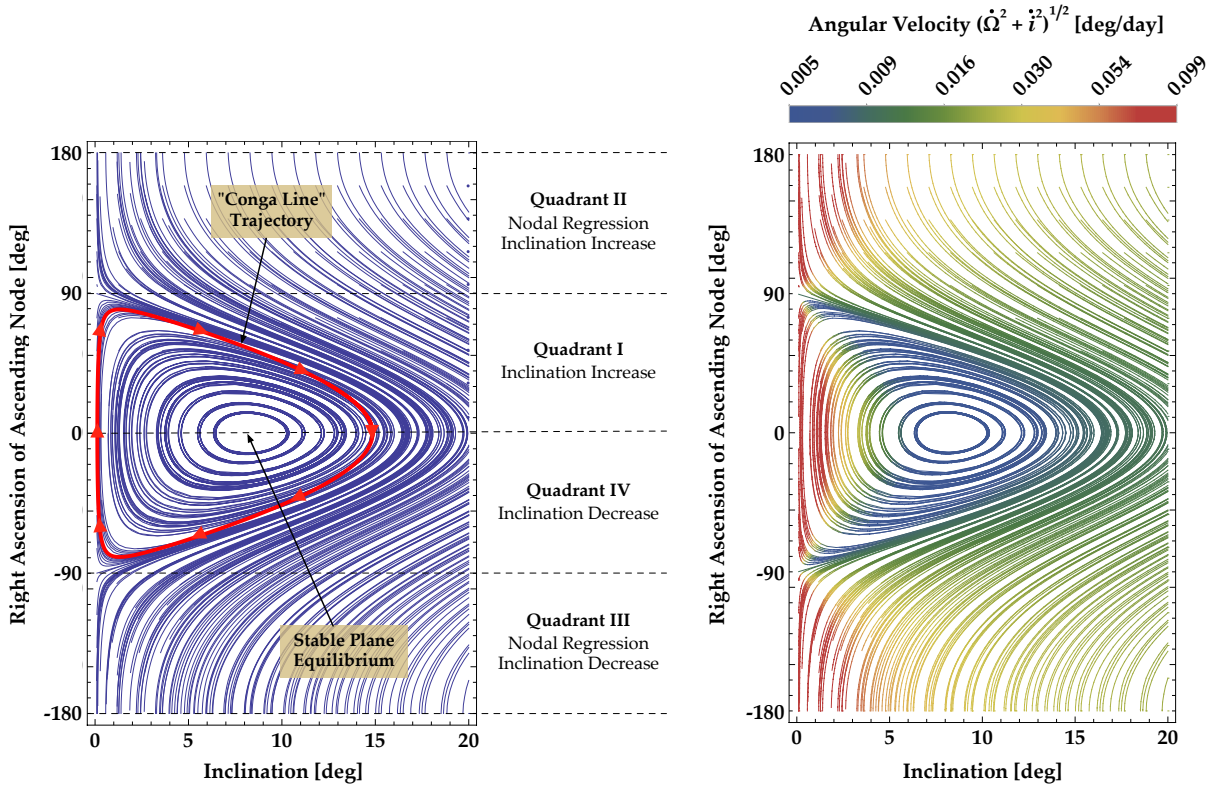


(a) Description of phase space trajectories at GEO.

(b) Angular rate on phase space trajectories.

Figure 3.2: Phase space portraits illustrating the doubly-averaged Equations (3.1)-(3.2) for inclination and RAAN variations induced by luni-solar perturbations at the GEO altitude.

because operational assets at GEO are often station-kept onto this curve to maintain near-zero inclination over their operational lifespans.[50] GEO operators minimize north-south station-keeping fuel allocation by initializing their assets with 1-2° inclination and a RAAN within Quadrant IV (e.g., $\Omega \approx -80°$), such that over the nominal lifespan of these satellites, luni-solar perturbations naturally decrease the inclination to nearly zero before the 53-year cycle begins increasing the inclination at a rate of approximately 0.8° per year.[9] If desired, routine station-keeping maneuvers can be used to re-initiate this portion of the triangular-shaped progression when the inclination begins to exceed the operational requirement.[50] Thus, maintaining the conga-line in Figure 3.2(a) is popular among GEO operators, as this phase progression best leverages natural perturbations to minimize expensive inclination

[2] See References 1 and 54.

control burns, which make up a sizeable portion of typical station-keeping fuel budgets.[3]

Figure 3.2(a) also illustrates the existence of the well-known GEO stable plane, which is a fixed point ($\dot{i} = \dot{\Omega} = 0$) of the doubly-averaged Equations (3.1)-(3.2). Objects initialized at this equilibrium configuration with $i_0 \approx 7.4°$ and $\Omega_0 \approx 0°$ exhibit dramatically-reduced inclination and RAAN variations during the 53-year cycle – inclination variations are confined to within 1.2° of the initial plane in this setup, in comparison to the 12-15° excursions typical for Type I and II progressions in Figure 3.2(a).[52] Physically, the stable plane equilibrium results from luni-solar perturbations acting against the nodal regression driven by central body $J_2$ oblateness, such that these equal-but-opposite effects cancel each other.[52] The stable plane has important operational implications for GEO satellite collocation, conjunction velocities, and mitigation alternatives, all of which are discussed in Reference 52.

Since both Type I and Type II progressions in Figure 3.2(a) have a period of approximately 53 years—even though inclination and RAAN variations are, in general, smaller for Type I cycles than for Type II cycles—Figure 3.2(b) shows the non-uniformity of the angular speed $\sqrt{\dot{\Omega}^2 + \dot{i}^2}$ along these progressions. As is predicted analytically with Equation (3.2), rapid nodal advancement occurs at small inclinations, when the luni-solar contributions to Equation (3.2) dominate $J_2$-induced nodal regression.[53] Type II motion exhibits a higher angular rate than "inner" Type I motion, such that each cycle maintains the 53-year period. Thus, although smart orbital insertion can leverage the naturally-occurring conga line trajectory to reduce the orbit from several degrees of inclination to equatorial, this is the most rapid part of the progression (lasting about three years), requiring re-initiation every time the inclination begins exceeding operational limits (e.g., five times in a 15-year lifespan).[50]

### 3.3 Current Inclination and RAAN Distribution

In light of the analytic theory presented in Section 3.2, it is instructive to consider the distribution of both controlled GEO satellites and the GEO derelict population within the inclination and RAAN phase portrait illustrated in Figure 3.2. Using the 28 February 2014

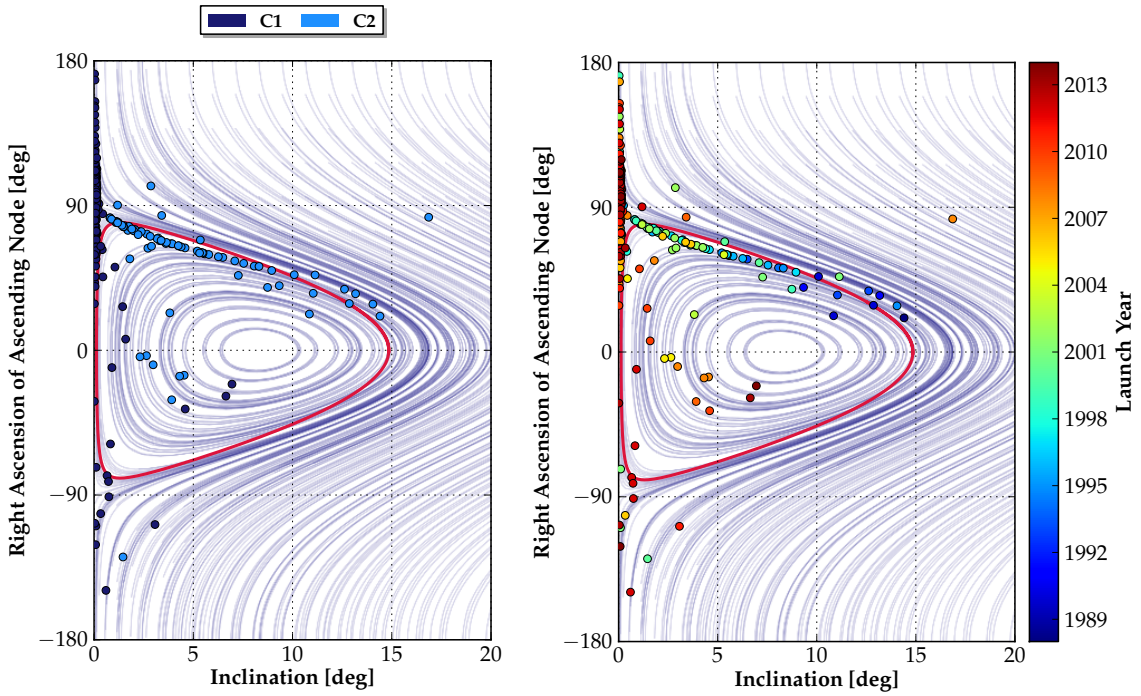


(a) Distribution of controlled satellites.

(b) Controlled distribution by launch year.

Figure 3.3: Phase space distribution of controlled GEO satellites on 28 February 2014.

TLE population described previously in Section 2.2, Figure 3.3 provides the phase portrait distribution for the 400 controlled GEO satellites in this TLE set, 318 of which are class C1 (longitude and inclination control), and 82 of which are class C2 (longitude control only). In particular, Figure 3.3(a) shows this controlled distribution colored by orbit class. As anticipated, the majority of class C1 satellites are maintaining near-zero inclination by either (a) executing routine station-keeping burns, or (b) leveraging the conga-line trajectory or a variation thereof for a naturally-occurring inclination decrease, as described in Section 3.2. Conversely, the majority of C2 satellites—those that were not equipped to perform out-of-plane station-keeping, or those that have lost this capability on-orbit—are progressing on or near the intermediate conga-line curve.[3] Figure 3.3(b), which illustrates this controlled distribution colored by launch year, confirms that the class C2 satellites furthest along the

[3] Recall that the conga-line trajectory and the doubly-averaged Equations (3.1)-(3.2) provide approximate, analytic, first-order descriptions of actual inclination and RAAN variations experienced at the GEO altitude.

clockwise, 53-year cycle (i.e., have largest inclinations in Quadrant I) are the oldest objects in the operational population. Thus, given two collocated C2 objects in this synchronized configuration, the younger object will lag behind the older object in the daily latitude cycle, since the node of the younger satellite has not regressed as far as that of the older satellite.[4] Ultimately, the dichotomy between fully-controlled C1 satellites and partially-controlled C2 satellites in Figure 3.3 demonstrates that while out-of-plane station-keeping is used to maintain near-equatorial orbits for C1 satellites, coupled inclination and RAAN variations exhibited by C2 objects follow predictable progressions described by Equations (3.1)-(3.2).

Figure 3.4 provides the phase portrait distribution for the 745 uncontrolled GEO objects extracted from the 28 February 2014 TLE set (recall Figure 2.1). Prominent clustering in debris objects is observed on or near the conga-line trajectory, especially around the apex of this triangular-shaped progression, where the inclination achieves a maximum value of approximately 15° over the 53-year cycle. Reference 51 shows that in 2002 (i.e., 39 elapsed years since the first GEO utilization in 1963), the majority of uncontrolled objects at GEO had not yet crossed the apex of this systematic progression. Now, 12 years later, Figure 3.4 shows that a significant portion of this uncontrolled population has already crossed—or is currently crossing—into the second half of the conga line cycle (from Quadrant I to Quadrant IV), in which the RAAN continues to regress while the inclination begins decreasing. Since 51 years have now elapsed since the first GEO utilization, the first GEO debris objects generated in the 1960s—including the world's first GEO communications satellite, Syncom 2—are soon to complete a full Type I revolution in this inclination and RAAN phase space.

Figure 3.4(a), which shows the uncontrolled debris distribution colored by orbit class, demonstrates that factors such as longitude of abandonment or orbit class—whether drifting or librating about one or both of the gravitational wells—do not affect the phase space progression that is followed by a debris object.[5] It is important to emphasize that inclina-

[4] Latitudinal lag between collocated satellites of differing on-orbit age has been confirmed in animations and numerical simulations performed by Darren McKnight and Frank Di Pentino of Integrity Applications.

[5] Although orbit class does not affect the progression directly, the semi-major axis, which is critical in de-

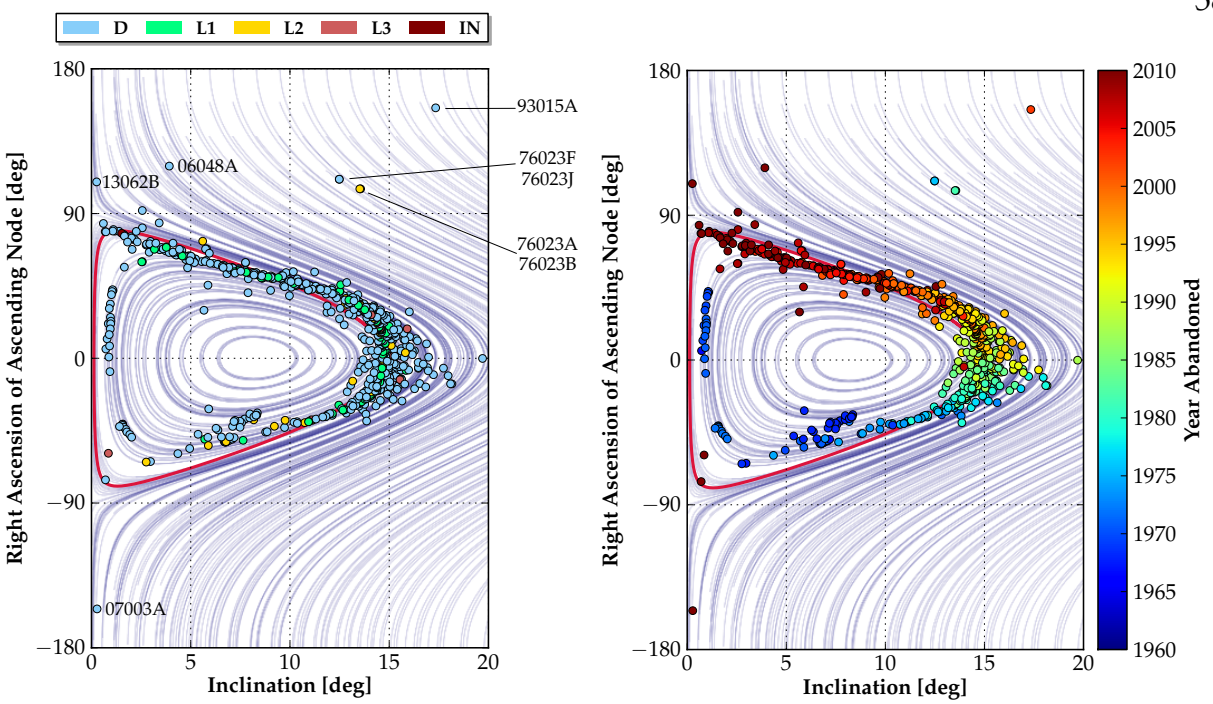


(a) Distribution of uncontrolled objects.

(b) Uncontrolled distribution by abandon year.

Figure 3.4: Phase space distribution of uncontrolled GEO derelicts on 01 March 2014.

tion and RAAN at the moment the object is abandoned dictate whether a Type I or Type II progression will result in the following cycle. Since luni-solar gravitational perturbations are conservative, the resulting cycles governed by Equations (3.1)-(3.2) are periodic, and do not admit natural transition from Type I to Type II behavior, or vice-versa, under luni-solar perturbations alone. The apparent "outlying" objects labeled in Figure 3.4(a), discussed in Section 3.5, could result from one or more of the following possibilities or artificial means:

(1) When operational, these satellites were not station-kept to the conga line trajectory for mission-related reasons, or (for launch debris) were not inserted onto this cycle;

(2) End-of-life disposal was attempted, and the maneuver sequence—purposefully or inadvertently—altered the inclination/RAAN while raising the semi-major axis;

termining whether an object will drift or librate once uncontrolled, is a required parameter of Equation (3.2), and is assumed to be constant when propagating this differential equation. This is a valid assumption given the magnitude of naturally-occurring semi-major axis variations at GEO, which are insignificant relative to the radius of the GEO ring (e.g., a 60° libration amplitude results from ±30 km of semi-major axis variation).

(3) Since Gauss's variational equations show that any out-of-plane acceleration will simultaneously change both the inclination and RAAN,[55] an out-of-plane collision with either environmental or artificial debris occurred, or the object has vented (or is currently venting) propellant externally, with a component out of the orbit plane.

Although these possibilities are not exhaustive, they enforce the fact that initial conditions in inclination and RAAN space dictate whether a Type I or Type II progression will result. Under the doubly-averaged Equations (3.1)-(3.2), these two modes are mutually exclusive.

To illustrate how object age on-orbit can be approximated by the phase portrait of Figure 3.2, Figure 3.4(b) shows the uncontrolled debris distribution colored by estimated year of abandonment. For upper stages and other launch or mission-related debris (e.g., apogee kick motors), the year of abandonment is the launch year; for derelict payloads in the population, the year of abandonment is approximated via a linear lifespan model derived from historical lifespan data, which reflects a linear increase from six years on average in 1977 to 13 years on average in 2010.[1] Similar to Figure 3.3(b), Figure 3.4(b) illustrates that derelicts further along the triangular-shaped progression are, in general, older than those near the "beginning" of the progression close to $i \approx 0^\circ$ and $\Omega \approx 90^\circ$. Objects abandoned in the late 1980s have achieved their maximum inclination of the cycle at the apex of the progression, while objects abandoned in the 1960s (approximately 26-27 years earlier) are now moving through the minimum inclination of the cycle towards a full revolution in the phase space. Thus, assuming that a particular payload of interest—operational or defunct—was station-kept onto the popular conga-line trajectory, the phase portrait of Figure 3.4(b) can be leveraged in tandem with the angular rate information of Figure 3.2(b) to estimate either when this object was abandoned, or when this object lost north-south station-keeping capability.

## 3.4 Evolution of Inclination and RAAN Distribution

In addition to studying the current distribution of derelict GEO objects in inclination and RAAN space, it is useful to predict the evolution of this distribution under the doubly-averaged Equations (3.1)-(3.2). Figure 3.5 shows this phase space distribution on 01 March 2014, as compared to the approximate distributions predicted 20, 40, and 60 years after this date. As noted in Section 3.3, a significant proportion of the present-day debris population is crossing into the second half of the conga line progression, producing strong clustering in RAAN about the line of Aries ($\Omega = 0°$). Deterministic, predictable clustering in RAAN has been widely leveraged for space-based space surveillance (SBSS), sensor tasking, and space situational awareness activities at GEO.[51] By pointing ground- or space-based sensors towards the well-known GEO "pinch points," observational coverage of the resident space object population at GEO can be maximized, and the probability of detecting "new" objects, for purposes of catalog maintenance, is improved. Reference 50 confirms that the productivity of the Space-Based Visible (SBV) sensor on the Midcourse Space Experiment (MSX) satellite improved 20-30% by taking advantage of this natural clustering in RAAN.

However, as Figure 3.5 illustrates, the interplay between location in the phase space and the location-specific angular rates in Figure 3.2(b) gives rise to the periodic dispersion and eventual re-focusing in the RAAN distribution. As the Type I derelicts circulate in this phase space, the spread of this distribution expands from reflecting Quadrant I clustering on [0°,90°] to reflecting full, Quadrant I/IV clustering on [-90°,90°]. For purposes of SBSS and space situational awareness activities, this dispersion of objects within the phase space indicates that the GEO pinch points are spreading out, thus diminishing in usefulness for sensor tasking. Therefore, in order to establish a leak-proof search fence, a more substantial search region in right ascension must be implemented to maintain current productivity levels achieved by SBV and other ground- or space-based sensors. Beneficially, Figure 3.5 shows that dispersion in RAAN does not continue indefinitely; rather, the distribution be-

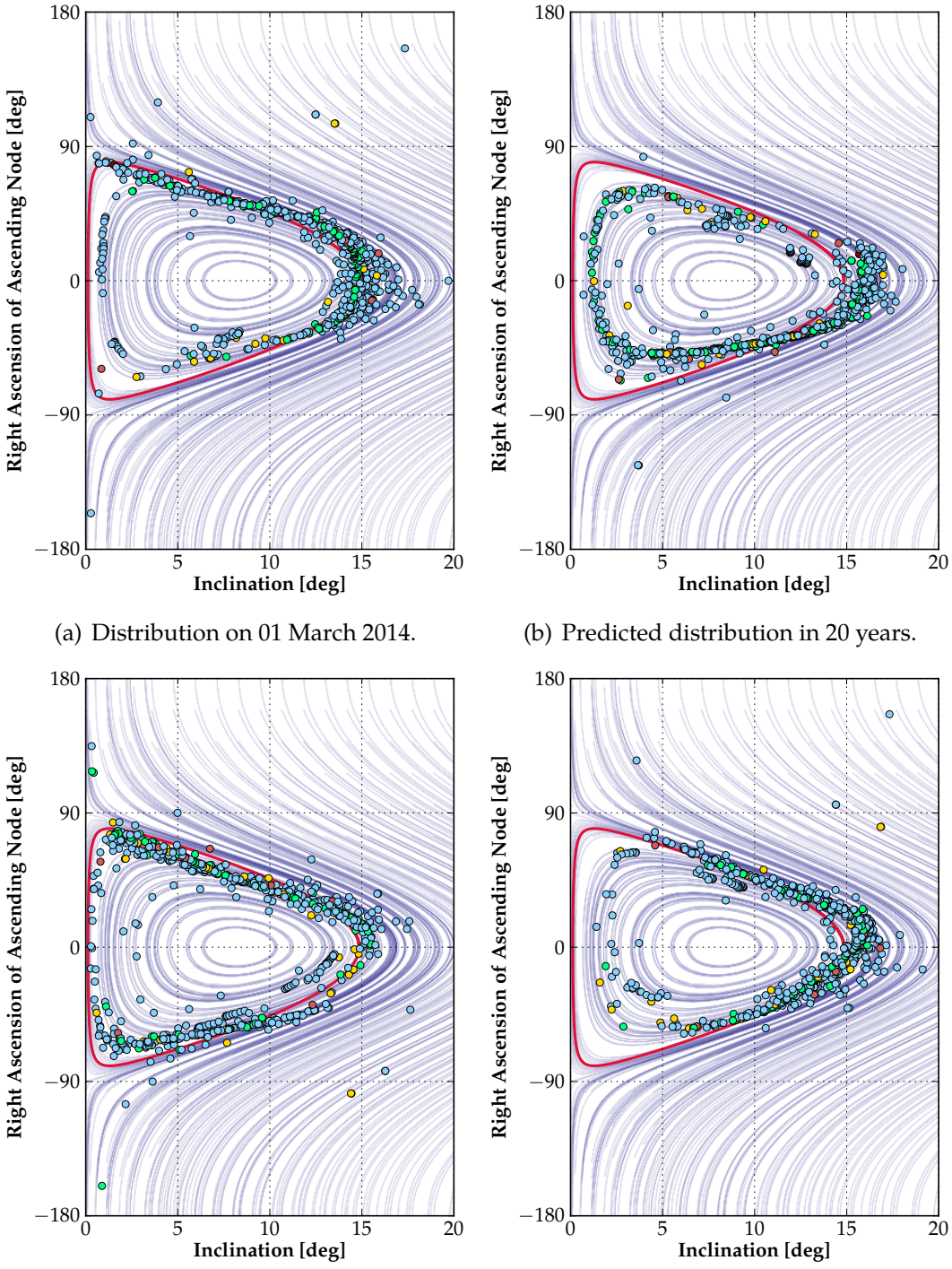


(a) Distribution on 01 March 2014.

(b) Predicted distribution in 20 years.

(c) Predicted distribution in 40 years.

(d) Predicted distribution in 60 years.

Figure 3.5: Evolution of derelict motion at GEO in inclination/RAAN space over 60 years, predicted using Equations (3.1)-(3.2) for Sun/Moon-driven inclination/RAAN variations.

gins to re-focus as the majority of the population passes through the minimum-inclination portion of the 53-year cycle to complete one Type I revolution, after which nodal regression rates slow. The spread in this RAAN distribution thus "ebbs and flows" as luni-solar perturbations and Earth oblateness propel the derelict population around the conga line cycle.

## 3.5 Investigating the Unsynchronized Objects

In light of the bottom-up, analytic theory presented in Section 3.2, and the top-down, observational portrait of the current inclination and RAAN distribution in Section 3.3, the eight derelict objects identified as being asynchronous to the transverse wave-like behavior shown in Figure 3.1 are now examined. Animations of the daily latitude cycle of the GEO derelict population indicate that these "outliers" traverse latitude cycles either partially or fully out-of-phase with those exhibited by nearby derelicts in neighboring longitude slots. As noted earlier, two latitude cycles become more out-of-phase the farther the corresponding RAAN angles are displaced from one another, e.g., two objects with RAAN angles that are 180° apart will be completely unsynchronized in the latitude cycle. Two asynchronous latitude cycles are best visualized in right ascension and declination coordinates, in which these once-daily cycles appear as out-of-phase sine waves instead of "figure-8" orbits.[50,51]

For purposes of flight safety and on-orbit anomaly correlation, it is critical to understand why the RAAN angles for these eight outliers—listed in Table 3.1—are not clustered with those of the rest of the large-scale, unclassified GEO debris population extracted from the 28 February 2014 TLE set. Reference 1 highlights that the equatorial crossing windows for the synchronized debris population are predictable and dependent upon time of day in addition to time of year. These alternating, six-hour intervals of increasing and decreasing flux relative to any given longitude slot are important for risk assessment and prediction at GEO, since conjunction events are most likely to occur in the out-of-plane direction when the longitude slot is passing through either the ascending or descending node pinch point. Derelicts that are asynchronous to this pattern of life present a special hazard in that these

Table 3.1: GEO debris objects exhibiting unsynchronized latitude cycles on 01 March 2014.

| Common Name | COSPAR | Class | Common Name | COSPAR | Class |
|---|---|---|---|---|---|
| LES-8 | 76023A | L2 | USA 98 (UFO F1) | 93015A | D |
| LES-9 | 76023B | L2 | Sinosat-2 (Xinnuo-2) | 06048A | D |
| Titan 3C Transtage R/B | 76023F | D | Beidou-1D (Beidou-4) | 07003A | D |
| LES Operational Debris | 76023J | D | Proton-M Briz-M R/B | 13062B | D |

objects cross the equatorial plane when north-south flux levels are at a daily minimum.[6]

As the current inclination and RAAN distribution in Figure 3.4 shows, the eight unsynchronized derelicts in Table 3.1 are currently positioned in Quadrants II and III, away from the significant RAAN clustering occurring at the boundary between Quadrants I and IV. These objects are not exhibiting oscillatory Type I trajectories in the phase space; rather, they are following bell-shaped Type II progressions, according to Equations (3.1)-(3.2). In contrast to the Type I cycles, which exhibit long durations of nodal regression followed by shorter periods of nodal advancement near the minimum inclination of the cycle, Type II cycles exhibit continual nodal regression over the entirety of the 53-year cycle. This critical difference is illustrated in Figure 3.6, which provides the predicted RAAN trajectories over a 60-year interval for various synchronized and unsynchronized objects in the 28 February 2014 TLE set. Figure 3.6(a) provides the RAAN trajectories for eight initially synchronized objects, i.e., with RAAN angles within one standard deviation of the distribution mean.[7] The RAAN angles for these Type I derelicts never exceed two standard deviations from the mean at any point during the 60-year prediction period. Thus, from the perspective of longitude/latitude coordinates, these objects are "strongly" synchronized with the transverse wave-like behavior in Figure 3.1, and maintain this synchronization over the 53-year cycle.

Conversely, Figure 3.6(b) provides predicted RAAN trajectories for the eight unsynchronized objects in Table 3.1, which have initial RAAN angles greater than two standard

[6] As an analogy, consider the hazard to one's vehicle when driving on the highway. Although risk levels during rush hour can be reasonably characterized in that they spike during predictable time frames, the risk attributed to a rogue driver speeding southbound down the northbound side is challenging to characterize.

[7] The expanding and contracting $1/2/3\sigma$ swaths in Figure 3.6 reflect the future distributions in Figure 3.5.

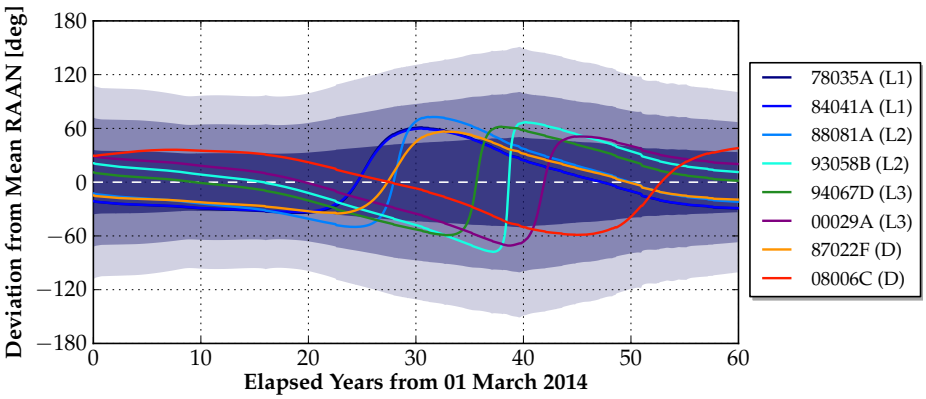


(a) Projected 60-year RAAN profiles for initially synchronized objects.

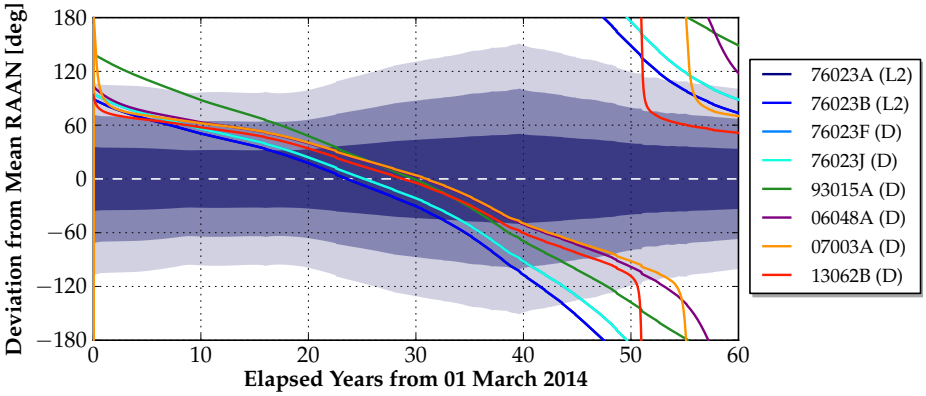


(b) Projected 60-year RAAN profiles for initially unsynchronized objects.

Figure 3.6: RAAN histories for initially synchronized and initially unsynchronized objects near GEO on 28 February 2014, predicted using the doubly-averaged Equations (3.1)-(3.2). Shaded swaths indicate $\pm 1$, $\pm 2$, and $\pm 3$ standard deviations from the distribution mean.

deviations away from the distribution mean. Continuous nodal regression of these Type II trajectories drives the RAAN angles of these outliers—and thus their daily latitude cycles—from being unsynchronized on 01 March 2014 into strong synchronization in an estimated 25-35 years. After approaching and achieving the distribution mean, however, the RAAN angles for these Type II derelicts continue to regress, until these objects once again become unsynchronized in 45-55 years, during which the node rapidly regresses as the minimum inclination of the cycle is achieved. The patterns of life for Type II objects thus differ from

those of Type I objects in that although Type I trajectories admit synchronized latitude cycles over the entirety of the 53-year progression, Type II trajectories result in latitude cycles that shift from unsynchronized to synchronized—and back—during a single progression. The apparent anomalous behavior observed in Figure 3.1 can therefore be explained by the Type II progressions that these eight derelicts are traversing in inclination/RAAN space. Again, since natural transitions from a Type I to Type II cycle (or vice versa) will not occur under conservative gravitational perturbations alone, the three possibilities highlighted in Section 3.3 apply if assessing how or why these objects are following Type II progressions.

## 3.6 Conclusions from Research Goal

In this chapter, the wave-like synchronization exhibited by the derelict population at GEO is explained using bottom-up, analytical theory that describes inclination and RAAN variations driven by luni-solar perturbations and Earth's oblateness over a 53-year period. This well-known theory is combined with top-down, operational observation data to paint a portrait of the current inclination and RAAN distribution by controlled or uncontrolled class and age on-orbit, and how this distribution will evolve under the approximate doubly-averaged Equations (3.1)-(3.2). Lastly, derelicts with partially or fully out-of-phase latitude cycles are explained not by apparent anomalous motion, but rather in terms of the difference between egg-shaped, Type I and bell-shaped, Type II progressions in the phase space.

Several operational implications arising from the synchronized debris motion at GEO are highlighted in this chapter for purposes of flight safety, anomaly correlation, and space situational awareness activities in this regime. Naturally-occurring Type II motion—which arises from the combination of inclination, RAAN, and semi-major axis when the satellite is abandoned—explains not only why younger objects lag behind older objects in the daily latitude cycle, but also shows how the latitude cycle of a Type II object transitions into and out of synchronization with the Type I population over the course of the 53-year cycle. For sensor tasking, predictions of the combined Type I/II motion over a projected 60-year time

frame highlight that the GEO pinch points resulting from tight clustering in RAAN are beginning to spread out, achieving maximum $3\sigma$ dispersion in approximately 40 years. Thus, both ground and space-based surveillance systems will need an increasingly wider search fence in right ascension to maintain current levels of sensor productivity in the near future.

## 3.7 Continuing Research Questions

For continuing research in this area, the following research questions are of interest:

(1) The doubly-averaged Equations (3.1)-(3.2), which are valid for near-circular orbits only, describe long-period inclination and RAAN variations driven by a combination of luni-solar gravitation and central body oblateness. What does the evolution of the phase space distribution in Figure 3.5 look like under higher-fidelity forcing, particularly if the non-conservative effect of solar radiation pressure is included?

(2) Figure 3.5 highlights the existence of multiple trajectories similar to the conga line that are popular amongst GEO operators. How many individual "conga-line-like" Type I cycles exist? Do they arise out of a need to maintain a minimum inclination for latitudinal coverage requirements, or do they arise from orbit insertion errors?

(3) Can the periodic expansion and contraction of the RAAN distribution of the GEO debris population—as illustrated in Figures 3.5-3.6—be leveraged by autonomous ground and space-based sensors, in order to maintain desired productivity levels?

# Chapter 4

## *Research Goal 2(a)*: Forecasting longitude-dependent congestion at GEO arising from nominal launch traffic

### 4.1 Overview of Research Goal

In addition to assessing the longitude-dependent congestion arising from the present-day, large-scale debris population at GEO, it is also imperative to investigate the influence of critical population growth mechanisms, in particular, nominal launch traffic to the GEO regime. From the perspective of orbital debris congestion at GEO, the "no future launches" scenario typically considered in various long-term debris growth analyses is most optimal, yet highly unrealistic for the profitable real estate at GEO. Currently, the GEO catalog is increasing by approximately 30 new operational satellites per year,[6,11] and as will be shown, historical launch data indicates that this launch traffic rate will only continue increasing in the years to come. Although widespread use of integrated apogee kick motors has caused the growth of upper stages in GEO orbit to begin leveling-off, this reduction in GEO object growth has been compensated for by a rapidly-intesifying number of payload insertions.[6]

Population augmentation in the GEO environment has been researched briefly in the literature,[6,11] albeit, these studies provide debris fluxes averaged over longitude, altitude, and time, and thus fail to address which longitude slots are the most prone to proliferating debris populations resulting from a combination of routine launch traffic, operational lifespan, and compliance to mitigation guidelines. To the author's knowledge, a representative launch traffic model for the GEO regime—one that characterizes not only the frequency of

launches to GEO, but the operational orbits that these satellites are inserted into—has not been presented in the literature. This thesis addresses this critical void in the literature by presenting a non-homogeneous method for modeling growth of the GEO catalogue, thus facilitating prediction of high-risk longitude slots for operational GEO assets over the next 50 years, and serving to further enforce that averaging debris flux is becoming increasingly misrepresentative for GEO. The objective of this research goal is to illustrate worst-case debris congestion at GEO under representative launch traffic and a nominal operational lifespan, and demonstrate that compliance to mitigation guidelines at end-of-life can serve to attenuate localized congestion – especially in the neighborhoods of the gravitational wells.

It is important to emphasize that nominal launch traffic is the only input to the debris growth model used in this chapter. On-orbit fragmentation events (investigated separately in Chapter 5), ejection of solid rocket motor slag, shedding of multi-layered insulation, and other growth mechanics incorporated in Reference 6, for example, are not considered here.

## 4.2 Operational GEO Orbit Model

During long-term congestion forecasting, the RSO population at GEO must be meaningfully augmented to simulate typical launch traffic in this regime. Realistic population augmentation requires an operational GEO orbit model to quantify where new GEO assets are typically positioned at insertion into their designated longitude slots – such a model serves to generate the initial conditions for new operational satellites created during long-term forecasting (the GEO launch instantiation procedure is highlighted in Section 4.4). To construct a first-order operational orbit model, data from the 01 January 2013 TLE set, the *Space-Track Geosynchronous Report*,[1] and the *SatBeams* database[2] are compiled, giving semi-major axis, eccentricity, inclination, and geocentric longitude information for 768 past and present GEO satellites—including all unclassified launches to GEO as of 01 January 2013—

[1] *Space-Track Geosynchronous Report* available at: `https://www.space-track.org/perl/geo_report.pl`.
[2] The *SatBeams* database provides GEO satellite longitude and launch year information, and is available at: `http://www.satbeams.com/satellites`.

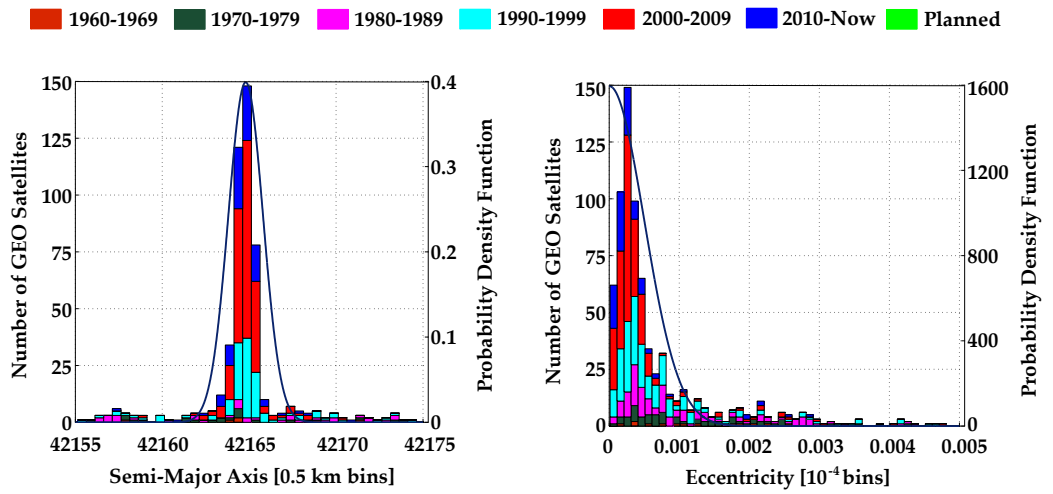


(a) Semi-major axis PDF for GEO orbit.

(b) Eccentricity PDF for GEO orbit.

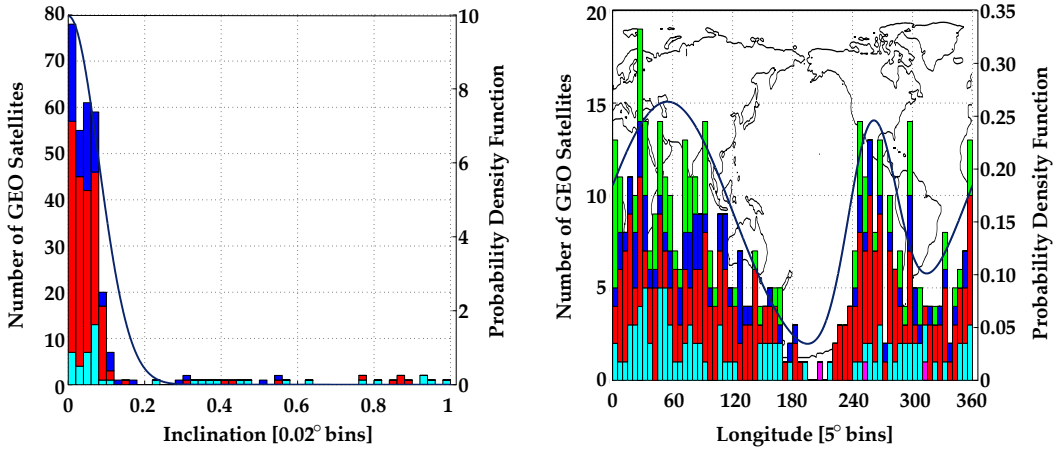


(c) Inclination PDF for GEO orbit.

(d) Longitude PDF for GEO orbit.

Figure 4.1: Parameter distributions for representative sampling of operational GEO orbits.

and 94 satellites planned through the year 2020. Employing these data, stacked histograms are constructed for the semi-major axis, eccentricity, inclination, and geocentric longitude, and appropriate probability density functions are fit to these histograms to construct representative distributions from which the orbital elements of a new controlled satellite may be sampled.[3] Figure 4.1 provides these parameter histograms (stacked by launch decade) and their associated probability density functions, summarized for each element below:

[3] The assumption underlying this methodology is that the semi-major axis, eccentricity, inclination, and longitude of the controlled satellite are considered independent, uncorrelated parameters during sampling.

- *Semi-major axis* ($a$). Normal distribution with mean $\mu = 42164.8$ km and standard deviation of $\sigma = 1.0$ km. The probability density function (PDF) and cumulative distribution function (CDF) for this distribution are given by (for $-\infty < x < \infty$):

$$f_{\mathcal{N}}(x;\mu,\sigma) = \frac{1}{\sigma\sqrt{2\pi}} \exp\left[-\frac{1}{2}\left(\frac{x-\mu}{\sigma}\right)^2\right] \tag{4.1}$$

$$F_{\mathcal{N}}(x;\mu,\sigma) = \frac{1}{2}\left[1 + \operatorname{erf}\left(\frac{x-\mu}{\sigma\sqrt{2}}\right)\right] \tag{4.2}$$

- *Eccentricity* ($e$). Half-normal distribution derived from a normal distribution with zero mean and $\sigma = 5.0 \times 10^{-4}$, for which the PDF and CDF are given by (for $x \geq 0$):

$$f_{\mathcal{N}/2}(x;\sigma) = \frac{\sqrt{2}}{\sigma\sqrt{\pi}} \exp\left(-\frac{x^2}{2\sigma^2}\right) \tag{4.3}$$

$$F_{\mathcal{N}/2}(x;\sigma) = \operatorname{erf}\left(\frac{x}{\sigma\sqrt{2}}\right) \tag{4.4}$$

- *Inclination* ($i$). Half-normal distribution derived from a normal distribution with zero mean and $\sigma = 0.08°$.

- *Longitude* ($\lambda$). Gaussian mixture of two wrapped normal distributions with $(\mu_1, \sigma_1) = (55°, 65°)$ and $(\mu_2, \sigma_2) = (260°, 25°)$, mixed as follows:[4]

$$\lambda \sim 0.75 f_{\mathcal{W}}(\mu_1, \sigma_1) + 0.25 f_{\mathcal{W}}(\mu_2, \sigma_2) \tag{4.5}$$

  The PDF and CDF for the wrapped normal distribution are given by ($0 \leq x \leq 2\pi$):

$$f_{\mathcal{W}}(x;\mu,\sigma) = \frac{1}{\sigma\sqrt{2\pi}} \sum_{k=-\infty}^{\infty} \exp\left[-\frac{(x-\mu+2\pi k)^2}{2\sigma^2}\right] \tag{4.6}$$

$$F_{\mathcal{W}}(x;\mu,\sigma) = \frac{1}{2}\sum_{k=-\infty}^{\infty}\left[\operatorname{erf}\left(\frac{x-\mu+2\pi k}{\sigma\sqrt{2}}\right) - \operatorname{erf}\left(\frac{-\mu+2\pi k}{\sigma\sqrt{2}}\right)\right] \tag{4.7}$$

For computer implementations, sampling from the distributions is performed by drawing a pseudo-random number on the interval $[0, 1]$ that represents the cumulative probability

[4] A Gaussian mixture is selected to simulate the bimodality of the longitude histogram in Figure 4.1(d), i.e., high concentrations of operational satellites above Europe/Asia and North America, but minimal assets above the Atlantic and Pacific Oceans.

sampled in the desired distribution. The appropriate CDF is then back-solved for the value of $x$ that would yield this cumulative probability. Back-solving the wrapped normal CDF is performed by incrementally stepping through the interval $[0, 2\pi]$ in Equation (4.7) until the sampled cumulative probability is achieved to tolerance (it is sufficient to iterate $k$ from $k = -100 \ldots 100$).

Right ascension of the ascending node $\Omega$ is selected uniformly on the interval $[0, 360^\circ]$, and the true anomaly is initialized as $0^\circ$, i.e., new satellites are inserted at periapsis. As a result, the argument of perigee $\omega$ is a dependent parameter that must satisfy the relation

$$\omega = \alpha_G + \lambda - \Omega \tag{4.8}$$

where $\alpha_G$ denotes the right ascension of Greenwich, computed at the epoch of insertion. After the initial orbit elements have been sampled in this manner, these Keplerian elements are converted into a Cartesian state and assigned to the created satellite. This methodology ensures that new controlled satellites created during long-term forecasting are initialized with orbit elements that are highly representative of the operational GEO orbits harnessed since the first GEO utilization in 1963.

### 4.3 Launch Instantiation Procedure

Launches to operational GEO orbits are simulated with the probabilistic, open-loop event instantiation method implemented in the European Space Agency's DELTA (Debris Environment Long-Term Analysis) tool.[11] Following Reference 11, the probability $\mathcal{P}_j$ of $j$ launches occurring over a given analysis interval is modeled with the Poisson distribution:

$$\mathcal{P}_j = \frac{c^j}{j!} \exp(-c) \tag{4.9}$$

where $c$ is the average number of launches occurring over the analysis interval, computed as $c =$ (average annual launch rate to orbit regime [years$^{-1}$]) $\times$ (length of analysis interval [years]).[11] Assuming the "business-as-usual" GEO launch rate of 30 satellites per year[6,11]

and using one-day analysis intervals, $c \approx 0.082$ as a first approximation for typical launch traffic at GEO. For computer implementations, the probabilities $\mathcal{P}_j$ for $j = 0, 1, \ldots, k$ are first determined until a threshold $\epsilon$ is achieved, such that $\mathcal{P}_{k+1} \leq \epsilon$ (for this study, $\epsilon \equiv 10^{-6}$). The resultant probabilities are then normalized such that their sum is unity:

$$\hat{\mathcal{P}}_j = \frac{\mathcal{P}_j}{\sum_{i=0}^{k} \mathcal{P}_i} \implies \sum_{j=0}^{k} \hat{\mathcal{P}}_j = 1 \tag{4.10}$$

A pseudo-random number $\hat{\zeta}$ on $[0, 1]$ is drawn, and the number of launch occurrences in the analysis interval is thus determined by the largest $j$ for which the sum of the normalized probabilities $\hat{\mathcal{P}}_j$ is still less than $\hat{\zeta}$, i.e.,

$$\sum_{i=0}^{j} \hat{\mathcal{P}}_i \leq \hat{\zeta} < \sum_{i=0}^{j+1} \hat{\mathcal{P}}_i \tag{4.11}$$

Therefore, following each day of propagation, a pseudo-random number $\hat{\zeta}$ is drawn, and the number of launches during the past day is determined with Equation (4.11). If a successful launch has been initiated, a controlled GEO satellite (C1) is created, and the initial orbit elements are sampled from the representative distributions presented in Section 4.2. For the purposes of this congestion study, the satellite is injected into its orbit at midnight, and is assigned a nominal lifetime of 15 years.[5] Controlled satellites that reach end-of-life (EOL) during propagation are abandoned without any attempt at mitigation compliance – these abandoned satellites are added to the uncontrolled RSO population for propagation.

Although the business-as-usual launch rate of 30 new GEO satellites per year offers a suitable first approximation for long-term congestion forecasting in this arena, it is more instructive to consider the more realistic case of an increasing launch rate to operational orbits at GEO. Figure 4.2 illustrates the number of launches to GEO occurring each year since 1963, using data extracted from the *Space-Track Geosynchronous Report*. Observing that the

[5] The baseline controlled population in the 01 January 2013 TLE set is also assigned this nominal lifetime (COSPAR designation gives launch year). References 1 and 6 illustrate that the average design lifetime for GEO satellites has continued to increase since 1964, but extended lifetimes are not simulated in this analysis.

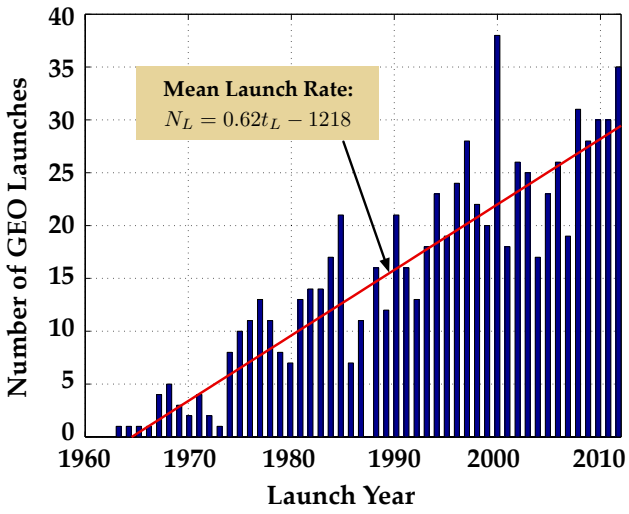


Figure 4.2: Annual launches to GEO since 1963.

number of launches $N_L$ is approximately proportional to the launch year $t_L$, linear regression provides the following linearly-increasing GEO launch rate model:

$$N_L = 0.62t_L - 1218 \text{ [launches/year]} \tag{4.12}$$

To implement this launch rate model, the parameter $c$ is updated after every year of propagation, and the probabilities in Equations (4.9)-(4.11) are recomputed to reflect a linearly-increasing launch rate during probabilistic launch instantiation.

## 4.4 "Business as Usual" Launch Traffic without Mitigation

Figure 4.3 illustrates the forecasted localized congestion for a 50-year prediction span beginning on 01 January 2013, assuming this linearly-increasing model in strict absence of mitigation measures. Figure 4.3(a) illustrates the absolute number of near-miss events per day for the 50 km GEO torus, while Figure 4.3(b) quantifies increase in the mean number of near-miss events per day—averaged over each year of propagation—over the idealized "no future launches" scenario, in which all launch traffic to GEO ceases. Similar results are illustrated in Figure 4.3 for the 100 km and 300 km minor radius cases. As anticipated, the

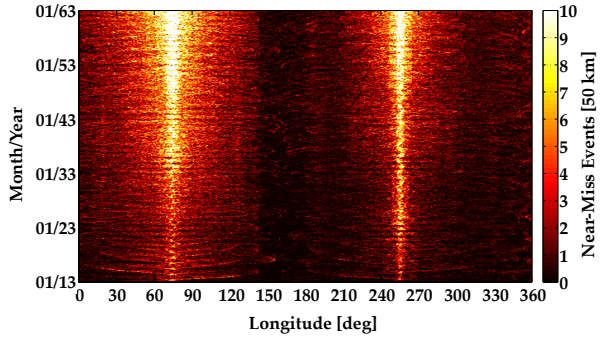


(a) Near-miss events per day (50 km torus).

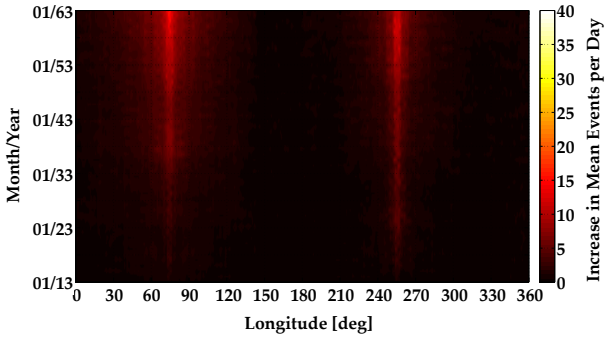


(b) Increase in near-miss events at 50 km.

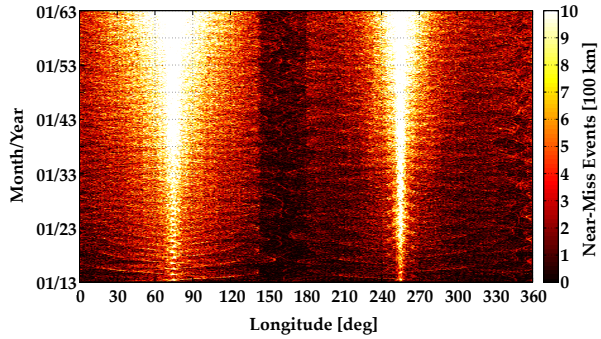


(c) Near-miss events per day (100 km torus).

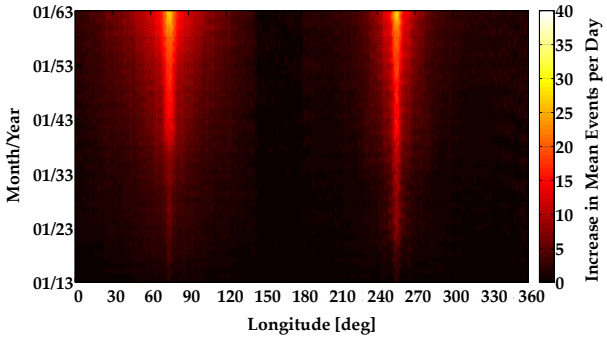


(d) Increase in near-miss events at 100 km.

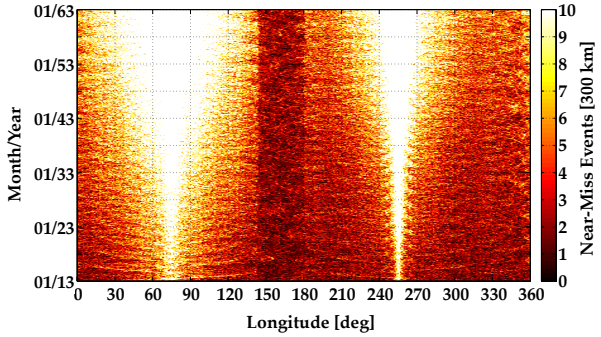


(e) Near-miss events per day (300 km torus).

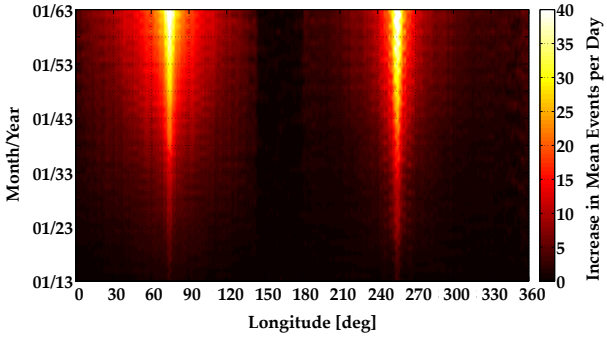


(f) Increase in near-miss events at 300 km.

Figure 4.3: Localized congestion forecasting (50 years) using the linearly-increasing launch traffic model, shown as the number of near-misses per day and increase in number of near-miss events over the idealized "no future launches" scenario, i.e., without augmentation.

intensity of the resulting debris weather trends is amplified as the minor radius increases, especially the localized congestion in the vicinity of the Eastern and Western gravitational wells. Congestion in these critical regions dramatically expands as propagation time progresses, a consequence of the simulated abandonment of controlled assets achieving EOL.

This is a particularly troublesome notion, as operational GEO satellites are typically inserted into longitude slots near the congested gravitational wells: studying Figure 4.1(d), it is evident that the two modes of the bimodal PDF selected for the geocentric longitude distribution are located directly over these two regions of maximum congestion, illustrated in Figure 4.3. At a distance of 50 km, Figure 4.3(a) predicts that assets in 30° longitude windows centered on each gravitational well could experience upwards of 10 near-miss events daily by 2063 in the absence of mitigation measures. This is a striking outcome that begins to corroborate the hypothesis that as the debris population in the GEO regime continues to rise unchecked, the amount of propellant required for routine station-keeping will rise in tandem, to account for the increasing frequency of conjunction events and potential collision avoidance maneuvers. Further, this result has significant implications for satellite insurance in high-risk longitude slots, and rising costs associated with determining whether or not the execution of a dedicated collision avoidance maneuver is even necessary during a conjunction event.

## 4.5 "Business as Usual" Launch Traffic with Mitigation

The congestion forecasting performed thus far in this thesis has not addressed the influence of properly-executed mitigation measures for operational satellites reaching end-of-life. Typical mitigation for the GEO regime incorporates re-orbiting to "graveyard" disposal orbits at perigee altitudes above the GEO ring, factoring the protected GEO zone and area-to-mass-ratio of the satellite into the minimum altitude calculation,[7,10,20] per the re-orbiting guidelines of the Inter-Agency Space Debris Coordination Committee (IADC).[22] Although one might speculate that adherence to these IADC guidelines could increase the risk of derelict collision in the IADC debris orbit that could accumulate above GEO under these guidelines, Reference 23 indicates that the variable amount of residual propellant at end-of-life has driven the wide variety of disposal orbits achieved in practice, such that the creation of a super-synchronous "debris ring" is unlikely. To emphasize the importance of

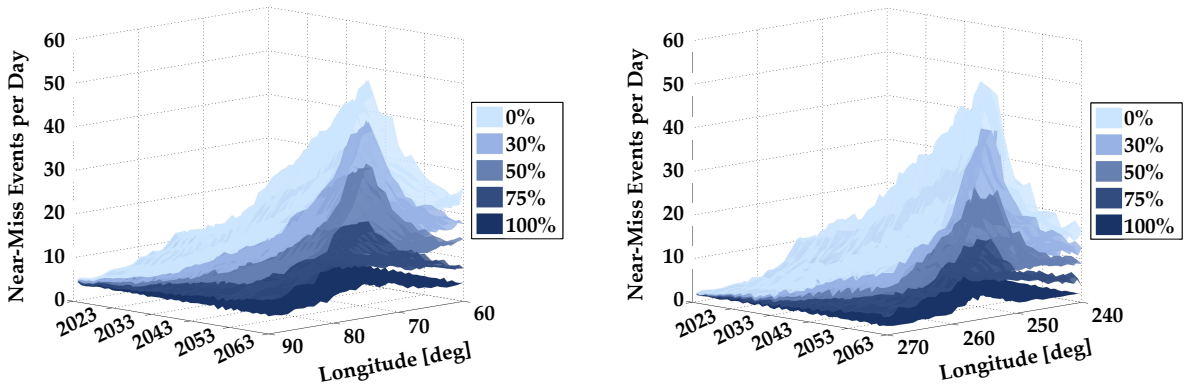


(a) Effect of mitigation on Eastern well congestion. (b) Effect of mitigation on Western well congestion.

Figure 4.4: Effect of perfect mitigation—implemented at various levels of compliance—on long-term, localized congestion in the 30° vicinity of the gravitational wells (300 km torus).

mitigation measures for GEO satellites, this study assumes perfectly-executed mitigation, in which a specified proportion of operational satellites achieving end-of-life are successfully re-orbited to super-synchronous, circular orbits at altitudes that do not interfere with operational assets stationed in the GEO ring during the forecasting periods considered.[6]

Figure 4.4 illustrates the influence of mitigation on localized congestion in the vicinity of the Eastern and Western stable points, for 0% (equivalent to the "business-as-usual" scenario in Figure 4.3), 30%, 50%, 75%, and 100% compliance (equivalent to the "no future launches" scenario), for a torus minor radius of 300 km. Figure 4.4 portrays how the year-averaged number of near-miss events per day at 300 km increases over this 50-year period around the gravitational wells for each of these mitigation scenarios. As the mitigation rate increases, the congestion peaks centered around these gravitational wells successively diminish to the level of the idealized "no future launches" scenario. It is instructive to recall that the case of 30% compliance is the most representative of the rate actually carried out in the GEO regime during the 1997-2003 time frame.[7,11] Of the 103 satellites that achieved end-of-life in this period, 34 were successfully re-orbited to IADC-compliant disposal or-

[6] Reference 29 provides a statistical assessment of the perigee altitude distributions resulting from global adherence to the IADC guidelines, allowing for uncertainties in fuel measurement and maneuver reliability.

bits, 35 attempted re-orbiting, but resulted in orbits with insufficient perigee altitudes, and 34 were abandoned into libration orbits around the gravitational wells.[7] Low compliance may be attributed to (a) the significant propellant cost for meeting the IADC re-orbit guidelines, (b) the difficulties of estimating on-board propellant, and translating the re-orbit $\Delta v$ into required propellant mass,[11] or (c) older satellites that were designed and built before establishment of the IADC guidelines in 1997, for which execution of the re-orbiting burns was not often achievable given, for example, residual propellant and thruster capability.[23]

Recently, Reference 23 praises the strong support of the GEO operator community for preservation of the GEO ring. Of the 160 operational GEO satellites that achieved end-of-life in the period 2001-2010, approximately 80% successfully re-orbited to disposal orbits. Of these satellites, 70% were transferred to orbits at least 200 km above GEO, and almost 50% achieved at least 300 km above GEO, in full compliance with the IADC guidelines.[23] Even with an optimistic mitigation rate of 80%, however, Figure 4.4 predicts that the mean number of near-miss events per day at 300 km in the vicinity of the two gravitational wells will double by the year 2063. Since on-orbit collisions and fragmentation events have not yet been considered, this observed factor of two increase is a lower bound of true congestion increase likely to occur in the GEO environment. Although recent re-orbiting statistics are promising in that they suggest increased adherence to mitigation guidelines—and ultimately growing international desire to safeguard the GEO ring—Figure 4.4 indicates that mitigation alone is not enough to stabilize increasing debris congestion at GEO under current re-orbit success rates. To stabilize projected debris growth at GEO, stricter mitigation measures must be combined with global compliance and proactive remediation initiatives.

## 4.6 Conclusions from Research Goal

Forecasting of localized debris congestion in the GEO ring is performed to quantify the frequency of near-miss events occurring daily for each longitude slot at GEO over a 50 year period, using a representative launch traffic model, operational lifespan, and end-of-

life mitigation compliance rate. Results illustrate that congestion in the vicinity of the two gravitational wells will become severe, provided the mitigation guidelines for this regime are not globally adhered to. Fortunately, a burgeoning desire to preserve GEO is reflected in the increasing numbers of satellite operators attempting re-orbit at end-of-life, but even under this optimistic, present-day mitigation rate of 80%, near-miss events at 300 km in the vicinity of the debris-critical gravitational wells will increase by a factor of two in 50 years. Ultimately, mitigation measures must be combined with active remediation initiatives for the GEO ring, to preserve the long-term usefulness of this valuable driver for space development, and preclude a situation similar to that presently sustained in the LEO regime.[34]

## 4.7 Continuing Research Questions

For continuing research in this area, the following research questions are of interest:

(1) Given that operational GEO lifetimes have increased from ~3 years in the 1960s, to ~7 years in the 1980s, to 15 years currently,[6] what is the effect of increasing satellite lifespans on localized congestion at GEO over the 50 year period, particularly if coupled with the linearly-increasing launch traffic model illustrated in Figure 4.2?

(2) What is the effect of more realistic mitigation on long-term congestion in the vicinity of the gravitational wells? In this chapter, perfectly-executed mitigation is simulated by removing re-orbited objects from propagation – as an improvement, historical re-orbit data can be leveraged to construct PDFs that describe disposal orbit element distributions resulting from fuel uncertainty, maneuver reliability, etc.[29]

(3) What is the effect of environmental remediation—active debris removal—on long-term congestion in the vicinity of the gravitational wells? How many objects need to be removed per year to stabilize congestion increases given an increasing launch traffic model, increasing satellite lifespans, and stable mitigation compliance rate?

# Chapter 5

## *Research Goal 2(b)*: Forecasting longitude-dependent congestion at GEO arising from on-orbit fragmentation events

### 5.1 Overview of Research Goal

Of critical importance is a thorough understanding of the consequences that on-orbit explosions and debris-debris or debris-satellite collisions, collectively classified as *fragmentation events*, have on longitude-dependent congestion throughout the GEO regime. This knowledge is especially important, since although two historical fragmentation events at GEO have been documented—the 1978 explosion of the Ekran-2 satellite, and the 1992 explosion of a Titan III-C transtage[11]—significant populations of objects with diameters as small as 10-15 cm have been detected in optical observations of the GEO ring, and are indicative of undocumented fragmentation events in this regime.[11,17,18] Although no known historical collision events have been documented at GEO, potential impact-induced anomalies have been observed in both the GEO ring and the super-synchronous GEO graveyard regime.[54] Fragmentations on-orbit are triggered by accidental mixing of hypergolic fuels, overheating of residual (non-vented) propellants, mechanical valve failures, hypervelocity impacts, or other unknown or unattributed causes.[56]

Although the literature strongly focuses on the effects of debris-generating fragmentation events in low-Earth orbit (LEO), several previous studies have been devoted to quantifying increases in collision risk driven by fragmentations in the GEO ring. Reference 30 harnesses momentum and energy principles to model hypervelocity impacts, and predicts

that the resulting fragment cloud remains close to the GEO belt, spreading longitudinally to all regions of the GEO ring within weeks. Reference 31 considers a probable conjunction scenario at GEO to show that the fragment energy distribution resulting from breakup is sufficient for permeating all orbit regimes from re-entry through super-synchronous. Recently, Reference 32 indicates that although close approach velocities for the GEO regime are in general lower than in the LEO regime, a low-energy breakup over one of the gravitational wells could be a worst-case scenario in that resonance could be preserved for most of the fragment population, serving to increase collision risk with operational assets at these longitudes. While the tools that the authors of these previous studies harness for characterizing breakup events at GEO differ, the independent conclusions of each study agree that fragmentations at the GEO altitude have long-term consequences that are detrimental to the sustainability and continuing usefulness of this unique regime. In addition to these environmental consequences, a fragmentation event at GEO and the effects thereof could hinder the high-value services of operational assets, increase insurance costs for operators with assets in higher-risk longitude slots, and engender political repercussions, as well.[31]

It is critical to determine whether the longitude of the parent body at the fragmentation epoch renders the localized effects of the break-up more or less severe for operational assets in higher-risk longitude slots, especially those in the vicinity of the two gravitational wells at 75°E and 105°W. As will be demonstrated, on-orbit fragmentation in the GEO ring has the potential to generate significant localized congestion, dependent on both the longitude and altitude at which the fragmentation occurs. This research therefore fills a void in the literature by addressing fragmentation analyses at GEO from the perspective of the Earth-fixed frame, and not inertial space, which has typically been used for fragmentation analyses in both the LEO and GEO regimes (see, for example, References 30 and 31). On-orbit fragmentations in a variety of representative GEO break-up scenarios are simulated to investigate short and long-term contributions to nominal, baseline congestion occurring on a slot-dependent basis for each of the longitude slots at GEO. As the debris population

continues to increase—especially as a result of fragmentation events—the amount of propellant required to maintain a designated longitude slot while simultaneously executing avoidance maneuvers, and the costs associated with reviewing conjunctions to determine if evasive action is even warranted, will begin increasing in tandem. From the perspectives of this research, the significance and implications of on-orbit fragmentations at GEO will be cast in a new light, to impel continued research in this critical and highly relevant area.

## 5.2 Fragmentation Model

Fragmentation particulates are generated using the NASA Standard Breakup Model, developed for NASA's long-term debris environment modeling software EVOLVE 4.0[46] and validated against catalogued debris clouds and ground-based experimental results for particles larger than 1 mm.[11] The NASA model uses an empirical power law to determine the cumulative number of fragments larger than the user-defined effective diameter $l_c$ that are generated during fragmentation. For explosions, the cumulative number of fragments $N_f$ is independent of the mass of the parent body, and is given by

$$N_f(d \geq l_c) = 6 c_s l_c^{-1.6} \tag{5.1}$$

where $d$ is fragment diameter, $l_c$ the effective diameter defined in meters, and $c_s$ a unitless, empirical correction for catalogued fragmentation events.[11] For this study, the correction $c_s = 1.0$ is assumed.[1] For collision events, $N_f$ is a function of the target and impactor mass and collision velocity:[11]

$$N_f(d \geq l_c) = 0.1 \hat{m}^{0.75} l_c^{-1.71} \tag{5.2}$$

where the mass-dependent factor $\hat{m}$ is defined as

$$\hat{m} \equiv \begin{cases} m_t + m_p \text{ [kg]} & \text{for } \tilde{E}_p \geq \tilde{E}_p^* \quad \text{[catastrophic]} \\ (m_p v_i)/1000 \text{ [kg m/s]} & \text{for } \tilde{E}_p < \tilde{E}_p^* \quad \text{[non-catastrophic]} \end{cases} \tag{5.3}$$

[1] Reference 46 indicates this relationship is valid for launch vehicle upper stages with mass 600-1000 kg, and introduces this correction factor to account for known debris from catalogued explosions of other parent body masses and types.

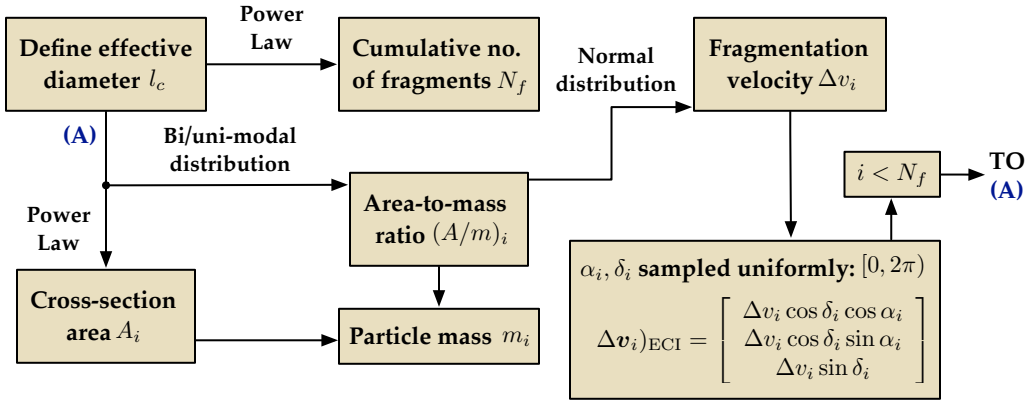


Figure 5.1: Flow-chart for computer implementation of NASA Standard Breakup Model.

where $m_t$ and $m_p$ are the target and impactor masses, respectively, $v_i$ is the impact speed, $\tilde{E}_p = 0.5 m_p v_i^2 / m_t$ is the specific energy of the impactor, and $\tilde{E}_p^* \equiv 40$ kJ/kg is the energy threshold for a catastrophic collision.[11] For all effective diameters $l_c > 11$ cm, a bi-modal probability distribution is used for sampling the area-to-mass ratio of every fragment. For $l_c < 8.0$ cm for spacecraft fragments, and $l_c < 1.7$ cm for upper stage fragments, a single-mode normal distribution is employed.[11] For effective diameters in the "definition gap" of 8-11 cm for spacecraft and 1.7-11 cm for upper stages, a pseudo-random number on [0,1] is generated to determine if the bi-modal or single-mode distribution should be utilized.[11] The cross-sectional area for each fragment is then determined as an explicit function of the effective diameter $l_c$, and the fragmentation delta-velocity $\Delta v_i$ applied to each fragment is sampled from a normal distribution on the area-to-mass ratio.[46] Figure 5.1 illustrates a flow-chart for using the NASA model – for more details regarding implementation, and for the parameters utilized in the bi-modal and single-mode area-to-mass ratio and delta-velocity distributions in the model, see References 11 and 46.

Note that for both explosion and collision events, the delta-velocity $\Delta v_i$ is applied in a random direction sampled over the unit sphere for each fragment. For this study, right ascension $\alpha_i$ and declination $\delta_i$ angles are sampled uniformly over the unit circle, and these angles are translated into a unit vector direction with spherical coordinates (cf. Figure 5.1).

Note that the resulting unit vector distribution is not uniform – rather, it exhibits slight bias towards the poles.[2] In the event of a collision, the number of fragments in each generated debris cloud is proportional to the mass fractions of the target and impactor, e.g., the target cloud receives $[m_t/(m_t + m_p)]N_f$ fragments, and the impactor cloud $[m_p/(m_t + m_p)]N_f$ fragments, such that each cloud receives $0.5N_f$ fragments inasmuch as $m_t = m_p$. Since the objective of this study is to investigate the longitude-dependent effects of fragmentations at GEO—and not the accuracy of the fragmentation model itself—these assumptions are appropriate for the scope of this research objective.

## 5.3 Longitude-Dependent Effects of Fragmentations at GEO

The longitude-dependent congestion generated by the fragmentation of a rocket body (R/B) over one of the gravitational wells at 75°E and 105°W is characterized by applying the fragmentation model outlined in Section 5.2 to a simulated rocket body positioned in various longitude slots at the GEO altitude. Reference 32 hypothesizes that a lower-energy fragmentation over one of the two gravitational wells could be a worst-case scenario in that resonance is preserved for the majority of the fragmentation particulates, resulting in frequent near-misses with operational assets in the vicinity of these critical longitudes. The results of this current study will illustrate that this hypothesis of Reference 32 is exactly the case—not only does longitude-dependent congestion increase as a function of the number of fragments captured by the gravitational well, but these localized congestion increases are predictable to first-order both in longitude and time since fragmentation. First, theory introduced by Reference 4 that provides the mathematics necessary for predicting libration parameters based on initial longitude and longitudinal drift rate $\dot{\lambda}$ is presented. These parameters are combined with a harmonic oscillator model to give a first-order, analytical formulation of the resulting libration motion of fragments captured by a gravitational well.

[2] Although the direction of the delta-velocity vector $\Delta \boldsymbol{v}_i$ is central to the instantaneous change in orbital elements experienced during fragmentation, it is ultimately the coupling between magnitude and direction that determines whether a fragment will circulate around the GEO arc or librate around a gravitational well.

### 5.3.1 Harmonic Oscillator Model of Libration Motion

Using the change of origin $\psi \equiv \lambda - \lambda_{1,2}$, where $\lambda$ and $\lambda_{1,2}$ denote geocentric longitude of the object and gravitational well, respectively, the condition for stable point "capture" is expressed to first-order as[4]

$$\|\dot{\psi}_0\| < k\|\cos\psi_0\| \tag{5.4}$$

where $\dot{\psi}_0 = n_0 - n_{\text{GEO}}$ is the initial longitudinal drift rate—a function of the initial semi-major axis only—and $k$ is an angular-velocity-like parameter dependent upon the $J_{2,2}$ sectorial harmonic and defined as[4]

$$k \equiv \frac{6n_{\text{GEO}}R_{\oplus}\sqrt{J_{2,2}}}{r_{\text{GEO}}} \tag{5.5}$$

Using the coefficient $J_{2,2} \equiv \sqrt{C_{2,2}^2 + S_{2,2}^2} \approx 1.82 \times 10^{-6}$ derived from the EGM-96 model,[3] the parameter $k \approx 8.92 \times 10^{-8}$ rad/s.[11] Following Reference 4, the amplitude and period of libration for objects that satisfy the capture condition in Equation (5.4) are approximated by the two formulas:

$$\sin\psi_m = \sqrt{\sin^2(\psi_0) + \frac{\dot{\psi}_0^2}{k^2}} \tag{5.6}$$

$$T_l = \frac{4}{k}K(\sin\psi_m) \tag{5.7}$$

where $\psi_m$ denotes the libration amplitude, $T_l$ is the period of libration, and $K(\sin\psi_m)$ is the complete elliptic integral of the first kind.[4] Note that Equations (5.6)-(5.7) are derived assuming the $J_{2,2}$ term only – higher-order harmonics appearing in a full expansion of the Earth's gravitational potential are neglected. Since the propagator harnessed in this thesis uses a $4\times4$ gravitation model, Equations (5.6)-(5.7) provide a first-order approximation for the libration characteristics observed in numerical simulations. Nonetheless, these formulas can be used in tandem with a harmonic oscillator model to rapidly predict libration motion to first-order, i.e., under the $J_{2,2}$ perturbation alone. If oscillatory motion is assumed,

[3] Coefficients for the EGM-96 model are available at: `http://cddis.nasa.gov/926/egm96/egm96.html`

the longitudinal motion of a captured object can be expressed as

$$\lambda(t) = \psi_m \cos\left(\frac{2\pi t}{T_l} - \phi\,\mathrm{sgn}(\dot{\psi}_0)\right) + \lambda_{1,2} \tag{5.8}$$

where the phase shift $\phi$ is determined with

$$\phi = \arccos\left(\frac{\psi_0}{\psi_m}\right) \tag{5.9}$$

Note that the sign of the initial longitudinal drift rate $\dot{\psi}_0$ is included to switch the sign of the phase angle $\phi$ accordingly, such that the resulting sinusoidal longitude profile reflects the initial east/west drifting direction of the particle. The accuracy of this harmonic oscillator model for predicting the libration motion of fragments captured by a gravitational well in the aftermath of a fragmentation is explored in Section 5.3.3.

### 5.3.2 Rocket Body Explosions over Gravitational Wells

To assess longitude-dependent debris congestion generated by explosions at the GEO altitude, the NASA Standard Breakup Model is applied to generate fragmentation debris with $l_c > 5$ cm resulting from the explosion of a simulated R/B. The initial conditions are selected to position this R/B at various longitudes surrounding the east/west gravitational wells at the simulated explosion epoch of 00:00:00 Zulu on 01 September 2013. From Equation (5.1), the NASA model predicts that 724 fragments larger than 5 cm are generated in the explosion. The fragmentation delta-velocity for each fragment is applied in a random direction sampled over the unit sphere, and is applied to the inertial velocity vector of the simulated R/B initial conditions $a = r_{\mathrm{GEO}}$, $e = 0.001$, $i = \Omega = M_0 = 0°$, with argument of perigee $\omega$ chosen such that the R/B is positioned at the desired longitude, i.e., $\omega = \alpha_G + \lambda_0$, where $\alpha_G$ is the right ascension of Greenwich at the explosion epoch.[2]

Figure 5.2 provides the characteristics of the resulting fragment distribution for the case $\lambda_0 = 60°$E. Figure 5.2(a) is a Gabbard plot that highlights the resulting perigee/apogee radius spread as a function of semi-major axis, normalized by the GEO radius. Figure 5.2(b)

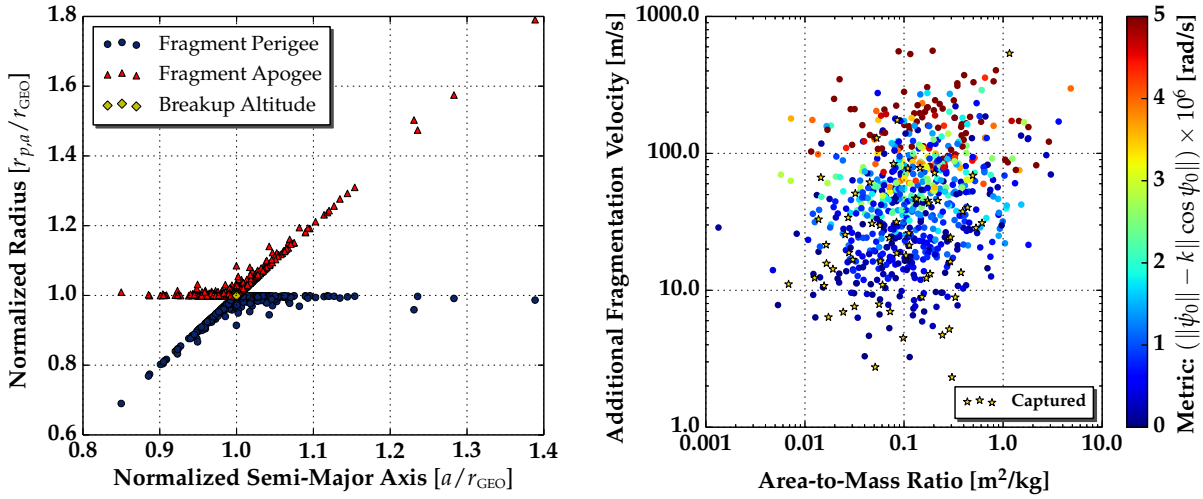


(a) Gabbard diagram for R/B explosion at 60°E. (b) Fragment distribution for R/B explosion at 60°E.

Figure 5.2: Characteristics of fragmentation distribution for simulated explosion at 60°E.

shows the area-to-mass ratio and fragmentation delta-velocity distribution, colored by the capture metric in Equation (5.4). In this case, 60/724 fragments are captured by the gravitational well at 75°E, and of these, 57 are ejected at fragmentation delta-velocities less than 100 m/s, and three at delta-velocities larger than 100 m/s. This indicates that the direction of the fragmentation delta-velocity vector for these higher-speed fragments is opposite the direction of the parent body's velocity vector. Furthermore, Figure 5.2(b) illustrates that area-to-mass ratios consistent with the definition of the high area-to-mass ratio (HAMR) objects observed in the GEO regime[4] are sampled via the NASA Standard Breakup Model. This underlies the importance of including SRP in the force model, which is a dominating perturbation to the long-term motion of both HAMR objects and fragmentation debris.[58]

Five-year congestion forecasts for simulated R/B explosions occurring at 45°E, 60°E, and at the Eastern gravitational well at 75°E are illustrated in Figure 5.3 for a torus minor radius of $\tilde{r} = 100$ km. Note that 54, 60, and 69 of the 724 generated fragments are captured by the Eastern gravitational well in each scenario, respectively, and begin librating around

[4] HAMR objects are defined as having area-to-mass ratios from 0.1-20 m$^2$/kg and above, and are widely studied in the literature, e.g., in References 57 and 58.

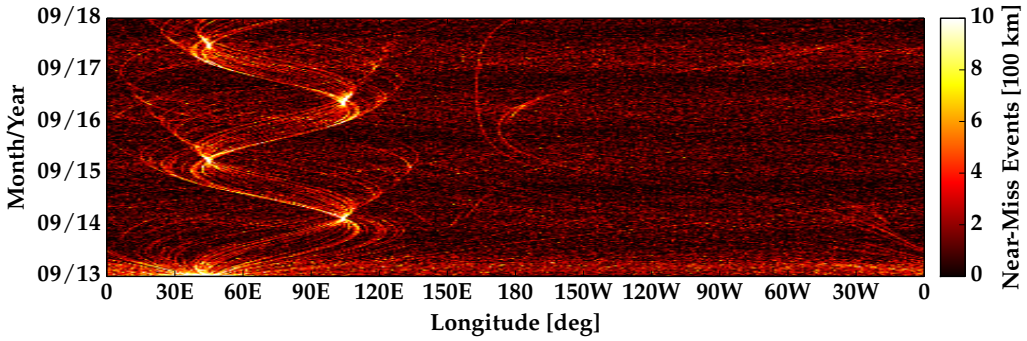


(a) Five-year congestion forecast for simulated explosion at 45°E ($\tilde{r} = 100$ km).

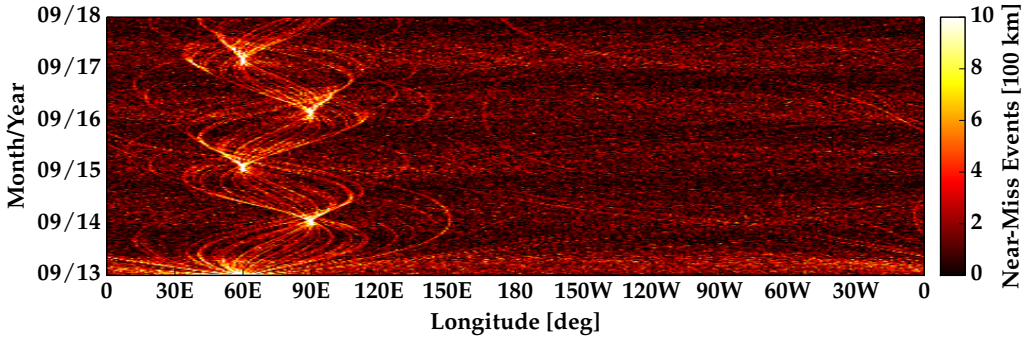


(b) Five-year congestion forecast for simulated explosion at 60°E ($\tilde{r} = 100$ km).

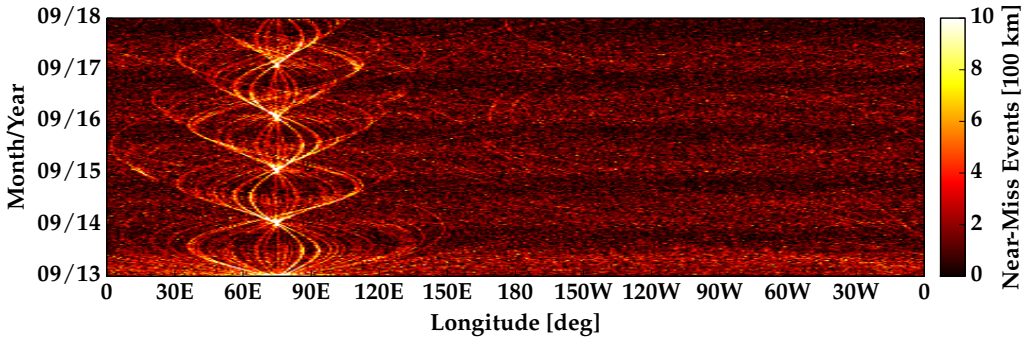


(c) Five-year congestion forecast for simulated explosion at 75°E ($\tilde{r} = 100$ km).

Figure 5.3: Five-year longitude-dependent congestion forecasts for simulated rocket body explosions in the vicinity of the Eastern gravitational well (torus minor radius of 100 km).

this critical longitude. As a consequence, bi-annual "debris storms"— dramatic increases in localized congestion—manifest at the longitudinal extents of the parent body's libration motion. This outcome is predicted by Equation (5.6), which states that $\psi_0 = \psi_m$ if $\dot{\psi}_0 = 0$, that is, the libration amplitude is equivalent to the initial deviation from the gravitational

well inasmuch as $a = r_{\text{GEO}}$ at the explosion epoch. The congestion forecasts in Figure 5.3 illustrate that the resulting oscillations in longitude exhibited by the captured fragments synchronize in approximately one-year intervals at the libration amplitudes of the parent body over the five-year prediction span. Therefore, this is critical knowledge not only for operators with satellites in longitude slots at or near the fragmentation longitude $\lambda_0$, but also for those with satellites in longitude slots $\pm 2\psi_m$ away from $\lambda_0$ (i.e., in the direction of the gravity well). Note that the resulting background noise from the drifting fragments not captured by the gravitational well exhibits a once-yearly banding phenomenon driven by once-yearly oscillations in the eccentricity magnitude induced by SRP, the effects of which are more pronounced as a consequence of higher area-to-mass ratios (cf. Figure 5.2(b)).[3,59]

Figure 5.4 provides a zoomed-in, one-year view of the five-year congestion forecast in Figure 5.3(b). Curvilinear traces of the fragments captured by the gravitational well are clearly visible, in addition to the linear traces of the higher-energy fragments that surpass capture and begin circulating around the GEO arc, with eastward drift for semi-major axes below the GEO ring, and westward drift for semi-major axes above GEO.[13] Figure 5.5(a) shows the 60°E case in Figure 5.3(b) propagated for 30 years to illustrate localized congestion trends occurring over this longer time scale. Longitudinal focusing, although prominent for the first five years, begins to diffuse during 5-10 years, leading to a lull in localized

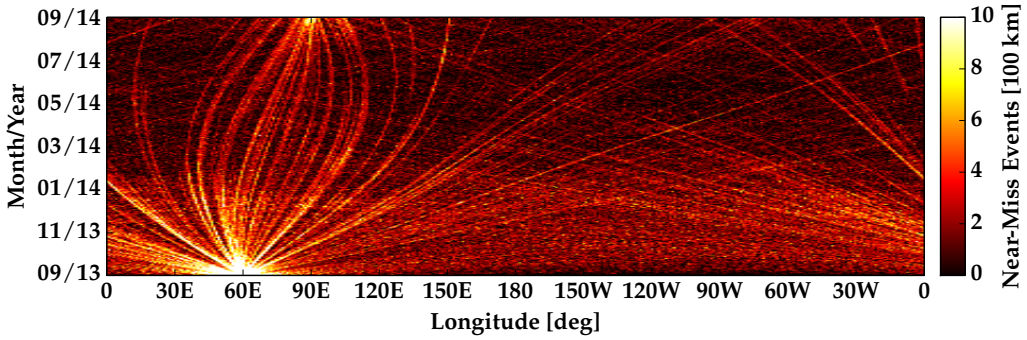


Figure 5.4: One-year longitude-dependent congestion forecast for simulated rocket body explosion at 60°E (torus minor radius of 100 km).

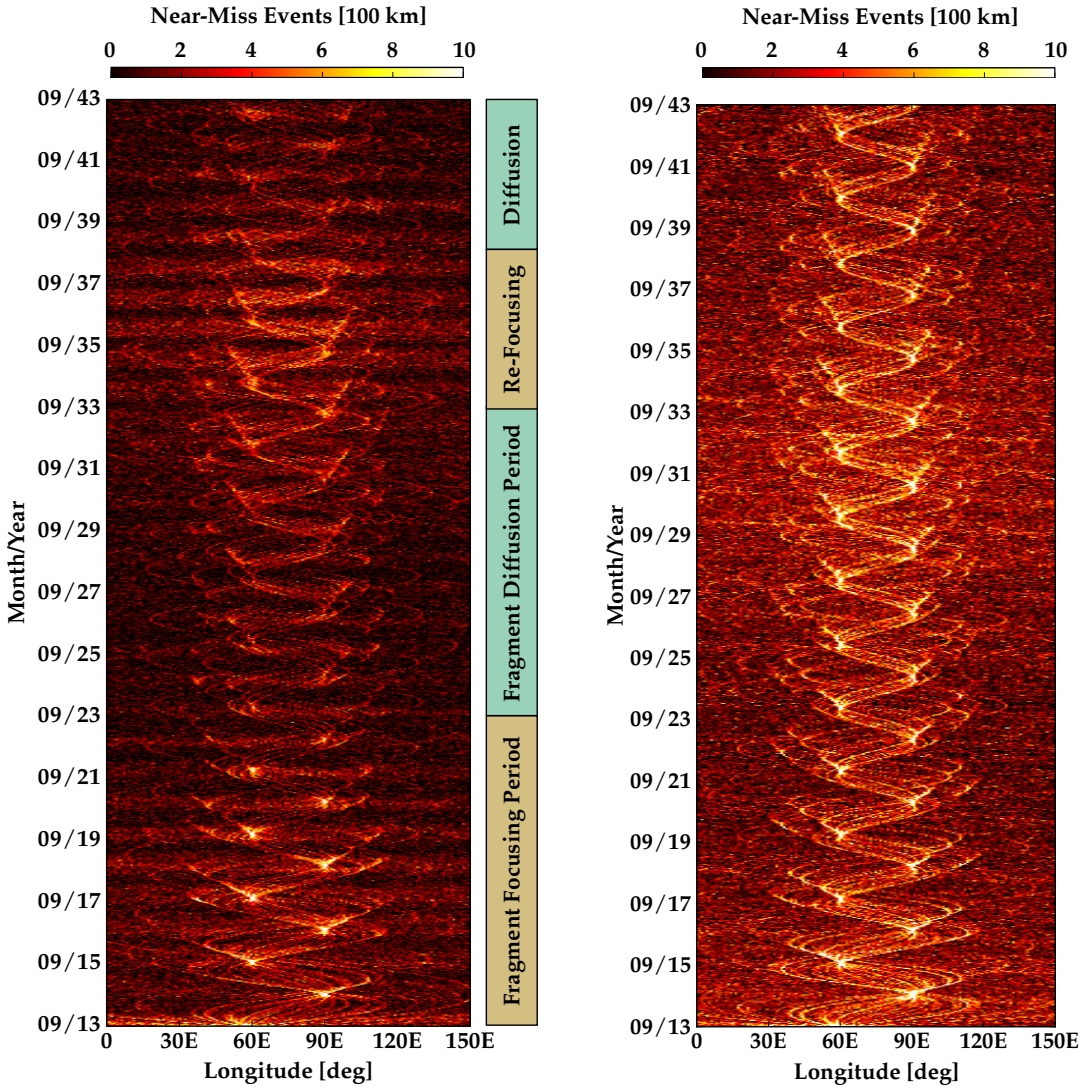


(a) Propagation under $4 \times 4$ gravity, luni-solar perturbations, and SRP (i.e., full force model).

(b) Propagation under $4 \times 4$ gravity only.

Figure 5.5: Longitude-dependent congestion forecast (30 years) for simulated rocket body explosion at 60°E (torus minor radius of 100 km), using full and Earth gravity force models.

congestion levels during 10-20 years. From 20-25 years, the librating fragments begin refocusing into a characteristic oscillatory pattern, but the intensity of these residual fragment storms is beneath that observed during the first five years following the explosion. After 25 years, the librating fragments (and resulting local congestion spikes) once again diffuse.

Analysis of simulation results indicates the mechanism for this long-term focusing,

diffusion, and re-focusing phenomenon is a combination of long-period luni-solar effects and SRP-induced eccentricity variations prevalent in the GEO ring. If these perturbations are removed from the force model, such that the 30-year propagation uses $4 \times 4$ gravitation only, the localized congestion forecast in Figure 5.5(b) appears. In this situation, fragment diffusion and re-focusing is not observed; rather, strong focusing at the libration amplitude persists throughout the entire 30-year simulation. This result emphasizes a conclusion of Reference 32 that luni-solar and SRP perturbations are critical for analyzing fragmentation events at GEO over durations longer than one year.

Figure 5.6 illustrates that similar focusing effects can occur for fragments captured by the Western gravitational well. For simulated R/B explosions at 75°W, 90°W, and at the Western gravitational well at 105°W, 58, 67, and 66 of the 724 ejected fragments are captured in each case, respectively. Although the number of captured fragments in each case is similar to the number captured in the Eastern well simulations illustrated in Figure 5.3, the intensities of the fragment focusing events are not as strong as the equivalent Eastern well scenarios, e.g., for $\psi_0 = 30°$, cf. Figures 5.3(a) and 5.6(a). For completeness, Figure 5.7 illustrates the five-year congestion resulting from an explosion at 165°E, a well-known unstable equilibrium longitude positioned halfway between the stable gravitational wells. In this situation, none of the 724 ejected fragments are captured by either gravitational well under the metric in Equation (5.4). However, curvilinear traces observed in Figure 5.7 indicate that several fragments begin oscillating about both the gravitational wells, behavior indicative of class L3 objects (recall Table 2.1).

### 5.3.3 Accuracy of Harmonic Oscillator Model

It is interesting to assess if the harmonic oscillator model in Equations (5.8)-(5.9) can accurately predict the longitudinal focusing observed in the five-year congestion forecasts in Figures 5.3 and 5.6. Fragment focusing at the longitudinal extents appears predictable both in longitude and time since fragmentation, such that a first-order model for forecast-

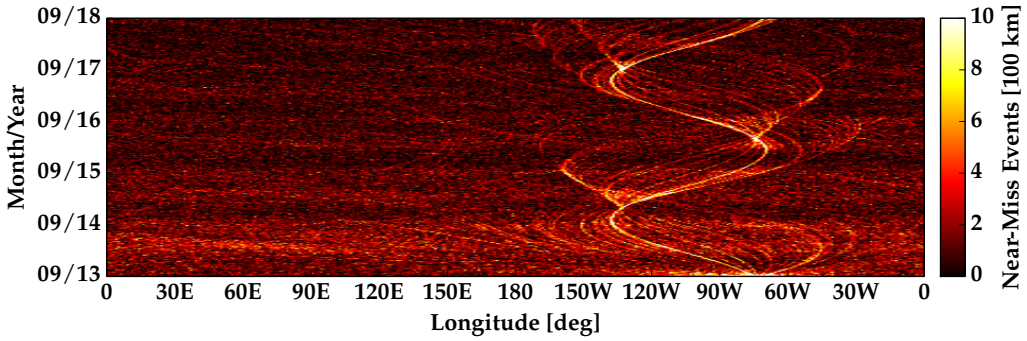


(a) Five-year congestion forecast for simulated explosion at 75°W ($\tilde{r} = 100$ km).

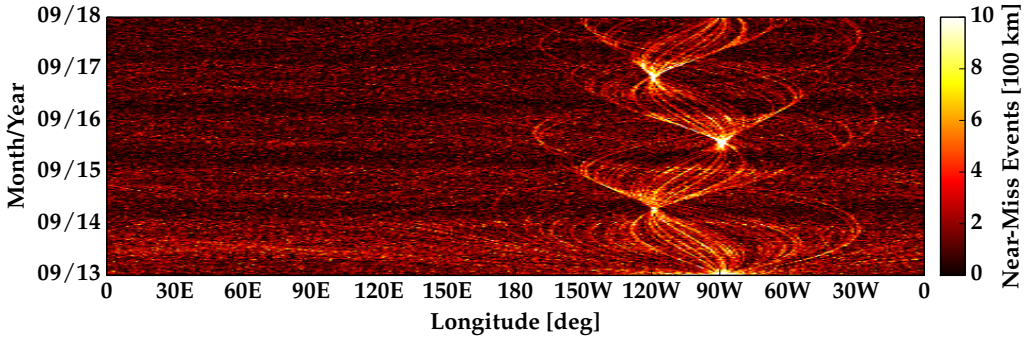


(b) Five-year congestion forecast for simulated explosion at 90°W ($\tilde{r} = 100$ km).

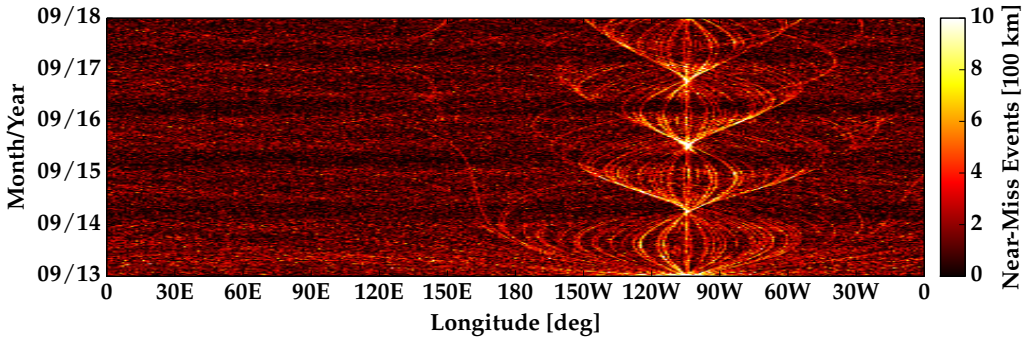


(c) Five-year congestion forecast for simulated explosion at 105°W ($\tilde{r} = 100$ km).

Figure 5.6: Five-year longitude-dependent congestion forecasts for simulated rocket body explosions in the vicinity of the Western gravitational well (torus minor radius of 100 km).

ing these debris storms with minimal knowledge of the fragment distribution is desirable. If the semi-major axes $a_i$ for the resulting fragment orbits in the aftermath of a fragmentation can be reasonably estimated, $\dot{\psi}_{0,i}$ is a known initial condition, and Equations (5.6)-(5.7) can be harnessed to compute the amplitude and period of libration for fragments captured

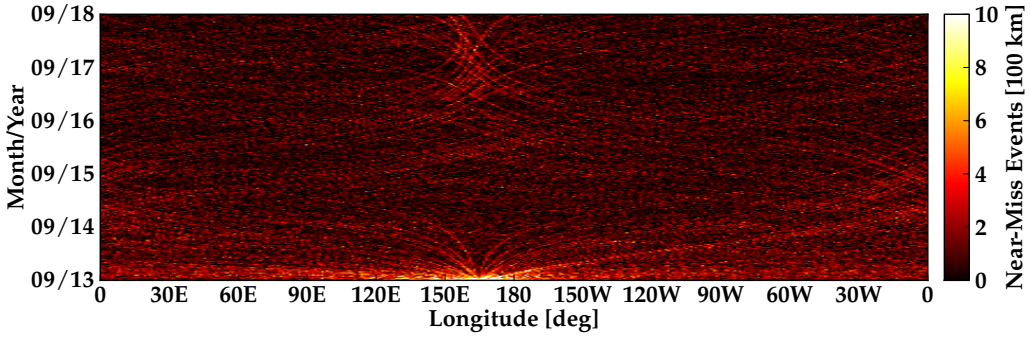


Figure 5.7: Five-year longitude-dependent congestion forecast for simulated rocket body explosion at 165°E (torus minor radius of 100 km).

via Equation (5.4). Longitude histories for these fragments are thus predicted analytically as a function of elapsed time using Equations (5.8)-(5.9), and overlaid to forecast (to first-order) when and where fragment focusing will occur following a fragmentation at GEO.

Figure 5.8 illustrates the accuracy of this harmonic oscillator model, showing comparisons between analytical longitude histories predicted using the model in Figure 5.8(a), simulated longitude histories under the $J_{2,2}$ harmonic only in Figure 5.8(b), and simulated longitude histories under full forcing (i.e., $4 \times 4$ EGM-96 gravity, luni-solar perturbations, and SRP) in Figure 5.8(c). As expected, the harmonic oscillator approximation agrees well with simulated longitudes under $J_{2,2}$ only, as this was the assumption made in the derivation of Equations (5.6)-(5.7). When compared against "truth" longitude histories for the 60 librating fragments in Figure 5.8(c), however, discrepancies exist not in the longitudinal location of the fragment focusing events, but in the times at which these focusing events occur. As errors in timing accumulate with time elapsed since fragmentation, this harmonic oscillator model should only be considered for short-term, 1-2 year predictions. Following this time span, dominating perturbations in the GEO environment that are not accounted for in the harmonic oscillator approximation begin influencing the libration motion of the fragments, and this first-order, $J_{2,2}$-only approximation diverges.

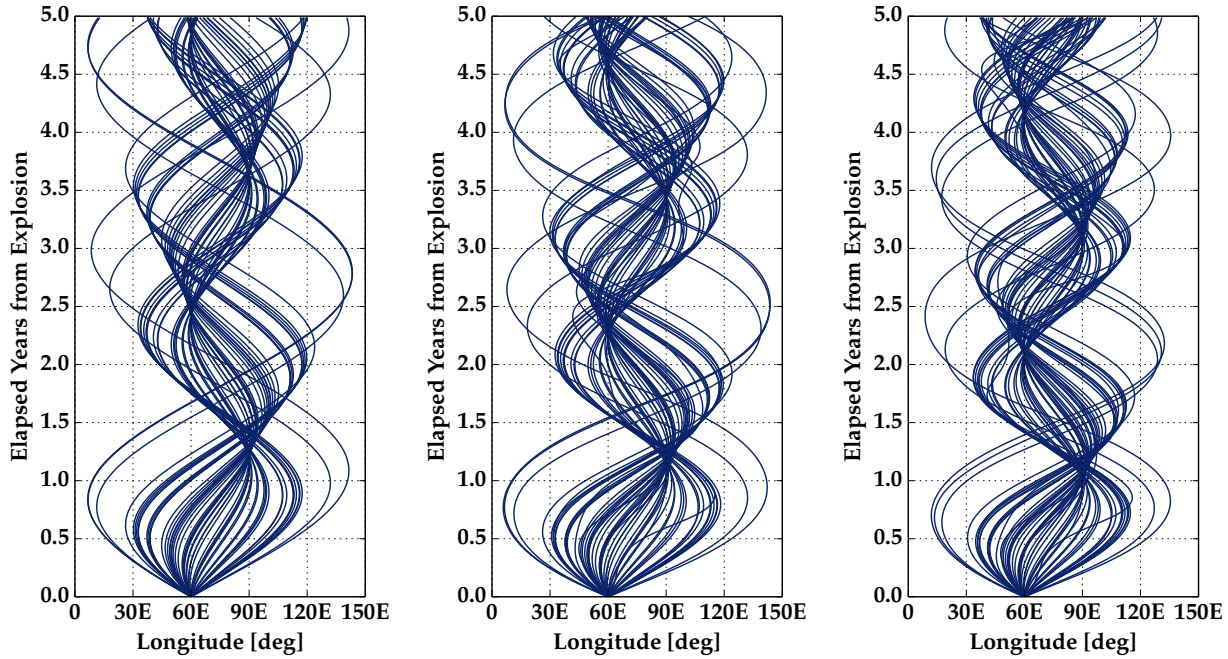


(a) Harmonic oscillator model. (b) Under $J_{2,2}$ harmonic only. (c) Under full GEO force model.

Figure 5.8: Longitude histories for the 60 librating fragments captured by the gravitational well at 75°E, computed with the harmonic oscillator model, simulated under $J_{2,2}$ only, and simulated using full GEO forcing.

### 5.3.4 Rocket Body Collisions over Gravitational Wells

Finally, the longitude-dependent congestion signature of collision events in the GEO regime is evaluated. Reference 32 indicates that since orbital velocities are lower for GEO—and objects are orbiting in the same direction—relative velocities are generally more benign for GEO than for LEO. Thus, according to Equation (5.2), although fewer fragments will be generated for a GEO collision event than for an equivalent event at LEO, peak risk potential increases as a result of a lower-mean fragmentation delta-velocity distribution.[32] For this study, three collisions near the Eastern gravitational well are simulated: (a) collision due to inclination difference $\Delta i$, (b) collision due to eccentricity difference $\Delta e$, and (c) collision between a GEO object and one in geostationary transfer orbit (GTO). For all scenarios, two 2000 kg upper stages are assumed to collide at 60°E, using the initial conditions

for the target R/B selected for the explosion cases shown in Section 5.3.2. Simulation results are highlighted in Table 5.1, and the five-year localized congestion forecasts for each collision scenario are provided in Figure 5.9.

Table 5.1: Simulation results for three collision scenarios between two 2000 kg upper stages at 60°E, where NC and C denote non-catastrophic and catastrophic collisions, respectively.

| **Collision Scenario Description** | **Collision Speed** | $N_f$ **(Captured)** |
|---|---|---|
| Inclination difference $\Delta i = 2.0°$ | 0.107 km/s (NC) | 941 (61) |
| Eccentricity difference $\Delta e = 0.05$ | 0.157 km/s (NC) | 1251 (71) |
| At apogee of 200 km $\times$ 35744 km GTO | 1.479 km/s (C) | 8439 (218) |

The first two collision scenarios are non-catastrophic according to the specific energy defined in Equation (5.3), and a smaller proportion of fragments are captured by the gravitational well for both of these cases than for the 60°E explosion (6.5% and 5.7% are captured for the inclination and eccentricity difference collisions, respectively, compared to the 8.3% captured in the explosion). This is largely a consequence of the fragmentation velocity distribution in the NASA Standard Breakup Model, which defines a higher mean $\Delta v$ for collision events than for explosion events.[46] In the third simulated collision event—defined as catastrophic according to Equation (5.3)—a mere 2.6% of the staggering 8439 fragments larger than 5 cm in diameter are captured by the gravitational well at 75°E.

Figure 5.9 shows that the localized congestion forecasts generated by collision events qualitatively appear to be similar to the macroscopic trends exhibited by explosion events, even though two separate fragment clouds exist in the former, and only a single cloud of ejecta is generated in the latter. The significant increase in the number of near-miss events at 100 km for the GEO-GTO collision (cf. Figure 5.9(c)) is a consequence of the large number of fragments ejected in this catastrophic collision event. Longitudinal bunching at the libration amplitude of the target R/B is still observed with similar periodicity in all three collision scenarios, although localized congestion during a bunching event in Figure 5.9(c) is a factor of four times more intense than for the inclination and eccentricity difference

scenarios in Figures 5.9(a)-5.9(b). These results indicate that longitude-dependent effects of explosions and collisions at GEO are approximately equivalent in characteristic, differing strictly by the number of fragments captured by the gravitational well in each scenario.

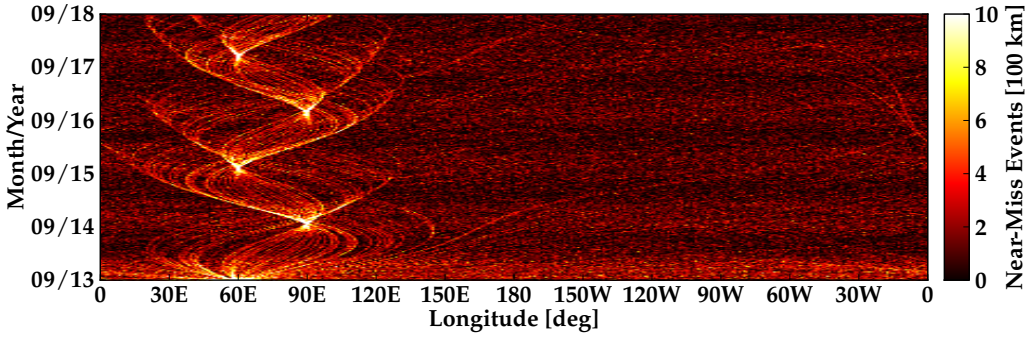


(a) Five-year congestion forecast for simulated collision at 60°E (inclination difference).

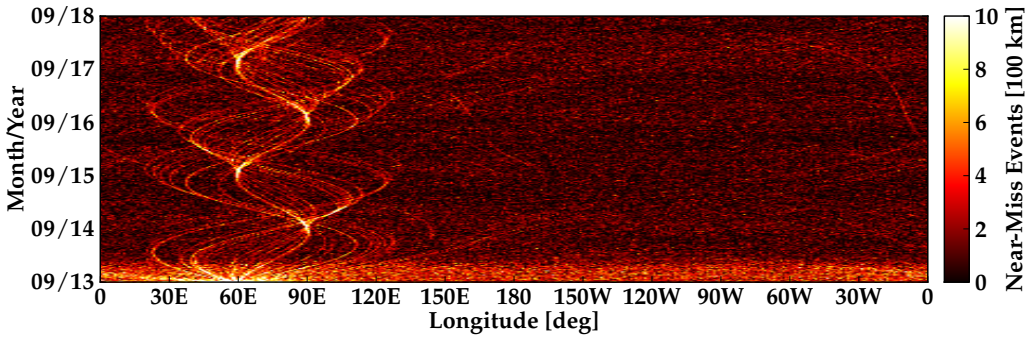


(b) Five-year congestion forecast for simulated collision at 60°E (eccentricity difference).

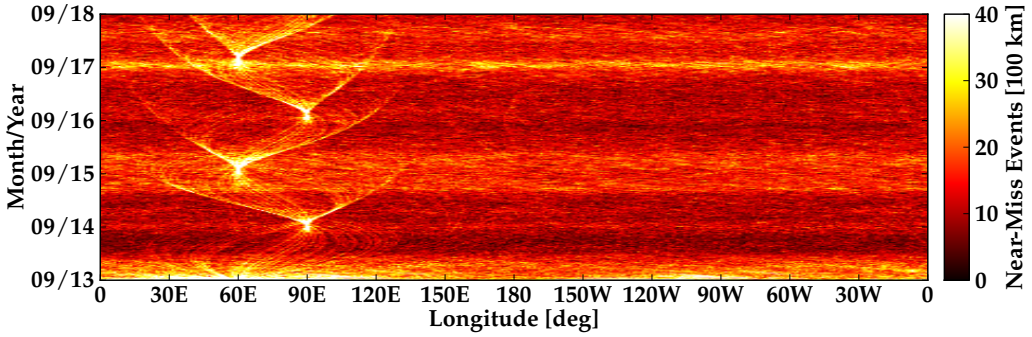


(c) Five-year congestion forecast for simulated collision at 60°E (GEO-GTO collision).

Figure 5.9: Five-year longitude-dependent congestion forecasts for simulated rocket body collisions in the vicinity of the Eastern gravitational well (torus minor radius of 100 km).

## 5.4 Conclusions from Research Goal

The effect of on-orbit fragmentations on longitude-dependent congestion in the GEO regime is investigated by simulating explosions and collisions of uncontrolled rocket bodies in various orbit configurations, including libration about one or both of the stable longitudes at the GEO altitude. Applying the NASA Standard Breakup Model in tandem with the near-miss event metric, short- and long-term localized congestion patterns are rapidly forecasted to investigate how strongly the severity of a GEO fragmentation event depends on the longitude of the parent body at the breakup epoch. Simulation results indicate that on-orbit GEO fragmentations in the vicinity of one of the critical gravitational wells spawn bi-annual debris storms at the longitudinal extents of the parent body's libration motion. Provided the semi-major axis distribution for a GEO fragmentation can be reasonably estimated using tracking data, longitudes and times at which dramatic increases in congestion will occur can be predicted to first-order, applying the harmonic oscillator formulation for time scales of less than five elapsed years since fragmentation.

For all fragmentation cases, the level of existing TLE background noise is achieved or surpassed only during the observed longitudinal focusing. The intensity of these longitude-dependent debris storms is proportional to the number of particles captured by the nearest gravitational well, however, and thus could readily overtake background congestion levels if higher-energy collisions are considered (as in the scenario of the GTO apogee collision), or if fragment sizes smaller than 5 cm are included. Ultimately, this chapter highlights the importance of energy passivation at end-of-life – satellites and upper stages not appropriately prepared for disposal during decommissioning are prone to fragmenting and generating a fragment cloud that threatens severe consequences for operational assets at GEO.

## 5.5 Continuing Research Questions

For continuing research in this area, the following research questions are of interest:

(1) The NASA Standard Breakup Model is an empirically-derived fragmentation model that does not satisfy conservation of mass or conservation of energy. What are the effects of a more realistic breakup model on the longitude-dependent congestion signature resulting from GEO fragmentation events studied in this chapter, if any?

(2) The cannonball SRP model is applied to the fragments propagated in this chapter, but this approximation is unrepresentative for widely-varying fragment geometry in the aftermath of a breakup. How would a more accurate force model—coupled with fragment attitude motion—affect the longitude-dependent congestion trends illustrated in this chapter, especially over longer time scales (recalling Figure 5.5)?

(3) Can the harmonic oscillator model for fragment libration be modified—via a scaling factor, for example—to account for luni-solar and SRP forcing not modeled by this analytic formulation, i.e., can the time scale over which it is valid be extended?

(4) Can fragments exhibiting correlated congestion signatures be back-propagated to identify a common fragmentation epoch, accounting for covariance information?

# Chapter 6

## *Research Goal 3(a)*: Evaluating the conjunction challenges of low-thrust GEO debris removal maneuvers

### 6.1 Overview of Research Goal

Currently, the most widely-implemented mitigation strategy for GEO satellites reaching end-of-life is to re-orbit to a graveyard disposal orbit at a perigee altitude safely above the GEO ring, "far enough away from GEO so as not to cause interference with space systems still in geostationary orbit."[21] In 1997, the Inter-Agency Space Debris Coordination Committee (IADC) proposed the following guideline to provide a stable passivation orbit that remains safely outside the protected GEO region, defined by a spherical shell segment within $\pm$200 km of the GEO altitude and $\pm 15^\circ$ latitude of the equatorial plane:[22,60]

$$\Delta h_p|_{\text{min}} \geq 235 + 1000 c_r (A_\odot/m) \quad \text{[km]} \tag{6.1}$$

where $c_r$ is the coefficient of reflectivity and $A_\odot/m$ is the area-to-mass ratio.[21] The 235 km minimum is the sum of the upper altitude for the protected GEO region (200 km) and the maximum descent of a re-orbited satellite due to geopotential and luni-solar perturbations (35 km).[60] For typical GEO satellites ($c_r \approx 1.5$ and $A_\odot/m \approx 0.04$ m$^2$/kg), the second term in Equation (6.1) is approximately 60 km, such that this IADC re-orbit guideline specifies a $\sim$300 km increase in perigee altitude, at minimum.[1] The IADC furthermore recommends

[1] The recommended mitigation re-orbit maneuver is executed in a multi-burn sequence with an approximate fuel cost equivalent to three months of station-keeping fuel for a typical GEO satellite,[21] corresponding to $\Delta v \approx 11$ m/s, that is, about 2.3% of the entire E-W/N-S station-keeping budget for a 10-year mission.[11]

the addition of an error margin to account for orbit determination uncertainties, maneuver execution errors, and spacecraft deterioration.[60] Although one might speculate that the IADC guidelines could increase the risk of derelict collisions in the IADC debris orbit that could accumulate above GEO under these guidelines, Reference 23 indicates that the variable amount of remaining propellant at end-of-life has driven the broad variety of disposal orbits achieved in practice, such that the creation of a unique "debris ring" is unlikely. Of the 160 GEO satellites that achieved end-of-life in the period 2001-2010, 80% successfully re-orbited to disposal orbits – of these satellites, 70% were transferred to orbits at least 200 km above GEO, and 50% achieved at least 300 km above, fully compliant with the IADC.[23]

Using historical re-orbit statistics compiled from the European Space Agency's *Classification of Geosynchronous Objects* reports,[33] Figure 6.1 illustrates compliance to the IADC GEO re-orbit guidelines since they were introduced to the operator community in 1997.[60] Figure 6.1(a) provides the annual number of GEO satellites that (1) reached the end of their operational lifespans, (2) attempted re-orbit to an IADC-compliant disposal orbit, and (3) successfully achieved the minimum perigee altitude increase specified in the IADC guidelines. The margin between the number of satellites that reached end-of-life and those that re-orbited into an IADC-compliant disposal orbit has decreased since 1997, indicative of an increasing international desire to preserve the long-term utilization of GEO. Figure 6.1(b) provides a breakdown by entity of the compliance data in Figure 6.1(a). During 1997-2013, approximately 50% of GEO satellites that reached end-of-life were repositioned into compliant disposal orbits before deactivation; nearly 30% attempted post-mission disposal, but were unsuccessful in reaching the minimum perigee altitude increase. The remaining 20% (53 GEO satellites) were abandoned without any re-orbit attempt during this time period, of which Russia contributed 33 satellites (62% of the assets abandoned during this 16-year period). As the resulting political cost to Russia for poor compliance with these guidelines has been negligible, these re-orbit data illustrate that it is less expensive in the near term to generate debris without repercussions from disregarding adopted mitigation practices.[61]

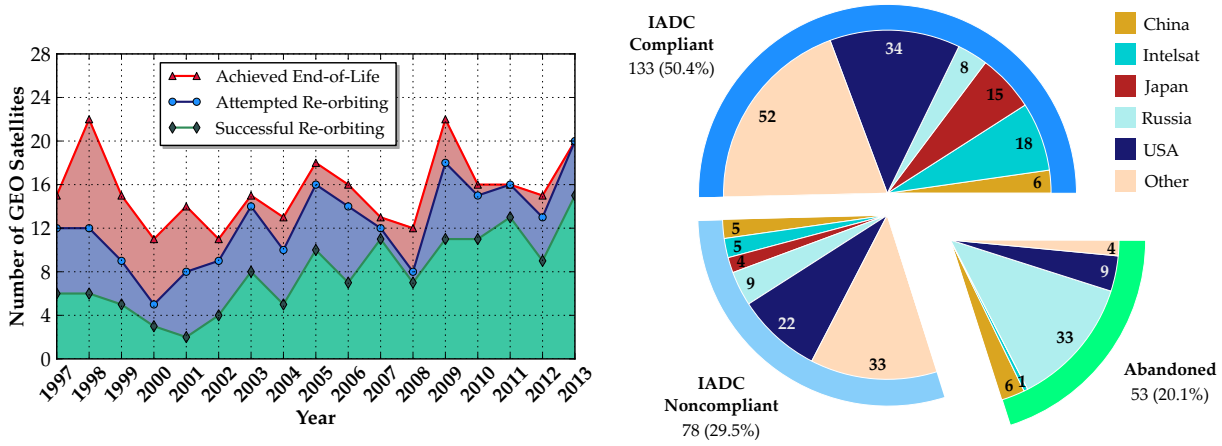


(a) Annual compliance to IADC re-orbit guidelines. (b) Guideline compliance by entity for 1997-2013.

Figure 6.1: Compliance to end-of-life GEO mitigation guidelines introduced by the IADC in 1997, illustrated as compliance rate by year and compliance rate by entity through 2013.

Even under an optimistic 80% compliance rate, however, Section 4.5 predicts that the mean number of near-miss events per day at 300 km in the vicinity of the two gravitational wells will double by the year 2063. Although recent re-orbiting statistics are promising in that they suggest increasing adherence to mitigation guidelines—and ultimately growing international desire to safeguard the GEO ring—mitigation alone is not enough to stabilize the growing debris congestion at GEO under current re-orbiting success rates. To stabilize projected debris growth at GEO under current mitigation levels, active debris remediation (ADR) measures must be synthesized and implemented to remove potentially threatening derelicts that (a) failed to achieve an IADC-compliant graveyard orbit at end-of-life, or (b) were simply abandoned by their operators at end-of-life with no attempt at a re-orbit. The necessity for cost-effective ADR activities at GEO is becoming more relevant, especially for larger derelicts (payloads, upper stages) that pose the greatest threat to operational assets.

A "chief space-tug" concept is often envisioned for performing the re-orbit maneuver once contact with the target debris object has been established. However, as rendezvous, proximity operations, and docking with an uncontrolled—and likely tumbling—derelict

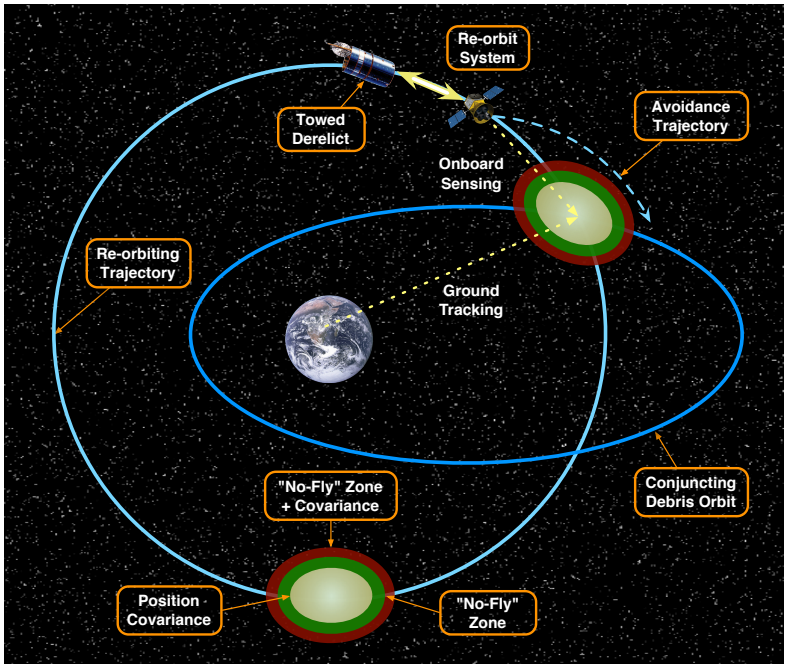


Figure 6.2: Challenges of low-thrust GEO debris re-orbit.

are challenging, several proposed methods have focused on contactless technologies such as an electrostatic tractor[62] or ion beam shepherd[63] for ADR at GEO. Each of these contactless ADR technologies rely on low-thrust engines for performing the required re-orbit maneuver. With lower maneuverability, however, collision avoidance for such low-thrust re-orbit systems is challenging. Potential conjunctions must be detected multiple revolutions in advance, to provide the tug's guidance system enough lead time to place the tug on a sufficient evasive trajectory, especially if this craft is designed to operate autonomously with minimal ground support. Figure 6.2 shows the challenges of developing a low-thrust guidance strategy for GEO debris re-orbiting applications. Of interest is investigating how many conjunction events with the current debris population at GEO could be experienced during a typical continuous thrust re-orbiting maneuver to an IADC-compliant graveyard orbit 300 km above the GEO ring.[7] Specifically, quantifying the *conjunction challenge* for a range of thrust levels—i.e., the global average of the number of conjunctions that could be expected for a re-orbit trajectory at each thrust level, regardless of the initial longitude or

inclination—is a useful tool for system design of an ADR demonstration mission at GEO.

Evaluating the global conjunction challenge for low-thrust GEO disposal maneuvers is beneficial not only for debris removal concepts, but for operational end-of-life mitigation activities, too. As lightweight, all-electric satellite busses are becoming more prominent in the satellite industry,[2] low-thrust electric propulsion is now being harnessed both for orbit raising and station-keeping of satellites. Previously, GEO satellites with chemical thrusters have used a two- to three-impulse Hohmann-like transfer to re-orbit to a disposal orbit at end-of-life,[11,64] but GEO satellites equipped with low-thrust electric engines must use continuous thrust orbit raising techniques to achieve the required increase in semi-major axis. Since continuous thrust re-orbiting performed under mN levels of thrust takes from weeks to months to achieve a 300 km increase in semi-major axis,[62] it is critical to quantify the number of conjunctions that such satellites might experience during this phase of de-commissioning. As it is undesirable to be responsible for a debris-generating event while engaged in an act of mitigation or remediation, characterizing the conjunction challenges of low-thrust re-orbit maneuvers is critical knowledge for both all-electric satellite operators and designers of contactless technologies using low-thrust engines for ADR at GEO.[3]

## 6.2 Analytic Results for Continuous Thrust Trajectories

In the framework of two-body dynamics, analytic expressions that describe the semi-major axis and longitude profiles for a continuous thrust re-orbit trajectory—as a function of thrust acceleration and elapsed time since the start of the re-orbit maneuver—are now derived. Following Reference 65, the time derivative of specific two-body orbit energy is

$$\epsilon = -\frac{\mu_\oplus}{2a} \quad \Longrightarrow \quad \dot{\epsilon} = \frac{\mu_\oplus}{2a^2}\dot{a} \tag{6.2}$$

[2] de Selding, P. B., "News from Satellite 2014: Boeing Electric Satellite Backlog Posed to Grow, includes Previously Undisclosed U.S. Gov't Order," *Space News*, 13 March 2014, Web.

[3] In this thesis, GEO satellites using continuous thrusting during end-of-life operations, and ADR space-tug concepts that use continuous thrust to re-orbit derelict objects to disposal orbits, are collectively termed *re-orbit systems* for generality.

where $\dot{a}$ denotes the time rate of change of the semi-major axis. From elementary physics, the rate of change of specific energy due to the thrust vector $\boldsymbol{\Gamma}$ is $\dot{\epsilon} = \boldsymbol{\Gamma} \cdot \boldsymbol{v}$, where $\boldsymbol{v}$ is the inertial velocity vector. Assuming that the thrust acceleration is directed along the instantaneous velocity vector direction (i.e., zero flight path angle), then $\dot{\epsilon} = \Gamma v$, such that

$$\frac{\mu_\oplus}{2a^2}\dot{a} = \Gamma v \quad \Longrightarrow \quad \dot{a} = \frac{2a^2\Gamma}{\mu_\oplus}v \approx \frac{2a^{3/2}\Gamma}{\sqrt{\mu_\oplus}} \tag{6.3}$$

where it is assumed that the osculating orbit remains near-circular during the continuous-thrust maneuver, such that the circular orbit velocity $v = \sqrt{\mu_\oplus/a}$ is applicable. Separating variables and assuming constant $\Gamma$, we have:

$$\int a^{-3/2}\mathrm{d}a = \frac{2\Gamma}{\sqrt{\mu_\oplus}}\int \mathrm{d}t \tag{6.4}$$

Performing the integration and enforcing the initial condition $a(0) = a_0$:

$$-\frac{1}{\sqrt{a}} = \frac{\Gamma}{\sqrt{\mu_\oplus}}t - \frac{1}{\sqrt{a_0}} \quad \Longrightarrow \quad a(t) = \frac{a_0\mu_\oplus}{(\sqrt{\mu_\oplus} - \Gamma\sqrt{a_0}t)^2} \tag{6.5}$$

The time $t_f$ required to transfer between circular orbits of radii $a_0$ and $a_f > a_0$ is therefore given by:[65]

$$t_f = \frac{\sqrt{\mu_\oplus}}{\Gamma}\left(\frac{1}{\sqrt{a_0}} - \frac{1}{\sqrt{a_f}}\right) = \frac{v_0 - v_f}{\Gamma} \tag{6.6}$$

As a result, $v_f = v_0 - \Gamma t_f$, that is, the re-orbit system slows down linearly in time as local circular orbit speed is maintained.[65] Figure 6.3 illustrates Equation (6.6) as a function of thrust acceleration for three super-synchronous semi-major axes. The hyperbolic form of Equation (6.6) indicates that as the thrust acceleration increases, the length of the re-orbit maneuver decreases rapidly. Furthermore, as the target semi-major axis $a_f$ increases, local orbit speed $v_f$ at $a_f$ decreases, such that the length of the re-orbit maneuver increases. As will be shown, the duration of the re-orbit maneuver is strongly correlated to the number of conjunction events a trajectory at a specified thrust acceleration experiences on average.

For a near-circular orbit, the rate of change of longitude $\dot{\lambda}$ is given by the mean motion difference

$$\dot{\lambda} = n - n_{\text{GEO}} = \sqrt{\frac{\mu_\oplus}{a^3}} - \sqrt{\frac{\mu_\oplus}{a_{\text{GEO}}^3}} \tag{6.7}$$

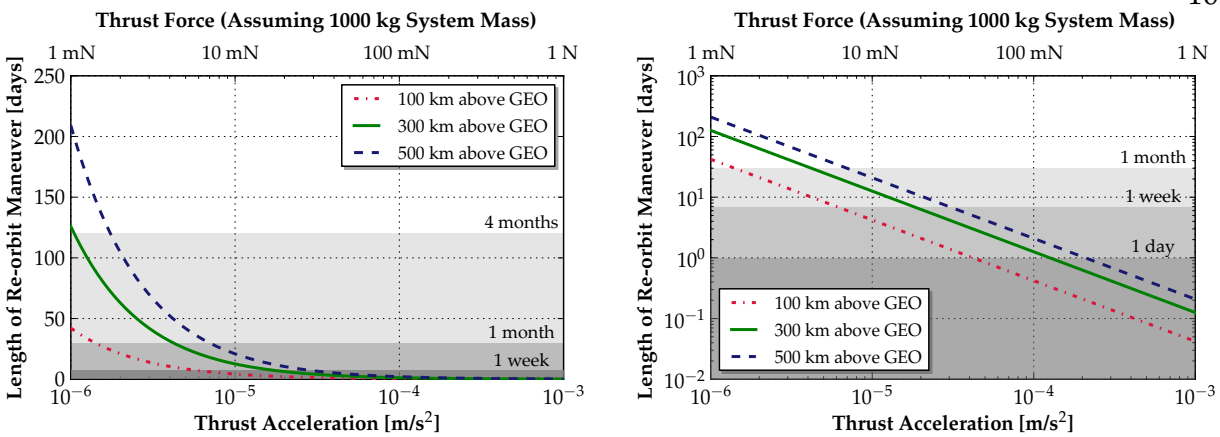


(a) Analytic re-orbit duration (linear $y$-axis). (b) Analytic re-orbit duration (logarithmic $y$-axis).

Figure 6.3: Duration of continuous-thrust re-orbiting maneuvers to three semi-major axes above GEO as a function of constant thrust acceleration and force, assuming 1000 kg mass.

Substituting Equation (6.5) for the semi-major axis $a(t)$, the longitude rate becomes

$$\dot{\lambda}(t) = \frac{(\sqrt{\mu_\oplus} - \Gamma\sqrt{a_0}t)^3}{a_0^{3/2}\mu_\oplus} - \sqrt{\frac{\mu_\oplus}{a_{\text{GEO}}^3}} \tag{6.8}$$

Integrating Equation (6.8) and enforcing the initial condition $\lambda(0) = \lambda_0$:

$$\lambda(t) = \frac{\mu_\oplus^2 - (\sqrt{\mu_\oplus} - \Gamma\sqrt{a_0}t)^4}{4\Gamma a_0^2\mu_\oplus} - \sqrt{\frac{\mu_\oplus}{a_{\text{GEO}}^3}}t + \lambda_0 \tag{6.9}$$

Given that the re-orbit system begins at longitude $\lambda_0$, Equation (6.9) provides an analytic prediction for the resulting longitude profile of the system as a function of elapsed time $t$ since maneuver start, initial semi-major axis $a_0$, and thrust acceleration $\Gamma$. Since the semi-major axis increases above that of GEO during the re-orbit, as described by Equation (6.5), the mean motion of the system slows with respect to the rotational rate of Earth, resulting in westward longitudinal drift. To evaluate the amount of longitude drift $\Delta\lambda \equiv \lambda(t_f) - \lambda_0$ that occurs during re-orbit as a function of thrust acceleration, the maneuver duration $t_f$ in Equation (6.6) is substituted into Equation (6.9), giving

$$\Delta\lambda = \frac{\mu}{4\Gamma a_0^2}\left[1 - \left(\frac{a_0}{a_f}\right)^2\right] - \sqrt{\frac{\mu_\oplus}{a_{\text{GEO}}^3}}\left(\frac{v_0 - v_f}{\Gamma}\right) \tag{6.10}$$

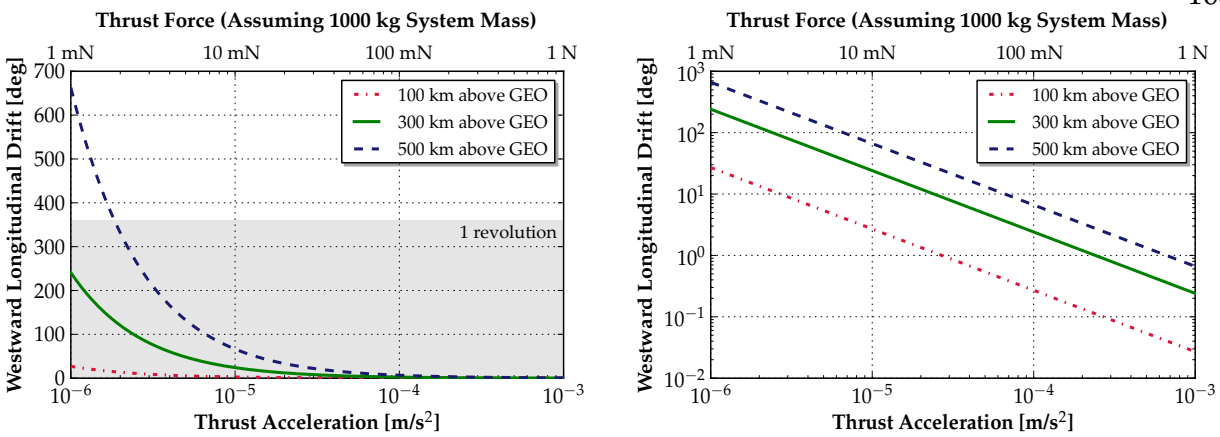


(a) Analytic longitude drift (linear $y$-axis). (b) Analytic longitude drift (logarithmic $y$-axis).

Figure 6.4: Accumulated longitudinal drift $\Delta\lambda$ for continuous-thrust re-orbit maneuvers to three semi-major axes above GEO, as a function of constant thrust acceleration and force.

Figure 6.4 illustrates Equation (6.10) as a function of thrust level for three super-synchronous semi-major axes. The hyperbolic form of Equation (6.10) indicates that as the thrust acceleration increases, the total longitudinal drift accumulated over the duration of the re-orbit decreases rapidly. Further, since larger $a_f$ require longer maneuver durations $t_f$ by Equation (6.6), total longitudinal drift increases with $a_f$ as a result. Figure 6.4 provides an interesting compliment to continuous-thrust trajectory representations in the inertial frame, which exhibit a "spiral-like" pattern in inertial space. For simulated maneuvers to 300 km above GEO, Figure 6.4 illustrates that the re-orbit system does not complete an entire revolution in the Earth-fixed frame over the range of thrust levels considered. This has implications for ground station coverage of these re-orbit maneuvers, and highlights that systems beginning in less-congested longitude slots could still pass through heavily-congested longitudinal regions (e.g., one or both of the gravitational wells) over the course of the transfer.

## 6.3 Evaluating Conjunctions for GEO Re-orbit Maneuvers

To begin developing insight into the conjunction challenges for continuous thrust re-orbit systems at GEO, this study considers the number of conjunction events that a re-orbit

system could encounter with the current GEO debris population during a typical re-orbit maneuver to 300 km above the GEO ring. Specifically, the research questions investigated in this GEO conjunctions study are as follows:

- How many conjunctions within various distances can be expected, on average, for a specified thrust acceleration, ranging from $10^{-6}$ to $10^{-3}$ m/s$^2$ (i.e., 1 mN to 1 N thrust force for a 1000 kg system), over the duration of a 300 km re-orbit maneuver?
- Is the number of conjunctions dependent on initial longitude and inclination, and if so, is this dependency sensitive to the thrust acceleration or the time at which the re-orbit maneuver begins?
- When are conjunctions most likely to occur during the re-orbit burn, regardless of initial longitude or inclination? Does the likelihood of a conjunction increase over a range of semi-major axes, and if so, which classes of debris objects are responsible for these conjunctions? Is conjunction likelihood also sensitive to longitude?
- What is the distribution of conjunction events in the Hill frame for a given thrust level? What are the relative speeds and combined risk factors associated with the conjunction events for a given thrust level?

The equations of motion for a re-orbit system are equivalent to those for the uncontrolled debris objects (described in Section 2.3.2), with the addition of a continuous thrust vector $\boldsymbol{a}_t$, which is oriented in the in-track (along-track) direction of the local orbit frame:

$$\ddot{\boldsymbol{r}} = -\frac{\mu_\oplus}{r^3}\boldsymbol{r} + \boldsymbol{a}_\oplus + \boldsymbol{a}_\mathfrak{D} + \boldsymbol{a}_\odot + \boldsymbol{a}_{\text{SRP}} + \boldsymbol{a}_t \tag{6.11}$$

The debris population is propagated from 01 March 2014 (00:00:00 Zulu) for five months in 5 minute time steps, and each continuous thrust re-orbit trajectory is propagated forward from the same epoch under Equation (6.11), until 300 km above GEO in semi-major axis is achieved. Conjunctions are then detected in post-processing by checking for debris objects

that come within a specified distance threshold of the re-orbit system at any time step over the duration of the maneuver. Logic is applied to ensure that multiple conjunctions from the same debris object detected over subsequent propagation steps are only counted once.

To quantify how threatening simulated conjunction events are for a re-orbit system, each conjunction event is assigned a level of combined risk based upon the relative state of the responsible debris object at the time of conjunction. Position and velocity risk functions are employed to individually weight (a) *how close* the object comes to the re-orbit system, and (b) *how fast* the object is traveling relative to the re-orbit system. Specifically, the position and velocity risk functions selected for this analysis are (equivalent to Section 2.3.3):

$$R_r(r) = \left(\frac{\tilde{r} - r}{\tilde{r}}\right)^2, \quad 0 \leq r \leq \tilde{r} \tag{6.12}$$

$$R_v(v) = 1 - e^{-3v/\bar{v}}, \quad v \geq 0 \tag{6.13}$$

where $\tilde{r}$ denotes the conjunction distance threshold, and $r$ and $v$ denote the magnitude of the relative position and velocity vectors at conjunction, respectively.[4] As in Section 2.3.3, the scaling velocity $\bar{v} \approx 0.2828$ km/s, derived from the NASA Standard Breakup Model as the relative speed threshold above which collisions are "catastrophic," assuming equivalent masses for the target and impactor.[46] After the relative position and velocity for the conjunction event are computed, the risk functions defined via Equations (6.12)-(6.13) are evaluated, such that the combined risk factor given by the product $R_r(r)R_v(v)$ is evaluated. This combined risk factor for the conjunction event is on the interval [0,1] and provides a metric for gauging how "threatening" the conjunction is for the re-orbit system. Note that both close proximity and sufficient relative speed must be present for a conjunction event to be considered high-risk under this metric – higher-speed events near the distance threshold and lower-speed events near the re-orbit system are both de-weighted (cf. Section 2.3.3). Note that this risk measure is not associated with the probability of collision metric used in

[4] Given that inertial frame positions and velocities for both the re-orbit system and the conjuncting debris object are known at the time of conjunction, the position $\boldsymbol{r}$ and velocity $\boldsymbol{v}$ for the debris object, relative to the re-orbit system, can be described in the local Hill frame using the relative motion algorithm in Reference 55.

conjunction assessment and should not be treated as equivalent with this statistical metric.

## 6.4 Results of GEO Re-orbit Conjunctions Study

### 6.4.1 Global Conjunction Challenge

To assess the global conjunction challenge for a given thrust level, a two-dimensional sweep over initial longitude on [0°,360°) and inclination on [0°,15°] is performed in 5° and 1° increments, respectively. The re-orbiting system is initialized using $a = a_{\text{GEO}}$, $e = 0.001$, $\omega = M_0 = 0°$, and right ascension of ascending node $\Omega$ selected to enforce the initial longitude at the start epoch of 01 March 2014 (00:00:00 Zulu). Figure 6.5 illustrates the mean number of conjunctions per trajectory as a function of thrust level and distance threshold, globally averaged over the 1152 trajectories propagated for each of the seven thrust accelerations surveyed, ranging from $10^{-6}$ to $10^{-3}$ m/s$^2$ (that is, 1 mN to 1 N of thrust for a 1000 kg system). For all distances considered, the mean number of conjunctions per trajectory rises hyperbolically as the thrust level decreases, a consequence of the result that re-orbit duration to 300 km above GEO increases hyperbolically as the thrust level decreases (see Figure 6.3). Therefore, the lower the thrust level considered for the re-orbiting system, the more "challenging" the maneuver becomes from the perspective of conjunction potential – the required burn time is lengthened, such that more conjunctions with the large-scale debris population are possible over the duration of the maneuver. Note that for the 500 mN and 1 N levels, no conjunctions beneath 25 km are experienced across all 1152 trajectories surveyed at these thrust levels, emphasizing that the mean number of conjunctions for a given thrust level and distance threshold becomes nearly zero as the thrust level increases.

In addition to quantifying the mean number of conjunctions per trajectory, it is also of interest to evaluate the standard deviation for the conjunction distributions generated at each thrust level and distance threshold. Figure 6.5(a) illustrates $1\sigma$ swaths for each thrust level and threshold, highlighting that the $1\sigma$ spread of these distributions decreases as the

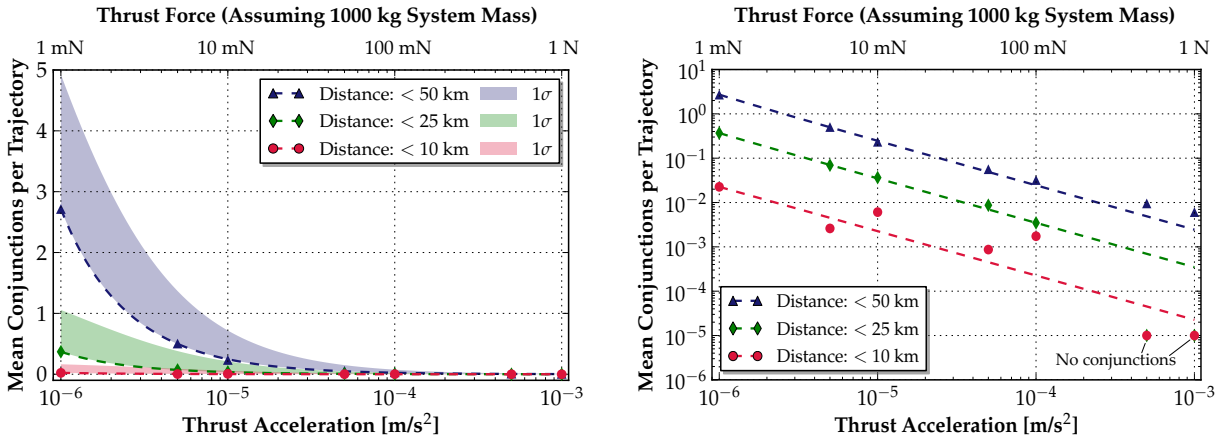


(a) Mean number of conjunctions with $1\sigma$ swaths.

(b) Mean number of conjunctions (log $y$-axis).

Figure 6.5: Mean number of conjunction events per trajectory as a function of thrust level and distance threshold shown with hyperbolic best-fit lines on linear and logarithmic axes.

thrust increases at each distance threshold. Thus, the number of conjunctions anticipated for a given trajectory at the 1 mN level, for example, becomes more uncertain in that this trajectory could experience fewer—or conversely, many more—conjunctions at a distance threshold of 50 km than the global average of approximately 2.7 conjunctions per trajectory at this distance. Inhomogeneities in conjunction potential are explored in the next sections.

### 6.4.2 Dependence on Initial Longitude and Inclination

Next, it is of interest to evaluate whether the number of conjunctions experienced for a particular trajectory at a particular thrust acceleration is sensitive to the initial longitude and inclination of the re-orbit system at the beginning of the maneuver. Figure 6.6 shows the number of conjunctions at a distance threshold of 50 km experienced for each of the 1152 trajectories surveyed under 1 mN, 5 mN, and 10 mN thrust accelerations. Qualitative trends in the number of conjunction events experienced at each thrust acceleration are not observed, indicating no deterministic dependence of the number of anticipated conjunctions on the initial longitude and inclination of the re-orbit system. As the thrust acceleration increases, "holes" in the initial condition space begin appearing in greater frequency,

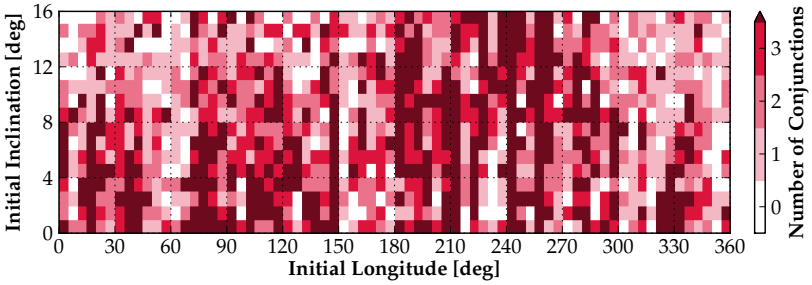


(a) Number of conjunctions at 50 km (thrust level: $1.0 \times 10^{-6}$ m/s$^2$).

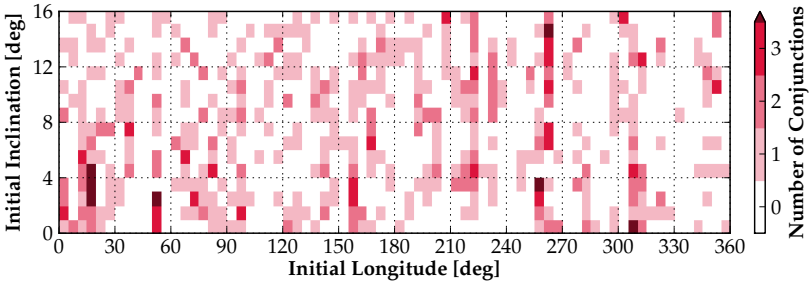


(b) Number of conjunctions at 50 km (thrust level: $5.0 \times 10^{-6}$ m/s$^2$).

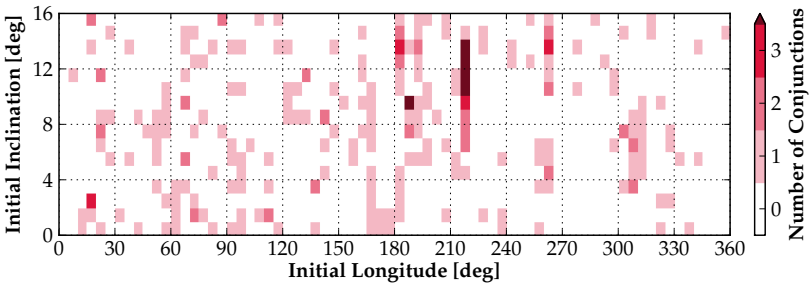


(c) Number of conjunctions at 50 km (thrust level: $1.0 \times 10^{-5}$ m/s$^2$).

Figure 6.6: Number of conjunction events experienced during a continuous-thrust re-orbit to 300 km above the GEO ring, illustrated as a function of initial longitude and inclination.

illustrating the result of Figure 6.5 that the number of conjunctions experienced globally for a given thrust acceleration decreases hyperbolically as this thrust increases. Although the global average in Figure 6.5 indicates that the number of conjunctions is sparse at all distances considered for thrust levels larger than ∼5 mN, Figure 6.6(c) illustrates that particular regions of the initial condition space could still be subject to upwards of three conjunction events at 50 km over the course of the re-orbit. Thus, it is critical to emphasize that Figure 6.5 provides a first-order—not exhaustive—design tool for forecasting the number

of conjunction events that could be experienced during re-orbit at a particular thrust level.

### 6.4.3 Conjunctions in SMA and Longitude Space

In addition to studying the dependence of the number of conjunctions on the initial longitude and inclination of the re-orbit system, it is important to quantify *where* conjunction events are most likely to occur over the duration of the maneuver. Instead of studying the frequency of conjunctions as a function of elapsed time since maneuver start, it is more consistent to consider the distribution of conjunction events in semi-major axis (SMA) and longitude space. Using the total number of conjunctions detected at a distance threshold of 50 km accumulated across all thrust levels considered, Figure 6.7 shows the conjunction probability for various regions in this SMA/longitude phase space.[5] The contributions of the librating debris population are evident around the two gravitational wells at 75°E and 105°W, with GEO-relative semi-major axes from 0-50 km above the GEO ring. As the SMA increases relative to GEO, neighborhoods with higher conjunction probabilities are experienced, indicative of contributions by the westward drifting population at higher altitudes.

The conjunction probability map illustrated in Figure 6.7 is an important tool in that it can be combined *a priori* with the analytic SMA/longitude predictions in Equations (6.5) and (6.9) to predict when a re-orbit system will be entering a region in the phase space with a higher conjunction probability relative to the surrounding regions in this phase space. Figure 6.7 further shows three re-orbit trajectories beginning at a longitude of 105°W, with 1 mN, 5 mN, and 10 mN of thrust acceleration, respectively. Given that the thrust acceleration and initial location in this phase space are known, the resulting re-orbit trajectory can be predicted with Equations (6.5) and (6.9), such that increased ground tracking can be requested prior to the re-orbit system entering a region with a higher conjunction likelihood. In the case of an autonomous system for ADR at GEO, onboard environmental sensing can

[5] "Longitude" refers here to the longitude at which each conjunction event occurs during re-orbit, not to the initial longitude of the re-orbit system, which is illustrated in Figure 6.6.

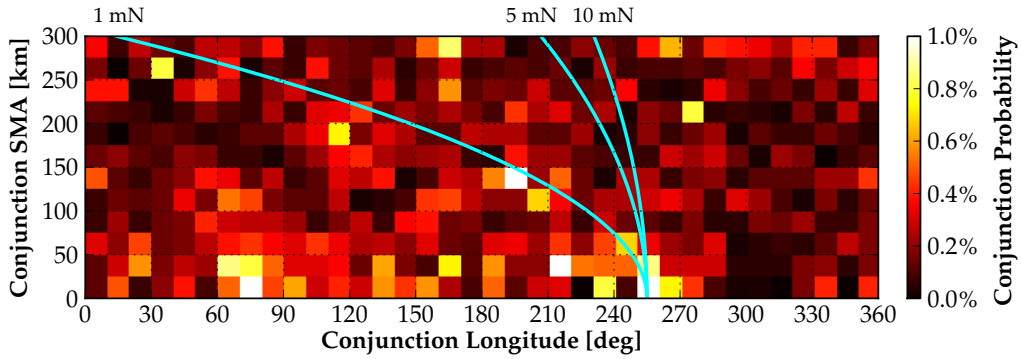


Figure 6.7: Density map illustrating regions in SMA/longitude space that experience high frequencies of conjunction events at 50 km, shown with three re-orbit trajectories at various thrust levels from an initial longitude of 105°W, as predicted by Equations (6.5) and (6.9).

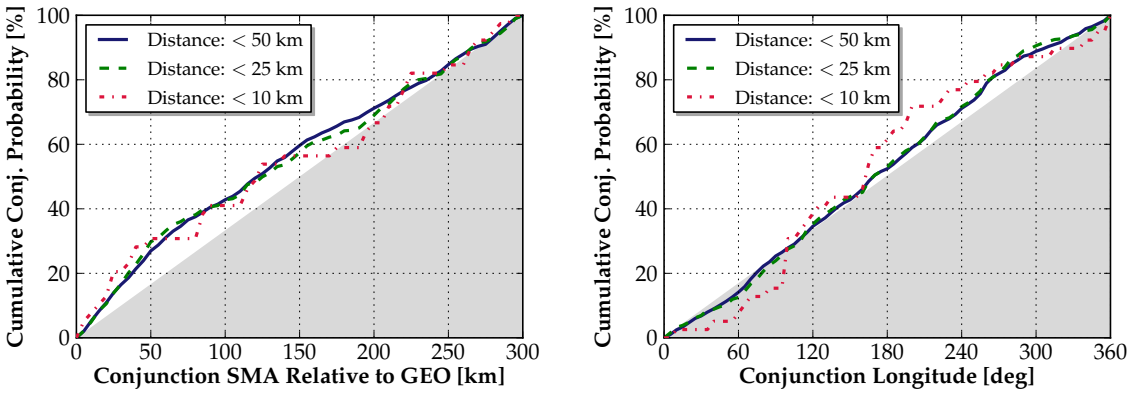


(a) Cumulative probability by semi-major axis.

(b) Cumulative probability by longitude.

Figure 6.8: Cumulative probability of conjunction event as function of semi-major axis and longitude during re-orbit burn, provided with uniform cumulative distribution function.

be applied or augmented when the re-orbit system enters higher conjunction risk regions.

If the conjunction probabilities illustrated in Figure 6.7 are binned by semi-major axis or longitude of conjunction only, the cumulative conjunction probability distributions for these two phase space variables—shown respectively in Figure 6.8—can be constructed. In particular, Figure 6.8(a) highlights that the cumulative probability of conjunction achieves 50% at approximately 120 km in SMA above the GEO ring across all thrust levels and distance thresholds considered. Therefore, the distribution of conjunctions in semi-major axis

is not uniform; rather, it exhibits slight bias towards the beginning of the maneuver, a consequence of the higher densities of librating objects in closer proximity to the GEO altitude. If equipped with a variable-thrust propulsion system, the re-orbiting system could reduce (or potentially eliminate) the number of anticipated conjunctions by increasing the thrust acceleration during the initial stages of the re-orbit, such that the system achieves a 120 km increase in SMA as rapidly as possible. After, the thrust acceleration could be decreased to conserve propellant until the desired re-orbit is accomplished. Interestingly, the cumulative probability by longitude in Figure 6.8(b) does not show strong contributions from the two gravitational wells, since these longitudes are only significant for conjunction probabilities at lower GEO-relative altitudes in closer proximity to the GEO ring (cf. Figure 6.7).

### 6.4.4 Relative Velocity and Risk Considerations

In addition to the average number of conjunctions experienced at a given thrust level, the dependence of this number of conjunctions on the initial conditions of the re-orbiting system, and where these conjunctions occur in SMA and longitude space, it is important to consider the relative velocities and combined risk factors for these conjunction events. For the 1 mN thrust level, Figure 6.9 illustrates three portraits of the conjunctions observed at a distance threshold of 50 km across the 1152 trajectories surveyed at this thrust level – the number of conjunction events in Figure 6.9(a), the maximum relative velocities for the conjunctions detected for each trajectory in Figure 6.9(b), and the maximum combined risk of the conjunctions detected for each trajectory in Figure 6.9(c). Figure 6.9 highlights that although a particular re-orbit trajectory could experience multiple conjunction events beneath 50 km over the duration of the re-orbit burn, the worst-case relative velocity of these conjunctions—or the worst-case combined risk thereof—could be benign, indicating that evasive action by the re-orbit system may not be necessary. Conversely, Figure 6.9 shows cases in which although only 1-2 conjunctions are experienced during the maneuver, these conjunctions carry a worst-case risk that may be significant enough to warrant evasive ac-

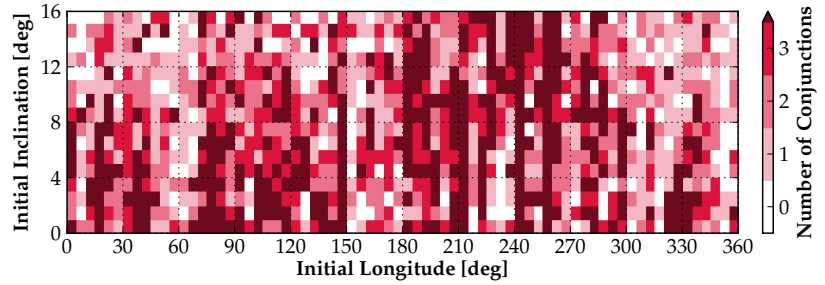


(a) Number of conjunctions at 50 km (thrust level: $1.0 \times 10^{-6}$ m/s$^2$).

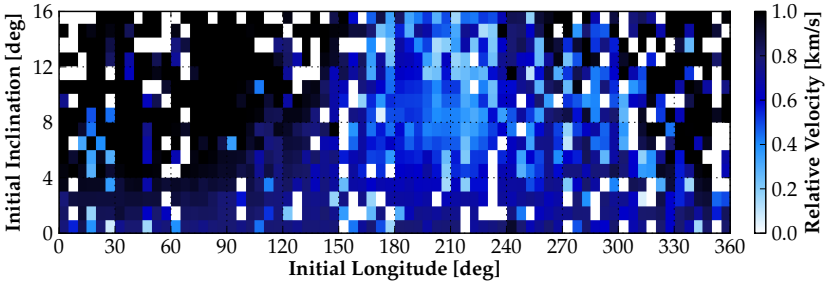


(b) Worst-case conjunction velocities (thrust level: $1.0 \times 10^{-6}$ m/s$^2$).

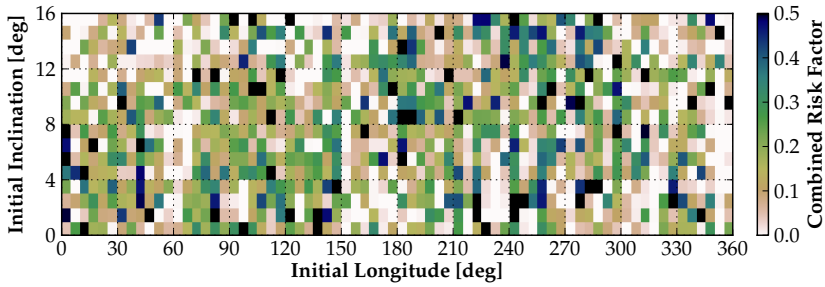


(c) Worst-case conjunction risk factor (thrust level: $1.0 \times 10^{-6}$ m/s$^2$).

Figure 6.9: Number of conjunctions at 50 km shown with worst-case relative velocities and combined risk factor for these trajectories, as a function of initial longitude and inclination.

tion (recall that conjunctions are threatening via the combination of proximity and speed).

To complement the global conjunction challenges illustrated in Figure 6.5, Figure 6.10 provides the average number of conjunctions per trajectory at various thrust levels and risk factor thresholds, globally averaged over the 1152 trajectories propagated for each thrust acceleration. For each risk threshold, the mean number of conjunctions per trajectory rises hyperbolically as the thrust level decreases. As the risk threshold increases, however, the mean number of conjunctions per trajectory for a given thrust level decreases in a manner

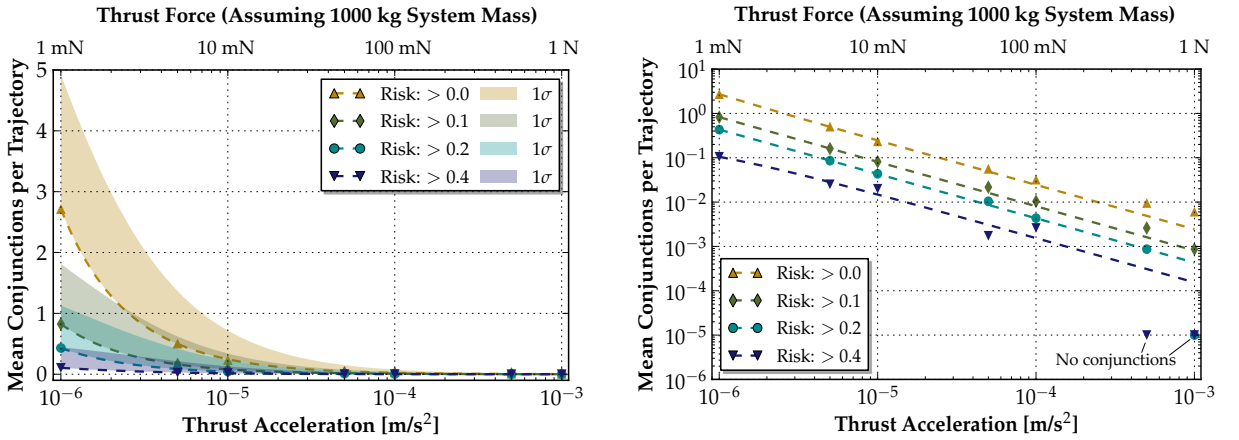


(a) Mean number of conjunctions with $1\sigma$ swaths.

(b) Mean number of conjunctions (log $y$-axis).

Figure 6.10: Mean number of conjunctions per trajectory at 50 km as a function of thrust level and risk level, provided with hyperbolic best-fit lines on linear and logarithmic axes.

that is analogous to decreasing the conjunction distance threshold (cf. Figure 6.5). Thus, at the 1 mN level, though the global conjunction challenge is approximately 2.7 conjunctions per trajectory on average at a distance threshold of 50 km, less than 0.5 conjunctions per trajectory on average are contributed by conjunctions with combined risk greater than 0.2. This global average is similar to that for a conjunction distance threshold of 25 km for the 1 mN thrust level in Figure 6.5.

To highlight the $1\sigma$ spread of the conjunction distributions generated for each thrust acceleration and risk threshold, Figure 6.10(a) illustrates $1\sigma$ swaths in addition to the mean number of conjunctions per trajectory determined for each thrust level and risk threshold. Analogous to Figure 6.5(a), the standard deviation decreases as the thrust level increases at a given risk threshold, and furthermore decreases as the risk threshold increases at a given thrust level. Thus, the average number of conjunctions with a combined risk factor above a given risk threshold—and the spread of the distribution that this mean conjunction metric describes—decreases significantly as the thrust level increases beyond ~10 mN. Re-orbit maneuvers beneath this thrust level become more challenging in that larger uncertainties make the number of conjunctions for any set of initial conditions more difficult to predict.

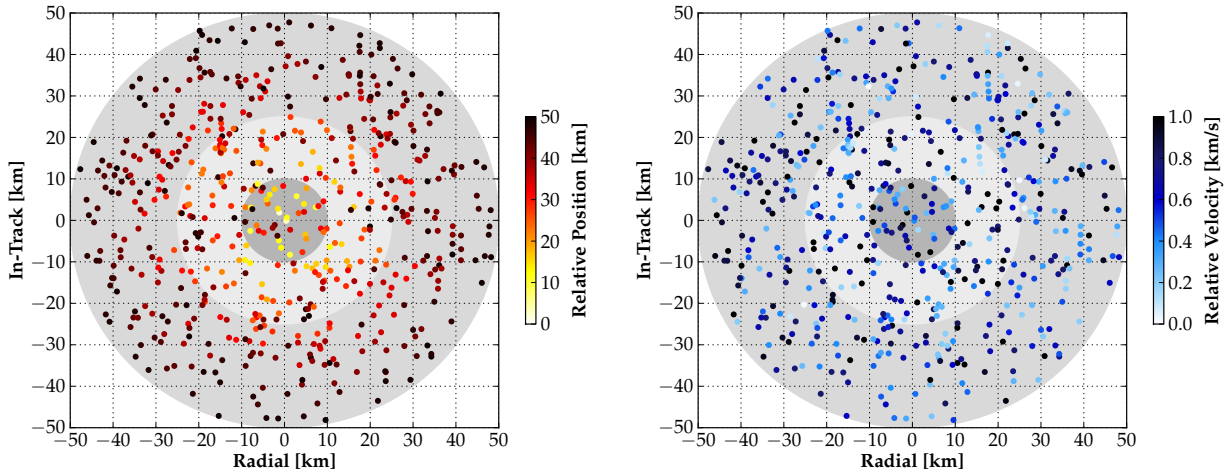


(a) Relative position distribution for conjunctions.

(b) Relative velocity distribution for conjunctions.

Figure 6.11: Distribution of conjunction events at 50 km in the local Hill frame, colored by relative position and relative velocity magnitude (thrust acceleration of $5.0 \times 10^{-6}$ m/s$^2$).

### 6.4.5 Distribution of Conjunctions in Hill Frame

For each of the conjunction events detected across all thrust accelerations considered in this study, it is beneficial to consider the distribution of these conjunctions in the Hill frame, which is centered on the re-orbit system and has axes directed in the orbit radial, in-track, and cross-track directions.[55] For all conjunctions at a distance threshold of 50 km detected across all 1152 trajectories at a thrust acceleration of 5 mN, Figure 6.11 illustrates the conjunction distribution in the local radial/in-track plane by relative proximity in Figure 6.11(a) and relative velocity in Figure 6.11(b). As Figure 6.11 highlights, trends in these relative position and velocity distributions are not observed, that is, the events detected are uniformly distributed (qualitatively) in the radial/in-track and radial/cross-track planes. Furthermore, these conjunctions occur at a broad range of relative speeds that are uncorrelated with the location of these conjunctions in the Hill frame. No correlations in the Hill frame distributions with thrust acceleration, initial longitude or inclination, or conjuncting debris object class are observed.

Figure 6.11 has important implications for guidance strategies for continuous thrust

re-orbit systems that are equipped to mitigate conjunction risk by adjusting the thrust profile, such that a sufficiently evasive trajectory relative to a conjuncting derelict is achieved. Since no correlations are qualitatively observed in the Hill frame position and velocity distributions, guidance strategies for debris avoidance must be flexible and robust, designed to handle any given relative position and velocity in the Hill frame. Note that the conjunctions shown in Figure 6.11 are the positions of conjuncting debris when these objects first cross the 50 km distance threshold, which is not necessarily the time of closest approach to the re-orbit system for each of these derelicts. Positions at the times of "first approach" are used to simulate the environmental sensing and detection performed by an autonomous re-orbit system, activities that would determine whether evasive action is even necessary.

### 6.4.6 Effect of Delaying Start Time of Maneuver

All of the re-orbiting trajectories considered thus far in this study are initialized at the start epoch 01 March 2014 (00:00:00 Zulu), but "holes" present in the initial condition space in Figure 6.6 for each thrust level suggest that the number of conjunction events for a given trajectory can be reduced, or even eliminated, if the start time of the maneuver is delayed. To evaluate the effect of delaying the start time for the 1152 trajectories propagated at each thrust level, Figure 6.12 provides the number of conjunction events at a distance threshold of 50 km, for the 2 mN thrust level, for start times in 6-hour increments over 01 March 2014. Studying Figure 6.12, it is evident that the number of conjunction events for the majority of trajectories can indeed be minimized or eliminated at particular times of day, which are dependent on the initial longitude—and therefore local time—of the re-orbit system.

Relative to an Earth-fixed observer, the collective motion of the debris field at GEO is qualitatively similar to a transverse wave with a period of one sidereal day, resulting from a clustering in right ascension of the ascending node driven by luni-solar perturbations.[6] Section 2.4.3 confirms that equatorial crossing windows of the GEO debris population are

[6] For an in-depth review of "pinch point" evolution resulting from luni-solar perturbations, see Chapter 3.

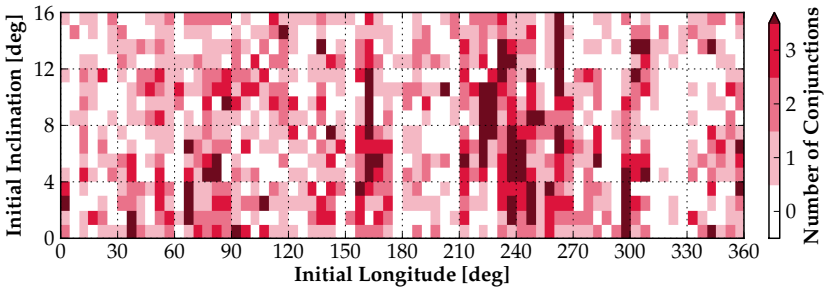


(a) Number of conjunctions at 50 km (re-orbit starts at 00:00:00 Zulu).

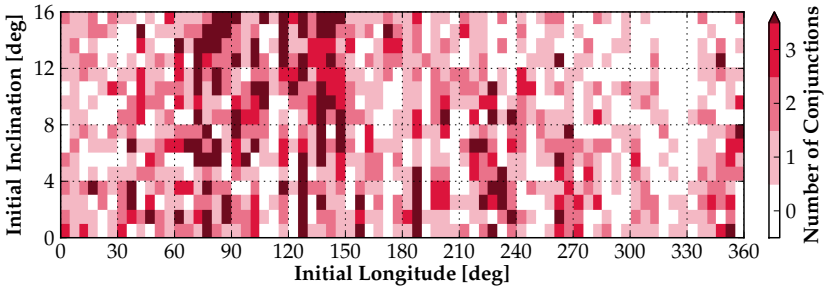


(b) Number of conjunctions at 50 km (re-orbit starts at 06:00:00 Zulu).

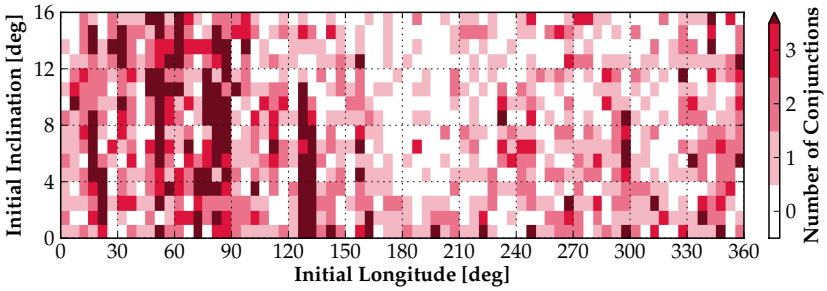


(c) Number of conjunctions at 50 km (re-orbit starts at 12:00:00 Zulu).

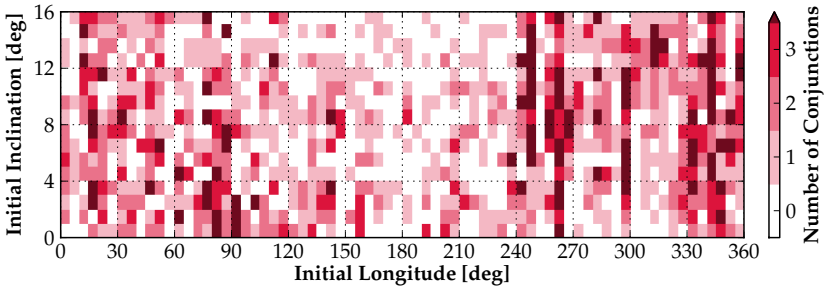


(d) Number of conjunctions at 50 km (re-orbit starts at 18:00:00 Zulu).

Figure 6.12: Effect of delaying start time for re-orbit maneuver on the number of conjunction events experienced across all trajectories surveyed at a thrust level of $2.0 \times 10^{-6}$ m/s$^2$.

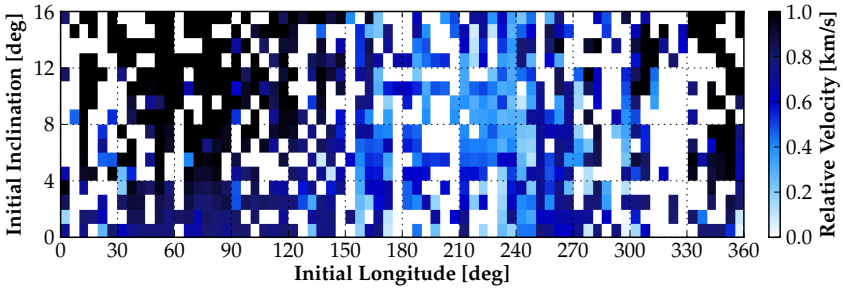


(a) Worst-case 50 km conjunction speeds (re-orbit starts at 00:00:00 Zulu).

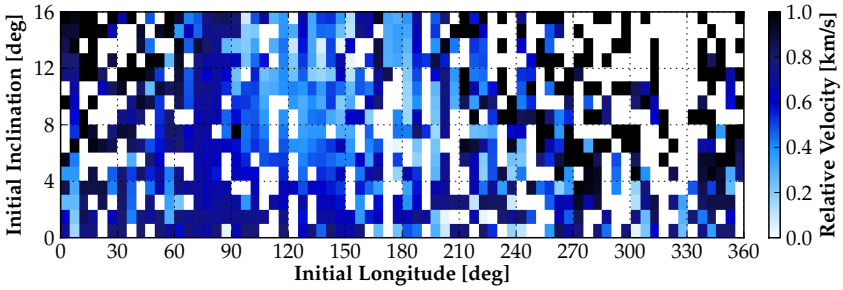


(b) Worst-case 50 km conjunction speeds (re-orbit starts at 06:00:00 Zulu).

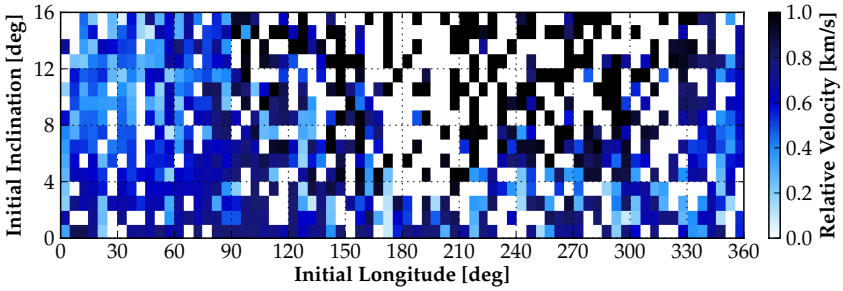


(c) Worst-case 50 km conjunction speeds (re-orbit starts at 12:00:00 Zulu).

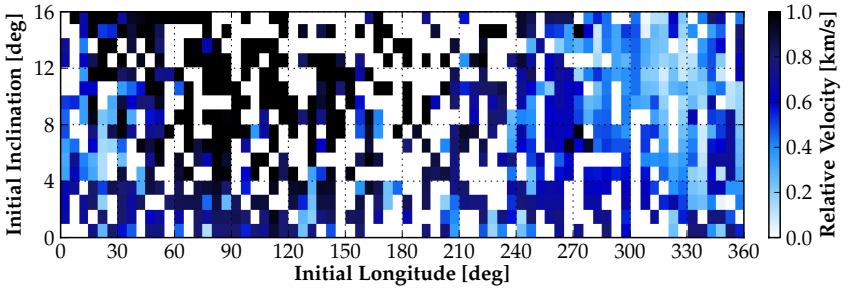


(d) Worst-case 50 km conjunction speeds (re-orbit starts at 18:00:00 Zulu).

Figure 6.13: Effect of delaying start time for re-orbit maneuver on the worst-case conjunction speeds experienced across all trajectories surveyed at a thrust level of $2.0 \times 10^{-6}$ m/s$^2$.

synchronized such that collision hazard to any longitude slot around GEO is episodic and predictable, dependent on time of year in addition to time of day. Therefore, delaying the start time for the re-orbit maneuver is analogous to shifting the latitudinal positions of the synchronized debris population located at the initial longitude of the re-orbiting system. Recalling that the re-orbit trajectories surveyed in this study are initialized at the ascending node in the equatorial plane, this suggests that trajectories beginning "in-sync" with local debris motion will, on average, experience more conjunctions than those beginning asynchronous to this transverse wave of debris, albeit with lower relative conjunction velocities.

Figure 6.13 shows the maximum relative velocities for the conjunction events at a distance threshold of 50 km illustrated in Figure 6.12. A prominent "wave-like" phenomenon that shifts westward nearly linearly across the longitude space as the start time is delayed over the course of one day is exhibited in Figure 6.13—a physical manifestation of the GEO debris synchronization effect on the conjunction challenges investigated in this thesis. As anticipated, the wave-like regions of minimum relative speed in Figure 6.13 correspond to those longitudes at which the local debris population is ascending through the equatorial plane from south to north during that time of day.[1] Since all propagated trajectories begin at the ascending node in the equatorial plane, these longitudes of reduced relative speed are those at which the re-orbiting system begins either partially or fully in-phase with local debris motion at the beginning of the maneuver. Conversely, the darker regions of higher relative velocities in Figure 6.13 are those at which the re-orbit system begins out-of-phase with the local debris population – the re-orbit system rises in latitude from the ascending node as the local debris population descends in latitude from north to south through the equatorial plane, leading to larger out-of-plane relative velocities at conjunction.

To emphasize the importance of the start time of the re-orbit maneuver in reducing or eliminating the number of conjunction events for a given initial longitude and inclination, Figure 6.14 provides the number of conjunctions at a distance threshold of 50 km for two trajectories—$(\lambda_0, i_0) = (75^\circ, 0^\circ)$ in Figure 6.14(a) and $(\lambda_0, i_0) = (75^\circ, 15^\circ)$ in Figure 6.14(b)—as

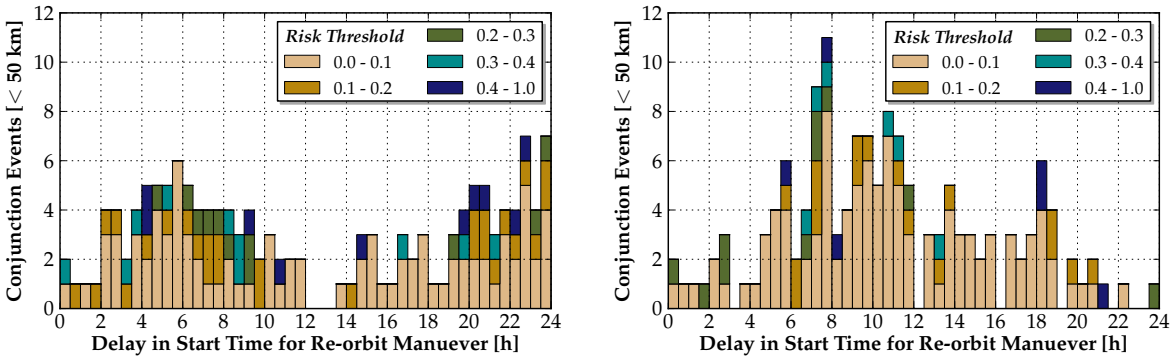


(a) Conjunctions at 50 km ($\lambda_0 = 75°, i_0 = 0°$). (b) Conjunctions at 50 km ($\lambda_0 = 75°, i_0 = 15°$).

Figure 6.14: Number of conjunctions as a function of maneuver delay (thrust acceleration of $2.0 \times 10^{-6}$ m/s$^2$) for two trajectories beginning at 75°E longitude and 0°/15° inclination.

a function of maneuver delay in half-hour increments. The number of conjunction events at each delay time is further subdivided by combined risk level, to highlight that not only is the number of conjunction events subject to change under a delayed start time, but the risk factors for these anticipated conjunctions, as well. For both cases in Figure 6.14, there exist optimal delay windows at which the number of conjunction events at a distance threshold of 50 km experienced over the entirety of the re-orbit maneuver are eliminated. Thus, the timing for the re-orbit maneuver is critical, and should be selected such that asynchronization with local debris motion at the beginning of the maneuver is leveraged to reduce—or even eliminate—the number of conjunction events experienced at a particular thrust level.

## 6.5 Conclusions from Research Goal

The conjunction challenges of using low-thrust propulsion for continuous thrust re-orbit of GEO objects to super-synchronous disposal orbits are investigated in this chapter. Lower maneuverability of re-orbit systems equipped with lower-thrust engines increases the challenges of collision avoidance, such that investigating the number of potential conjunction events experienced with the current debris population at GEO during a typical re-

orbit to 300 km above GEO is an imperative task. In particular, a two-dimensional sweep over initial longitude and initial inclination is performed, in which surveyed re-orbit trajectories are propagated from the GEO ring under various thrust levels until 300 km increase in semi-major axis is achieved. Then, conjunctions with large-scale GEO derelicts from the publicly-available TLE population are detected at various conjunction distance thresholds in post-processing, as described in the methodology outlined in Section 6.3.

Results indicate that on average, the number of conjunction events experienced for a given thrust level and distance threshold rises hyperbolically as the thrust level decreases, in correlation with the maneuver duration for a given thrust level. Sensitivity to the initial longitude and inclination of the re-orbit system at a particular start time, thrust level, and distance threshold are not observed. Examination of the conjunction events in semi-major axis and longitude space, however, highlights locations of this phase space in which conjunctions are more likely, e.g., around the gravitational wells within 50 km of the GEO ring in semi-major axis. Advantageously, timing the re-orbit maneuver appropriately—that is, such that the re-orbit system is asynchronous at the start of the transfer with the wave-like behavior of the local derelict motion—serves to reduce, or possibly eliminate, the number of conjunction events anticipated for a given trajectory at a given thrust level. No conjunctions beneath the distance threshold of 25 km are detected across all surveyed trajectories at the $5 \times 10^{-4}$ m/s$^2$ and $10^{-3}$ m/s$^2$ levels, indicating that timing may not be necessary in these cases. However, inasmuch as the debris population at GEO continues to increase in the absence of perfect, global adherence to mitigation guidelines—and since debris objects smaller than approximately 0.8-1 m are not included in this study—it is critical that re-orbit systems be equipped with a robust guidance system to adjust the thrust profile in the event that timely evasion of conjuncting debris is warranted.

## 6.6 Continuing Research Questions

For continuing research in this area, the following research questions are of interest:

(1) How many conjunction events for a given thrust level could the re-orbiting system experience in a realistic scenario, using chief and deputy covariance information? How many of these conjunctions might warrant evasive action to mitigate risk?

(2) In the case of an autonomous re-orbit system using environmental sensing in tandem with a guidance strategy for collision avoidance, what is a realistic distance at which conjuncting debris objects could be detected using state-of-the-art sensors?

(3) Could a thrust profile be implemented such that the re-orbit system remains asynchronized with the transverse debris wave throughout the entirety of the transfer?

# Chapter 7

## *Research Goal 3(b)*: Developing a guidance strategy for low-thrust debris avoidance during GEO re-orbit

### 7.1 Overview of Research Goal

In Chapter 6, the conjunction challenges for a GEO re-orbit system using low-thrust propulsion to perform orbit raising at end-of-life, in compliance with the IADC mitigation guidelines, are investigated by quantifying the number of conjunction events possible with the current TLE population during a typical re-orbit to 300 km above GEO. In this study, it is shown that although the average number of conjunctions per trajectory rises hyperbolically as the thrust acceleration decreases, the global conjunction challenge can be reduced by (a) increasing the thrust acceleration, and/or (b) timing the start of the maneuver such that the re-orbit system begins out-of-sync with the north-south, latitudinal motion of the local debris population. Depending upon mission constraints, satellite bus design, and the particular low-thrust propulsion used, option (a) may not be possible. Option (b) guarantees that the potential conjunction events for a given re-orbit trajectory will be reduced, but not necessarily eliminated. Therefore, it is of critical importance that such re-orbit systems be equipped with a GNC subsystem specifically for steering the vehicle onto an avoidance trajectory in the event a predicted conjunction warrants timely, evasive action. In this way, any remaining collision risk not mitigated under options (a) or (b) can be further reduced.

Although such a GNC subsystem is beneficial for operational GEO satellites engaged in mitigation activities at end-of-life, the application to autonomous, "space-tug" concepts

for environment remediation is emphasized in this chapter. Conceptualized in Figure 6.2, an autonomous re-orbit system for ADR at GEO would approach a high-risk target derelict, dock with it via either physical or contactless means, perform a continuous-thrust burn to increase the perigee altitude per the IADC guidelines, and lastly return to the GEO altitude to repeat with other debris objects until fuel has been depleted. With lower maneuverability, however, collision avoidance for such a low-thrust re-orbit system during orbit raising is a challenging task. Conjunctions must be detected with enough lead time to sufficiently alter the trajectory of the re-orbit system to mitigate collision risk by maintaining a desired miss distance, given covariance information and a specified "no-fly" (or "keep-out") zone surrounding the derelict. Intuitively, re-orbit systems with higher thrust levels (more maneuverability) can detect a conjuncting object later than systems with lower thrust levels (less maneuverability), and still miss this object by the same distance at the collision epoch. Thus, in addition to a guidance strategy for online avoidance of conjuncting debris, the re-orbit system must have the capability to sense the surrounding environment, and forecast potential conjunction events using relative state estimation and two-body orbit prediction.

Concepts for autonomous "sense and avoid" are widespread within the robotics and unmanned aerial vehicle (UAV) communities, and have recently been applied to the challenges of spaceflight, in particular, satellite cluster flight and rendezvous and docking. The artificial potential function concept for autonomous guidance was originally developed for terrestrial robotics applications,[66,67] and was later applied to the spacecraft formation flying problem for optimal reconfiguration,[68] distributed motion planning,[69] pattern transition,[70] and autonomous operations.[71] In this method, an artificial potential field (that is, non-physical and for purposes of control only) is superimposed around a neighboring object, and this potential field is activated to either attract or repel the controlled vehicle to or from this object.[67] Alternatively, the problem of continuous-thrust, on-orbit rendezvous can be treated by minimizing a path-dependent cost function—subject to path constraints enforcing collision avoidance among multiple vehicles—using nonlinear optimization[72,73]

or mixed-integer linear programming.[74] All of these intensive path-planning strategies, however, are not well-suited for autonomous GEO re-orbit systems, which demand simple-yet-robust control laws that are effective for on-orbit collision avoidance, while minimizing (1) human-in-the-loop interactions and (2) computational load required for the avoidance.

The guidance strategy for debris avoidance developed and simulated in this chapter is analogous to the conflict resolution maneuver proposed in Reference 75 for approaching aircraft in a congested control volume. It is shown that an aircraft entering the volume can always execute a lateral displacement maneuver—via a single heading change decision—that results in a conflict-free (collision-free) trajectory, as long as the width of the maneuver corridor is sufficiently large.[75] The guidance strategy for collision avoidance presented in this chapter uses a comparable heading change, i.e., the angle of the thrust vector, to result in a conflict-free trajectory inasmuch as the lead time with which the conjuncting object has been detected is sufficiently large for the particular maneuverability of the re-orbit system.

## 7.2 Development of Guidance Strategy for Debris Avoidance

### 7.2.1 Nonlinear Relative Equations of Motion with In-Plane Chief Thrusting

Prior to formulating the guidance strategy for debris avoidance, equations of motion that describe the trajectory of a deputy debris object relative to the chief re-orbit system—which is thrusting in the plane of the local orbit frame—are now derived. Using Cartesian coordinates in the rotating Hill frame centered on the re-orbit system, the inertial position vector of the deputy object is written as

$$\boldsymbol{r}_d = \boldsymbol{r}_c + \boldsymbol{\rho} = (r_c + x)\hat{\boldsymbol{o}}_r + y\hat{\boldsymbol{o}}_\theta + z\hat{\boldsymbol{o}}_h \tag{7.1}$$

where $r_c$ is the orbital radius of the chief, and $(x, y, z)$ are the Cartesian coordinates of the deputy object along the radial ($\hat{\boldsymbol{o}}_r$), in-track ($\hat{\boldsymbol{o}}_\theta$), and cross-track ($\hat{\boldsymbol{o}}_h$) axes of the Hill frame. The angular velocity vector of the Hill frame $\mathcal{O}$ relative to the inertial frame $\mathcal{N}$ is given by

$$\boldsymbol{\omega}_{\mathcal{O}/\mathcal{N}} = \dot{f}\hat{\boldsymbol{o}}_h \tag{7.2}$$

where $\dot{f} = h/r^2$ is the rate of true anomaly. Note that in-plane thrusting does not affect the angular velocity of the orbit frame $\mathcal{O}$ directly – rather, as will be shown, in-plane thrusting in the in-track direction affects the true anomaly acceleration, which in turn affects the true anomaly rate (acceleration does not instantaneously alter velocity). Applying the transport theorem to take two derivatives of $\boldsymbol{r}_d$ with respect to inertial frame:[55]

$$\begin{aligned}\ddot{\boldsymbol{r}}_d = &\left[\ddot{r}_c + \ddot{x} - \ddot{f}y - 2\dot{f}\dot{y} - \dot{f}^2(r_c + x)\right]\hat{\boldsymbol{o}}_r \\ &+ \left[\ddot{y} + 2\dot{f}(\dot{r}_c + \dot{x}) + \ddot{f}(r_c + x) - \dot{f}^2 y\right]\hat{\boldsymbol{o}}_\theta + \ddot{z}\hat{\boldsymbol{o}}_h\end{aligned} \tag{7.3}$$

This kinematic expression can be simplified by developing expressions for the true anomaly acceleration $\ddot{f}$ and chief radial acceleration $\ddot{r}_c$. Recalling that the chief angular momentum magnitude is given by $h = r_c^2\dot{f}$, differentiate and apply Euler's equation $\dot{h} = r_c a_\theta$ to show that the true anomaly acceleration is

$$\ddot{f} = -\frac{2\dot{r}_c\dot{f}}{r_c} + \frac{a_\theta}{r_c} \tag{7.4}$$

where $a_\theta$ is the in-track component of the chief thrust vector $\boldsymbol{a}_t = a_r\hat{\boldsymbol{o}}_r + a_\theta\hat{\boldsymbol{o}}_\theta$. Writing the chief position in the orbit frame as $\boldsymbol{r}_c = r_c\hat{\boldsymbol{o}}_r$, and applying the transport theorem twice:

$$\ddot{\boldsymbol{r}}_c = (\ddot{r}_c - r_c\dot{f}^2)\hat{\boldsymbol{o}}_r + a_\theta\hat{\boldsymbol{o}}_\theta \tag{7.5}$$

Assuming two-body dynamics, the inertial acceleration vector of the chief is written as:

$$\ddot{\boldsymbol{r}}_c = -\frac{\mu}{r_c^3}\boldsymbol{r}_c + \boldsymbol{a}_t = \left(a_r - \frac{\mu}{r_c^2}\right)\hat{\boldsymbol{o}}_r + a_\theta\hat{\boldsymbol{o}}_\theta \tag{7.6}$$

Equating the radial components of Equations (7.5)-(7.6), the chief radial acceleration is:

$$\ddot{r}_c = r_c\dot{f}^2 - \frac{\mu}{r_c^2} + a_r \tag{7.7}$$

Substituting Equations (7.4) and (7.7) into Equation (7.3), the inertial acceleration vector of the deputy becomes:

$$\begin{aligned}\ddot{\boldsymbol{r}}_d = &\left[\ddot{x} - 2\dot{f}\left(\dot{y} - y\frac{\dot{r}_c}{r_c}\right) - \dot{f}^2 x - \frac{\mu}{r_c^2} + a_r - \frac{y}{r_c}a_\theta\right]\hat{\boldsymbol{o}}_r \\ &+ \left[\ddot{y} + 2\dot{f}\left(\dot{x} - x\frac{\dot{r}_c}{r_c}\right) - \dot{f}^2 y + (r_c + x)\frac{a_\theta}{r_c}\right]\hat{\boldsymbol{o}}_\theta + \ddot{z}\hat{\boldsymbol{o}}_h\end{aligned} \tag{7.8}$$

The unforced, two-body deputy equations of motion are given by

$$\ddot{\boldsymbol{r}}_d = -\frac{\mu}{r_d^3}\boldsymbol{r}_d = -\frac{\mu}{r_d^3}(r_c + x)\hat{\boldsymbol{o}}_r - \frac{\mu}{r_d^3}y\hat{\boldsymbol{o}}_\theta - \frac{\mu}{r_d^3}z\hat{\boldsymbol{o}}_h \tag{7.9}$$

where the deputy radius is $r_d = \sqrt{(r_c + x)^2 + y^2 + z^2}$. Finally, equating the kinematics in Equation (7.8) with the dynamics in Equation (7.9) gives the exact nonlinear relative equations of motion of the deputy with respect to the chief, which admits in-plane thrusting:

$$\ddot{x} - 2\dot{f}\left(\dot{y} - y\frac{\dot{r}_c}{r_c}\right) - \dot{f}^2 x - \frac{\mu}{r_c^2} + a_r - \frac{y}{r_c}a_\theta = -\frac{\mu}{r_d^3}(r_c + x) \tag{7.10a}$$

$$\ddot{y} + 2\dot{f}\left(\dot{x} - x\frac{\dot{r}_c}{r_c}\right) - \dot{f}^2 y + (r_c + x)\frac{a_\theta}{r_c} = -\frac{\mu}{r_d^3}y \tag{7.10b}$$

$$\ddot{z} = -\frac{\mu}{r_d^3}z \tag{7.10c}$$

Note that if thrusting is turned-off, i.e., $\boldsymbol{a}_t = \boldsymbol{0}$, the relative motion equations reduce to the unforced form derived in Reference 55. Since linearization is not applied, Equations (7.10) are valid for arbitrarily large relative motion. Furthermore, Equations (7.10) allow the chief orbit to be eccentric – the only assumption made in the derivation of these equations is that two-body dynamics apply for both the deputy debris object and chief re-orbit system, and the only perturbation to the chief's orbital motion is that of the in-plane thrust vector $\boldsymbol{a}_t$.

### 7.2.2 Efficiency Factor for Re-orbit Maneuvers

It is well-known that thrusting along the instantaneous velocity vector direction generates maximum increase in the semi-major axis.[55,65] For the near-circular, low-thrust re-orbit trajectories considered in this thesis, the in-track direction is approximately oriented along the instantaneous velocity direction (i.e., small flight path angle). Assuming that the maximum available thrust acceleration $a_{\max}$ is continuously applied during orbit raising, an *efficiency factor* $\gamma$ for the maneuver may be defined such that the thrust vector becomes:

$$\boldsymbol{a}_t = a_{\max}\sqrt{1 - \gamma^2}\hat{\boldsymbol{o}}_r + \gamma a_{\max}\hat{\boldsymbol{o}}_\theta \tag{7.11}$$

In this formulation, $\gamma = 1$ yields $\boldsymbol{a}_t = a_{\max}\hat{\boldsymbol{o}}_\theta$, that is, maximum available thrust is directed along the in-track direction for maximum increase in SMA.[1] Applying maximum available thrust in the in-track direction is appropriate for general re-orbit maneuvers at GEO, since this minimizes the duration of the transfer, which is lengthy for mN levels of thrust (recall Figure 6.3). Conversely, $\gamma = 0$ yields $\boldsymbol{a}_t = a_{\max}\hat{\boldsymbol{o}}_r$, i.e., maximum available thrust is directed along the radial direction. Although this thrust direction still provides an increase in SMA, this rate of increase is minimal, since the Gauss variational equation for the SMA is[55]

$$\frac{\mathrm{d}a}{\mathrm{d}t} = \frac{2a^2}{h}\left[e\sin(f)a_r + \frac{p}{r}a_\theta\right] \tag{7.12}$$

which shows that the effectiveness of the radial thrust component is reduced first by $\sin(f)$, then by the near-zero eccentricity (or, any thrust component not directed along the velocity vector direction does no work on the re-orbit system to increase its two-body orbit energy).

Letting $\alpha$ be the angle in the orbit plane directed from the local radial direction $\hat{\boldsymbol{o}}_r$, the thrust vector of the re-orbit system can also be expressed in the form:

$$\boldsymbol{a}_t = a_{\max}\cos(\alpha)\hat{\boldsymbol{o}}_r + a_{\max}\sin(\alpha)\hat{\boldsymbol{o}}_\theta \tag{7.13}$$

Equating the components of Equations (7.11) and (7.13), the efficiency factor is $\gamma = \sin(\alpha)$, and is thus dependent on the angle $\alpha$ of the thrust vector in the orbit plane. In this chapter, $\alpha$ is restricted to $0° \leq \alpha \leq 180°$, such that the thrust vector $\boldsymbol{a}_t$ never has a component in the $-\hat{\boldsymbol{o}}_\theta$ direction, which would serve to decrease the SMA during re-orbit via Equation (7.12).

### 7.2.3 Formulation of Bisection Guidance Strategy

In the event of a conjunction during re-orbit that warrants evasive action, a guidance strategy must be applied to tune the efficiency factor $\gamma$—by adjusting the in-plane angle of the thrust vector—such that the re-orbit system misses the conjuncting object by a specified distance at the predicted collision epoch, as conceptualized in Figure 7.1. During nominal

[1] Recall that this is the manner in which all surveyed re-orbit trajectories are propagated in Section 6.3.

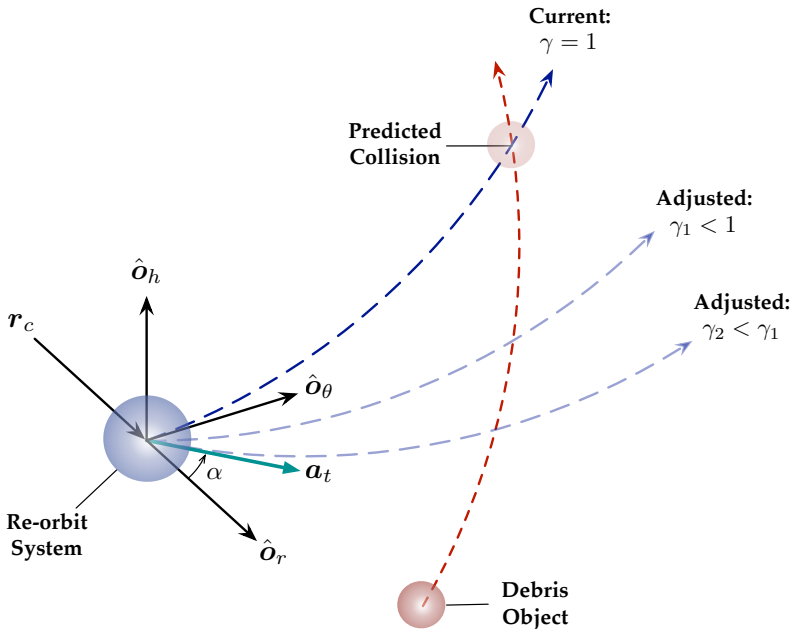


Figure 7.1: In-plane guidance concept for low-thrust debris avoidance.

orbit raising, the re-orbit system maintains $\gamma = 1$, but if a potential collision is detected at a future time, the guidance system must decrease the efficiency factor by applying a larger thrust component $a_r$ in the radial direction. In this manner, the rate of increase in SMA is temporarily slowed, such that the conjuncting object misses by a specified in-track distance $y \neq 0$ when $x = z = 0$ (recall that $x = y = z = 0$ indicates a collision in that the deputy is at the location of the chief, i.e., the origin of the Hill frame). This desired miss distance can be drawn from the largest position coordinate uncertainty for the debris object (the major axis of its covariance ellipsoid), a spherical "keep-out" zone, or the superposition thereof.

Inasmuch as sufficient lead time is available prior to the collision epoch given the maneuverability of the re-orbit system, a predictor-corrector method that uses Equations (7.10) in tandem with a bisection root-finding method can be applied to achieve the desired miss distance. In this guidance strategy, the relative equations of motion in Equations (7.10) are propagated forward to the collision epoch using the current thrust direction. The in-plane thrust angle $\alpha$ is then iteratively adjusted via root bisection to converge on the angle $\alpha^*$ that

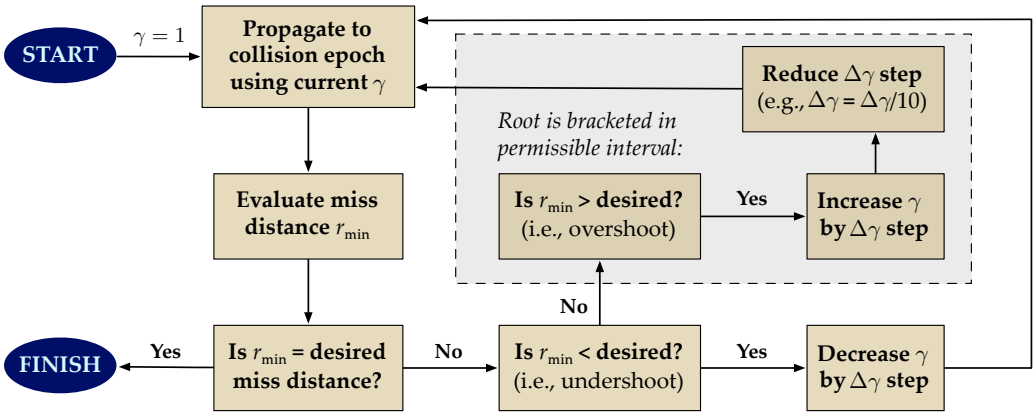


Figure 7.2: Flowchart for computer implementation of bisection guidance strategy.

achieves the desired miss distance at the collision epoch. This "single-shooting" method is fast, robust, and well-suited to an autonomous re-orbiting system that uses environmental sensing to detect the debris environment prior to a potential conjunction event. A flowchart outlining the bisection guidance strategy for active debris avoidance is shown in Figure 7.2.

Since numerical integration of Equations (7.10) requires initial conditions for the conjuncting debris object, the guidance system must have knowledge of the relative trajectory of the conjuncting object in the Hill frame, which can be obtained with (a) traditional, on-ground sensing and inertial orbit determination, or (b) onboard sensing and relative orbit determination using a batch least-squares or sequential state filter, in tandem with relative range and angles measurements. Furthermore, Equations (7.10) contain the chief radius $r_c$ and radial rate $\dot{r}_c = \dot{\boldsymbol{r}}_c \cdot \hat{\boldsymbol{o}}_r$, such that the re-orbiting system must have knowledge of its own inertial position and velocity vectors, in addition to the thrust vector $\boldsymbol{a}_t$ and in-plane thrust angle $\alpha$. This state knowledge can be obtained with (a) traditional, on-ground sensing and inertial orbit determination, (b) by applying a parametric form of position and velocity as a function of elapsed time, using the analytic results in Equations (6.5)-(6.6), for example, or (c) a combination thereof. Although not simulated in this thesis, the in-plane thrust angle must be updated at a predetermined frequency during the entirety of the debris approach, to account for navigation and force model errors, thruster performance uncertainties, and

other error sources not modeled in the two-body framework of Equations (7.10).[2]

Figure 7.3 shows several example approach geometries in the Hill frame to illustrate the effectiveness of the bisection guidance strategy for evading a conjuncting debris object with low thrust propulsion. Using a 1 mN thrust level with a desired miss distance of 5 km at the simulated collision time of 24 hours from the start epoch, Figure 7.3 provides propagated trajectories without guidance (i.e., in-track thrusting only), and with bisection guidance applied. In all three cases, the bisection method converges on $\gamma = 0.706$ to achieve the specified miss distance of 5 km at the predicted collision epoch. Without the guidance applied, a collision occurs at the origin of the Hill frame – with bisection guidance activated, however, the relative trajectory of the conjuncting object is altered such that it achieves zero radial position with nonzero in-track position at the collision epoch (i.e., $x = 0$ with $y \neq 0$).

To illustrate the effect of delaying the start time of the avoidance maneuver, Figure 7.4 provides the trajectory example of Figure 7.3(b), if the conjuncting object is detected not 24 hours in advance of the predicted collision, but 18, 12, and 6 hours prior to the collision. In Figure 7.3(b), the bisection method converges on $\gamma = 0.706$ to achieve the miss distance of 5 km. If, as in Figure 7.4(a), the object is detected 18 hours prior to the collision instead of 24 hours, an efficiency of $\gamma = 0.471$ is required to maintain this 5 km separation at the collision epoch. In Figures 7.4(b)-7.4(c), this guidance strategy does not have enough lead time to alter the relative trajectory such that 5 km separation is achieved, i.e., bisection fails because the root $\alpha^*$ cannot be bracketed in the allowable range $0 \leq \alpha \leq 180^\circ$. Applying maximum available thrust in the negative radial direction ($\gamma = 0$) yields a miss distance of 2.92 km for the 12-hour detection in Figure 7.4(b), and ~430 m for the 6-hour detection in Figure 7.4(c). It is thus of critical importance to evaluate the tradeoffs among thrust acceleration, desired miss distance, and required detection time, assuming perfect knowledge in the absence of representative error sources, to establish "best-case" performance limits for this method.

[2] In this manner, the *open-loop*, "single-shooting" guidance strategy becomes *closed-loop* and robust in that the desired miss distance can be achieved even in the presence of error sources and unmodeled disturbances.

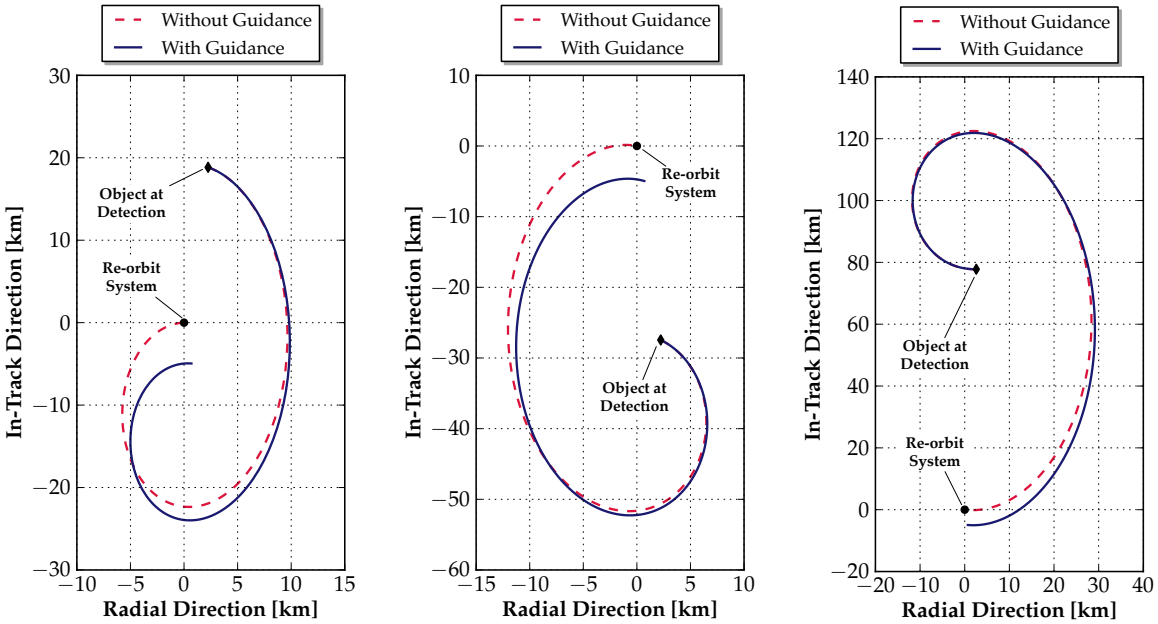


(a) First example trajectory. (b) Second example trajectory. (c) Third example trajectory.

Figure 7.3: Three examples of bisection guidance technique, which converges on $\gamma = 0.706$ to achieve a specified miss distance of 5 km at the predicted collision time of 24 hours out.

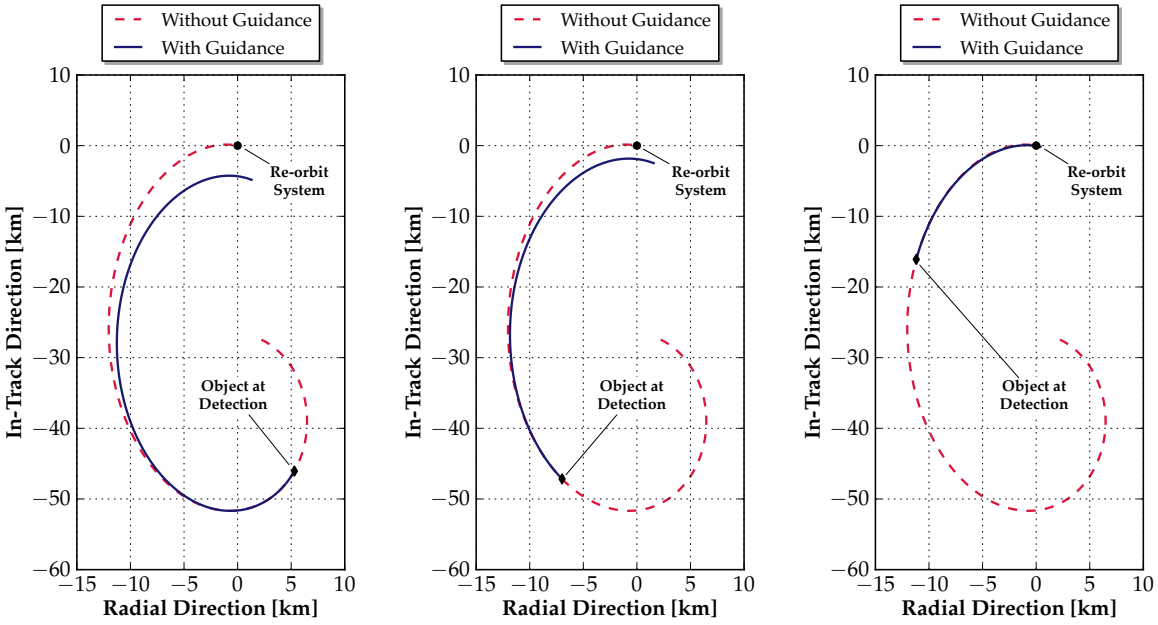


(a) Detection 18 hours prior. (b) Detection 12 hours prior. (c) Detection 6 hours prior.

Figure 7.4: Convergence of and the efficiency factor $\gamma$ resulting from bisection method are dependent upon the lead time with which the object is detected prior to the collision time.

## 7.3 Performance of Guidance Strategy for Debris Avoidance

### 7.3.1 Development of Prototype Collision Scenarios

To quantify "best-case" performance bounds for the bisection guidance method, representative approach geometries in the local Hill frame, i.e., prototype conjunction geometries that a re-orbit system could encounter during orbit raising, must first be constructed. Then, these baseline scenarios are applied with a two-dimensional sweep over thrust level and miss distance, to assess the minimum detection times required to maintain the desired miss distances at the collision epoch for each surveyed thrust acceleration. Assuming two-body dynamics, Figure 7.5 provides three collision scenarios that could occur for a re-orbit system during orbit raising from the GEO altitude to a super-synchronous disposal orbit:

(1) *Case 1.* Collision due to a semi-major axis difference, in which the re-orbit system asymptotically approaches the object at the collision point with nearly zero relative velocity at impact (i.e., re-orbit trajectory "spirals-up" to the conjunction altitude).

(2) *Case 2.* Collision due to an eccentricity difference, in which the system approaches the object at a point of intersection between two, coplanar orbits with $e_1 \neq e_2$, with 10's of m/s of relative velocity at impact (assuming typical eccentricities at GEO).

(3) *Case 3.* Collision due to an inclination difference, in which the system approaches the object at one of the orbital nodes, i.e., points of intersection between two, non-coplanar orbits with $i_1 \neq i_2$, with 100's - 1000's of m/s of relative velocity at impact.

Cases 1 and 2 involve in-plane relative motion only, while Case 3 has out-of-plane relative motion. Noting that relative velocity at impact increases by an order of magnitude between each of these cases, the prototype scenarios in Figure 7.5 serve as the means for comparing bisection performance bounds under successively-increasing collision velocity. Using data from the GEO re-orbit conjunctions study in Chapter 6, Figure 7.6 provides a histogram of the relative velocity for all conjunction events within 50 km detected across all seven thrust

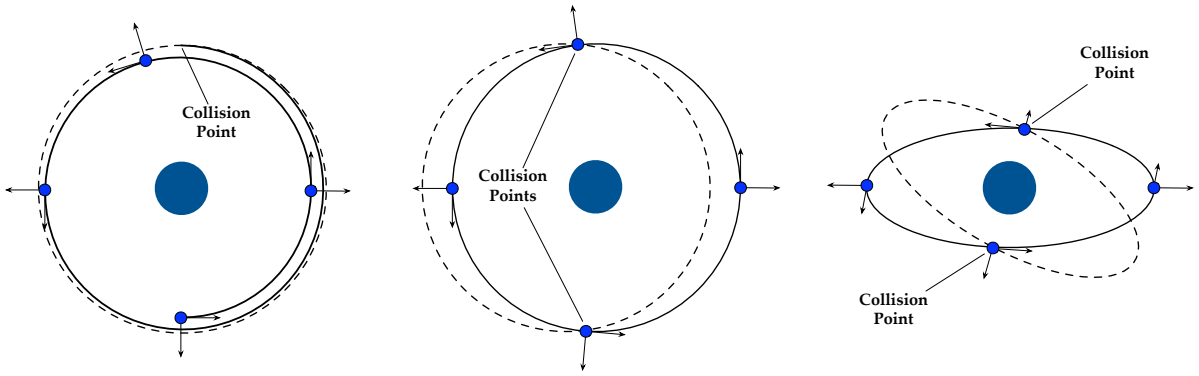


(a) Case 1: SMA difference. (b) Case 2: Eccentricity difference. (c) Case 3: Inclination difference.

Figure 7.5: Representative GEO collision geometries for testing bisection debris avoidance strategy, where collision speed increases from SMA case at left to inclination case at right.

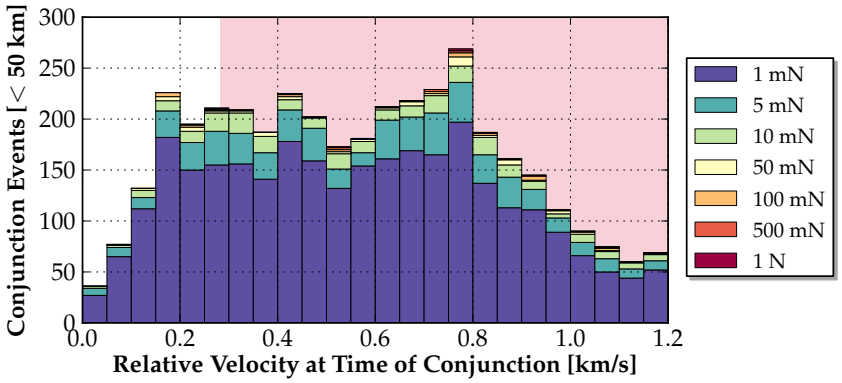


Figure 7.6: Distribution of 50 km conjunction velocities, derived from re-orbit conjunction data in Chapter 6, by thrust level. Shaded region illustrates catastrophic collision regime.

accelerations surveyed. This histogram shows an extensive range of conjunction velocities are possible for simulated continuous-thrust re-orbit trajectories. In particular, of the 4099 conjunction events detected within 50 km across all surveyed thrust levels, 80.2% are at or above the catastrophic relative velocity threshold of 0.2828 km/s, detailed in Section 6.3.[46] Although the simulated conjunctions in Chapter 6 cannot be categorized exclusively under one of the prototype cases in Figure 7.5—since conjunctions due to a combination of orbit element differences occur in practice—the histogram in Figure 7.6 shows that the majority of simulated conjunctions fall under Cases 2-3 in terms of relative velocity at conjunction.

To derive specific eccentricity and inclination differences to apply to these prototype collision scenarios, Chapter 6 conjunction events within 10 km at the 1 mN thrust level are examined. Of the conjunction events detected at this 10 km distance threshold and thrust level, one conjunction results from an eccentricity difference $\Delta e = 0.028$ (relative speed of 86 m/s), and another results from an inclination difference of $\Delta i = 12.1^\circ$ (relative speed of 649 m/s). The semi-major axis difference scenario is simulated by propagating the re-orbit system forward from the GEO radius under continuous, in-track thrust until the specified collision epoch; the Cartesian state of the re-orbit system is then assigned to the conjuncting object, which is then reverse-propagated to the simulation start epoch under two-body dynamics to provide the required initial conditions. Figure 7.7 illustrates the resulting approach trajectories in the Hill frame for each of the three prototype scenarios in Figure 7.5, using a 1 mN thrust level and specifying that the collision will occur 24 hours in the future, inasmuch as the bisection guidance method is not applied to alter the approach geometry.

### 7.3.2 Performance Bounds of Bisection Guidance Method

Performance bounds for the bisection guidance method are investigated with a two-dimensional sweep over thruster acceleration and miss distance at the collision epoch. For each thrust acceleration and desired miss distance, an auxiliary bisection technique is used to evaluate the minimum detection time required to maintain the surveyed miss distance at the collision time, i.e., the latest possible time that the debris object can be detected such that the re-orbit system can still evade the object while achieving the desired miss distance. As it is more advantageous for the re-orbit system the earlier it detects a conjuncting object —since resulting efficiency factors will be closer to the $\gamma = 1$ maximum—this performance study illustrates worst-case, full-radial performance $(\gamma = 0)$ under "best-case" knowledge, that is, perfect chief and deputy initial conditions, no navigation or force model errors, etc.

Figure 7.8 shows bisection performance bounds for each of the three representative collision scenarios in Figure 7.7. Thrust accelerations ranging from $10^{-6}$ m/s$^2$ to $10^{-3}$ m/s$^2$

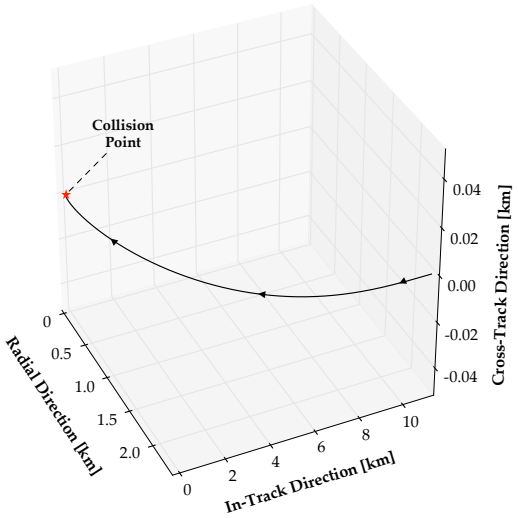


(a) Case 1: Asymptotic SMA approach.

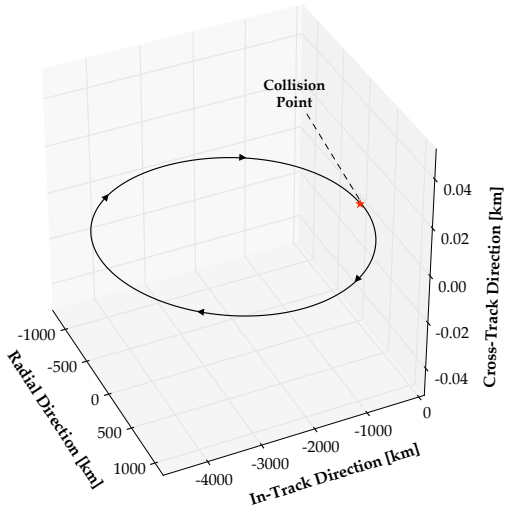


(b) Case 2: Eccentricity difference $\Delta e = 0.028$.

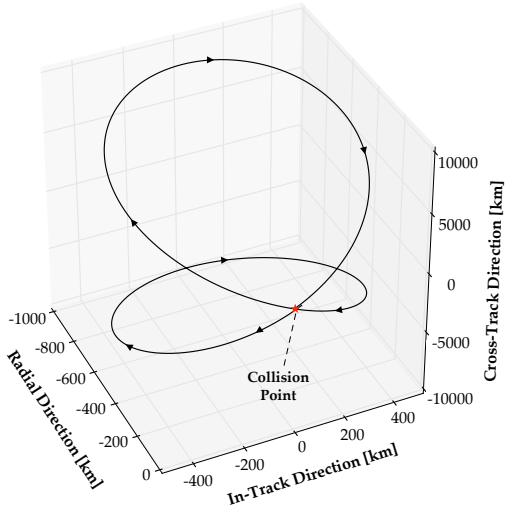


(c) Case 3: Inclination difference $\Delta i = 12.1°$.

Figure 7.7: Relative Hill frame trajectories for representative GEO collision geometries.

(i.e., 1 mN to 1 N of thrust force for a 1000 kg re-orbit system) are surveyed in tandem with miss distances ranging from 10 m to 10 km at the collision epoch. For example, if a Case 1 approach geometry is assumed, Figure 7.8(a) shows that a re-orbit system with $10^{-6}$ m/s$^2$ of thrust acceleration requires 6 hours prior to the predicted collision epoch, at minimum, to miss this object by ∼100 m using the bisection guidance strategy. If the object is detected

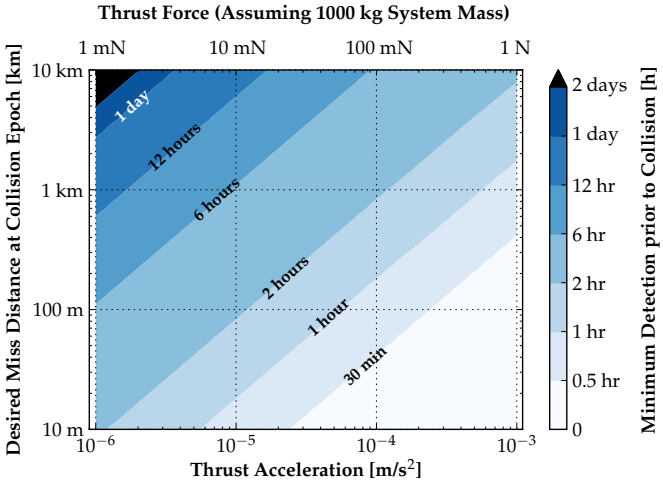


(a) Case 1 performance: Asymptotic SMA approach.

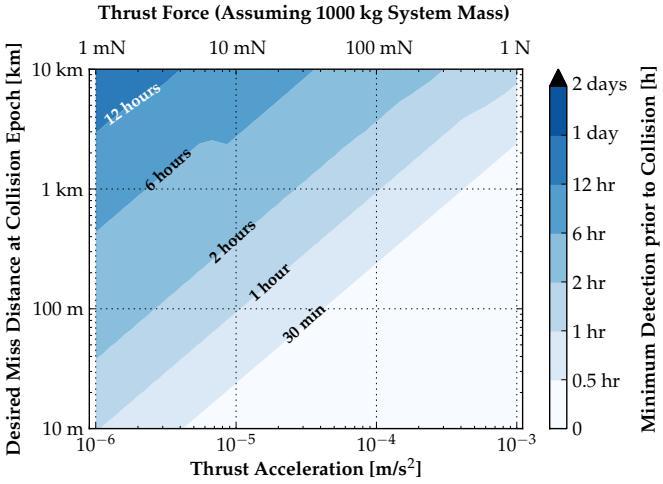


(b) Case 2 performance: Eccentricity difference $\Delta e$.

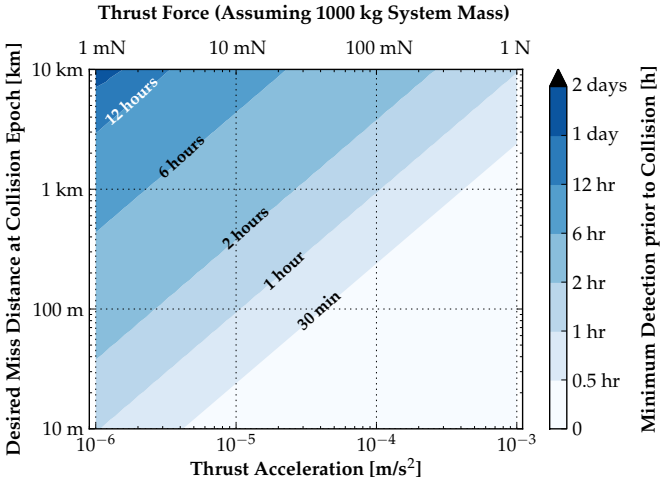


(c) Case 3 performance: Inclination difference $\Delta i$.

Figure 7.8: Performance bounds of bisection method for derelict avoidance, illustrated for various miss distances with the prototype GEO collision geometries in Figures 7.5 and 7.7.

earlier than this bound, the resulting efficiency factor will improve; conversely, if the object is detected any later than this bound, bisection root-bracketing fails, and the specified miss distance is no longer achievable given the maneuverability of the re-orbit system. Note the latter does not state a collision *will* occur; rather, the desired miss distance is not achievable.

The contours in Figure 7.8 illustrate that as the thrust acceleration decreases, and the desired miss distance increases, the minimum required detection time rises exponentially. This is an intuitive result, for the less maneuverability a re-orbit system has, the sooner its guidance subsystem must know in advance of a predicted conjunction to begin altering the in-plane thrust angle such that the desired miss distance is achieved at the collision epoch. The white triangular regions in the southeast corners of Figure 7.8 are those regions in this parameter space in which less than 30 minutes of lead time are required to miss the derelict using a full radial burn ($\gamma = 0$). Interestingly, performance bounds improve as the relative velocity of the encounter increases, e.g., using $10^{-6}$ m/s$^2$ of thrust acceleration and a 100 m miss distance, Case 1 in Figure 7.8(a) requires a minimum detection time of approximately 6 hours, but this is reduced to approximately 3 hours in Figure 7.8(c) for Case 3 geometry. This is a consequence of faster relative motion between the re-orbit system and conjuncting object at the collision epoch. Using a least-squares curve-fitting tool, the performance plots for Cases 1 and 3 in Figures 7.8(a) and 7.8(c) can be approximated by the analytic functions

$$t_{\text{min}}(\tilde{x}) \approx \exp(0.2396\tilde{x}^2 + 0.4124\tilde{x} + 0.2184) - 0.5572 \quad \text{[Case 1]} \tag{7.14}$$

$$t_{\text{min}}(\tilde{x}) \approx \exp(0.2075\tilde{x}^2 + 0.4201\tilde{x} + 0.2583) - 0.9666 \quad \text{[Case 3]} \tag{7.15}$$

where $\tilde{x} \equiv \frac{1}{\sqrt{2}} \left[\log_{10}(a_{\text{max}}) - \log_{10}(d_{\text{miss}})\right]$. In this formulation, $a_{\text{max}}$ is the thrust acceleration, $d_{\text{miss}}$ the desired miss distance, and $t_{\text{min}}$ the minimum detection time required to maintain $d_{\text{miss}}$ at the collision time. The coefficient of determination that measures goodness of fit is $\mathcal{R}^2 = 0.976$ for Case 1 and $\mathcal{R}^2 = 0.980$ for Case 3, indicative of a good fit to the minimum detection times evaluated in the thrust/distance parameter space illustrated in Figure 7.8.

Note that although bisection performance bounds for Cases 2 and 3 in Figures 7.8(b)-

7.8(c) are qualitatively similar, a bump observed on the 6-hour contour line in Figure 7.8(b) is not exhibited in Figure 7.8(c). When computing minimum detection times in Figure 7.8, trajectories are propagated using maximum available thrust in both the positive radial ($\hat{\boldsymbol{o}}_r$) and negative radial ($-\hat{\boldsymbol{o}}_r$) directions, since these directions both correspond to $\gamma = 0$ (i.e., $\alpha = 0°$ and $\alpha = 180°$, respectively). As a consequence of the approach geometry for Case 2 in Figure 7.7(b), thrusting in the $-\hat{\boldsymbol{o}}_r$ direction gives larger miss distances southwest of the bump, and thrusting in the $\hat{\boldsymbol{o}}_r$ direction gives larger miss distances northeast of the bump. This observed "bump discontinuity" does not appear in Cases 1 and 3, since thrusting in the $-\hat{\boldsymbol{o}}_r$ direction provides larger miss distances across the entirety of the parameter space.

## 7.4 Conclusions from Research Goal

A computationally efficient guidance strategy for debris avoidance during low-thrust re-orbit to a super-synchronous disposal orbit is investigated in this chapter. The guidance strategy employs a bisection root-finding method to converge on the in-plane thrust angle that gives the desired miss distance at the predicted collision epoch, inasmuch as sufficient lead time is available prior to the conjunction. Designed with simple-yet-robust autonomy in mind, this bisection guidance strategy is ultimately a component of a larger, "sense and avoid" system to mitigate collision risk during orbit raising at end-of-life while minimizing human-in-the-loop requirements. When coupled with environmental sensing and an on-board, relative state estimator, bisection guidance can be applied to safely avoid specified "no-fly" regions around conjuncting derelicts, while continuing to increase the semi-major axis during a re-orbit. The performance bounds quantified in this chapter illustrate that for typical conjunction velocities probable during GEO re-orbit, a desired miss distance of 1-2 km requires less than 12 hours of lead time for all surveyed thrust levels ranging from $10^{-6}$ m/s$^2$ to $10^{-3}$ m/s$^2$. To compliment Chapter 6—which shows that conjunction challenges during GEO re-orbit can be reduced by increasing the thrust level and/or timing the start of the re-orbit burn appropriately—this chapter demonstrates that any remaining collision

risk can be safely mitigated with bisection guidance for online avoidance of debris objects.

## 7.5 Continuing Research Questions

For continuing research in this area, the following research questions are of interest:

(1) The bisection method developed in this chapter applies maximum available thrust in the radial/in-track plane of the local Hill frame to evade a conjuncting derelict. Can related guidance methods be developed that allow for (a) variable thrust magnitude, (b) an out-of-plane thrust vector component, (c) coasting periods, in which the thrust vector is turned-off (i.e., $\boldsymbol{a}_t = \mathbf{0}$), or (d) an optimal combination thereof? Investigating how to incorporate coasting periods would be especially useful, since satellites with thrusters fixed in the body frame would have to execute an attitude maneuver to achieve the thrust vector heading commanded by bisection guidance.

(2) Can optimal control theory be leveraged to develop an optimal, continuous-thrust guidance law for derelict avoidance, in which the thrust profile is adjusted to minimize a cost function $\mathcal{J}$ while simultaneously enforcing various path constraints?

(3) What are the effects of various error sources—such as chief and deputy state knowledge, navigation and force model errors, thruster pointing/execution errors, etc.—on convergence, robustness, and applicability of the bisection guidance technique?

(4) Using the mean conjunctions per trajectory metric in Chapter 6 in tandem with the bisection method developed in this chapter, can a lifetime fuel budget be estimated for an ADR system at GEO that uses low-thrust propulsion to perform the re-orbit for a variety of derelict GEO objects? Note that once in super-synchronous orbit, a re-orbit system must burn against the velocity vector to return to the GEO altitude.

# Chapter 8

## Conclusions

In this thesis, entitled "Characterizing Longitude-Dependent Orbital Debris Congestion in the Geosynchronous Orbit Regime," multiple dimensions of the problem of orbital debris at GEO are investigated. The GEO regime is home to hundreds of large, high-value satellites from the civil, commercial, and defense sectors, leveraged for applications ranging from communications and data relay to weather monitoring and classified surveillance activities. As the lack of environmental cleansing mechanisms at the GEO altitude renders the lifetimes of objects in this regime indefinitely long, debris generated near GEO remains there permanently – until environment remediation via a cost-effective ADR system is synthesized, demonstrated, and implemented to remove large-scale derelicts and small-scale, undetectable fragmentation particulates that threaten the integrity of on-orbit GEO assets. Although recent re-orbit statistics are promising in that they suggest increased adherence to end-of-life mitigation guidelines—and ultimately, a growing international desire to preserve the long-term usability of this regime—complete global compliance is challenging to reach without an internationally-recognized legal framework for enforcing space sustainability laws (especially at GEO, where profit is proportional to operational lifetime). Thus, it will become increasingly apparent that *reactive mitigation* initiatives must be augmented by *proactive remediation* initiatives to ultimately "solve" the problem of orbit debris at GEO.

Since operational GEO satellites are required to maintain designated longitude slots, operators cannot execute a phase shift in true anomaly (as can be done at LEO) to mitigate

risk incurred by conjuncting debris. Currently, the large-scale debris population at GEO is sparse enough that collision avoidance maneuvers can be built-in to routine maintenance burns. As the GEO debris population continues to increase, however, due to (a) mitigation noncompliance, (b) lack of an operational ADR system, or (c) older, non-passivated rocket bodies and payloads that threaten to explode, the costs to operate in the GEO environment will continue to rise in proportion. This thesis research thus serves to build context for the problem of orbital debris at GEO, by identifying and characterizing longitude-dependent congestion trends to "provide a foundation for future active risk reduction options."[1]

In Chapter 2, longitude-dependent congestion generated by the large-scale, unclassified, and trackable debris population currently at GEO is forecasted and characterized over a five-year prediction period. The near-miss event metric leveraged for quantifying localized congestion is introduced, and position and velocity risk functions useful for assigning a threat level to each near-miss event are presented. Congestion predictions indicate that controlled satellites in the longitude slots neighboring the two gravitational wells are subject to 4-8 near-misses per day at 50 km, four times the 1-2 near-misses per day experienced in the least congested longitude slots (i.e., covering the Atlantic and Pacific Oceans). Risk data—accumulated either globally or locally across a subset of longitude slots—is used to prioritize the debris population for ADR target selection. In particular, the librating class derelicts collectively account for 76% of globally accumulated risk over a five-year period, even though this subset comprises only 14% of the RSO population at GEO. In the vicinity of the Western gravity well, the top 9 class L2 derelicts alone are responsible for 50% of the risk locally accumulated in that region during the five-year congestion forecasting period.

In Chapter 3, analytical theory describing inclination and RAAN variations driven by luni-solar perturbations is merged with observational data to explain apparent anomalous behavior exhibited by eight derelicts with unsynchronized latitude cycles. The phase por-

[1] See D. McKnight, "Pay Me Now or Pay Me More Later: Start the Development of Active Orbital Debris Removal Now," *White Paper*, Integrity Applications, Inc., 2010.

trait for the doubly-averaged equations describing inclination and RAAN variations at the GEO altitude admit two types of behavior, one in which the RAAN circulates in the phase space (Type I), and the other in which the RAAN continually regresses (Type II). "Outlier" objects exhibiting either partially or fully out-of-phase latitude cycles follow Type II curves, such that these objects shift from asynchronous (with the rest of the debris population) to synchronous—and back—over the course of this 53-year inclination/RAAN progression.

In Chapter 4, longitude-dependent congestion trends under the effect of a representative, linearly-increasing GEO launch traffic model are evaluated. Historical, present, and projected operational orbit data are applied to construct probability density functions that sample the semi-major axis, eccentricity, inclination, and longitude slot for new controlled satellites artificially created during long-term forecasting. In tandem with a launch instantiation procedure, this population augmentation method is leveraged to simulate congestion trends over a 50-year forecast – with and without mitigation compliance at end-of-life. Results demonstrate that even under optimistic, 80% re-orbit compliance, daily near-miss events at 300 km in the vicinity of the gravitational wells will double in 50 years, illustrating the need for a coupling between aggressive mitigation compliance and active removal.

In Chapter 5, longitude-dependent congestion generated by fragmentation events—explosions and collisions—in the GEO regime is evaluated. The NASA Standard Breakup Model is applied to sample initial conditions for the fragment distribution resulting from a simulated breakup event, and the longitude of the parent body at the epoch of fragmentation is varied to demonstrate how the severity of a breakup event at GEO depends upon initial longitude. A breakup occurring in the vicinity of one gravitational well is a "worst-case" scenario in that fragments are more likely to begin librating about the well, resulting in bi-annual bunching at the amplitude of the parent body's libration motion. Inasmuch as the semi-major axis distribution resulting from a fragmentation event can be estimated, the harmonic oscillator model presented in this chapter can be applied to predict to first order the specific times and longitudes at which congestion spikes will occur (in the short term).

In Chapter 6, the conjunction challenges for operational satellites or space-tug ADR concepts using low-thrust propulsion to achieve a super-synchronous graveyard orbit are quantified. A two-dimensional sweep over initial longitude and inclination is performed, and conjunctions with the TLE debris population are detected at various distance thresholds for each continuous-thrust re-orbit trajectory surveyed. Results show that on average, the number of conjunction events expected for a given thrust level and distance threshold rises hyperbolically as the thrust level decreases, in correlation with the burn duration for a given thrust level. Furthermore, examination of the conjunction events in semi-major axis and longitude space indicates locations in this space in which conjunction events are more likely. Beneficially, timing the maneuver appropriately—that is, such that the re-orbit system is out-of-phase at the start of the transfer with the synchronized latitude motion of the local debris population—reduces or even eliminates the expected number of conjunctions.

In Chapter 7, a computationally-efficient guidance strategy for debris avoidance during low-thrust orbit raising to a super-synchronous configuration is presented. The guidance strategy uses a bisection root-finding method to converge on the in-plane thrust angle that gives the desired miss distance at the predicted collision epoch, inasmuch as sufficient lead time is available prior to the conjunction. When coupled with environmental sensing and an onboard, relative state estimator, bisection guidance can be applied to safely avoid specified "no-fly" zones around conjuncting debris, while continuing to increase the semi-major axis during re-orbit. Performance bounds assessed in this chapter show that for conjunction speeds probable during a re-orbit, a desired miss distance of 1-2 km requires less than 12 hours of advance notice for all surveyed thrust levels from $10^{-6}$ m/s$^2$ to $10^{-3}$ m/s$^2$.

The research presented in this thesis is by no means exhaustive in scope; rather, the intent of this work is to tackle core aspects of the fundamental research questions posed in Chapter 1, and ultimately, demonstrate the increasingly relevant need for ADR in the GEO ring. With more aggressive mitigation standards, timely ADR implementation, and global cooperation, this unique and delicate regime can be preserved for the generations to come.

## Bibliography


[1] D. S. McKnight and F. R. Di Pentino, "New Insights on the Orbital Debris Collision Hazard at GEO," Acta Astronautica, Vol. 85, 2013, pp. 73–82.

[2] P. V. Anderson and H. Schaub, "Local Debris Congestion in the Geosynchronous Environment with Population Augmentation," Acta Astronautica, Vol. 94, February 2014, pp. 619–628.

[3] C.-C. Chao, Applied Orbit Perturbation and Maintenance. The Aerospace Press, 2005.

[4] R. R. Allan, "Perturbations of a Geostationary Satellite by the Longitude-Dependent Terms in the Earth's Gravitational Field," Planetary and Space Science, Vol. 11, August 1963, pp. 1325–1334.

[5] N. Johnson, "Protecting the GEO Environment: Policies and Practices," Space Policy, Vol. 15, 1999, pp. 127–135.

[6] P. Wegener, J. Bendisch, H. Krag, M. Oswald, and S. Stabroth, "Population Evolution in the GEO Vicinity," Advances in Space Research, Vol. 34, 2004, pp. 1171–1176.

[7] R. Jehn, V. Agapov, and C. Hernandez, "The Situation in the Geostationary Ring," Advances in Space Research, Vol. 35, 2005, pp. 1318–1327.

[8] P. Chrystal, D. McKnight, and P. Meredith, "Space Debris: On Collision Course for Insurers?," tech. rep., Swiss Reinsurance Company Ltd, 2011.

[9] T. Yasaka, T. Hanada, and H. Hirayama, "GEO Debris Environment: A Model to Forecast the Next 100 Years," Advances in Space Research, Vol. 23, No. 1, 1999, pp. 191–199.

[10] R. Jehn and C. Hernandez, "International Practices to Protect the Geostationary Ring," Space Debris, Vol. 1, 2001, pp. 221–233.

[11] H. Klinkrad, Space Debris: Models and Risk Analysis. Praxis Publishing, 2006.

[12] J. Wertz and W. Larson, eds., Space Mission Analysis and Design. Microcosm Press, 3 ed., 2007.

[13] P. V. Anderson and H. Schaub, "Local Orbital Debris Flux Study in the Geostationary Ring," Advances in Space Research, Vol. 51, June 2013, pp. 2195–2206.

[14] H. Lewis, G. Swinerd, N. Williams, and G. Gittins, "DAMAGE: A Dedicated GEO Debris Model Framework," Proceedings of the Third European Conference on Space Debris, Vol. 1, March 2001.

[15] J. Bendisch, K. Bunte, H. Klinkrad, H. Krag, C. Martin, H. Sdunnus, R. Walker, P. Wegener, and C. Wiedemann, "The MASTER-2001 Model," Advances in Space Research, Vol. 34, 2004, pp. 959–968.

[16] J.-C. Liou, D. T. Hall, P. H. Krisko, and J. N. Opiela, "LEGEND: A Three-Dimensional LEO-to-GEO Debris Evolutionary Model," Advances in Space Research, Vol. 34, 2004, pp. 981–986.

[17] T. Schildknecht, M. Ploner, and U. Hugentobler, "The Search for Debris in GEO," Advances in Space Research, Vol. 28, No. 9, 2001, pp. 1291–1299.

[18] T. Schildknecht, R. Musci, M. Ploner, G. Beutler, W. Flury, J. Kuusela, J. d. Leon Cruz, and L. d. Fatima Dominguez Palmero, "Optical Observations of Space Debris in GEO and in Highly-Eccentric Orbits," Advances in Space Research, Vol. 34, 2004, pp. 901–911.

[19] L. Anselmo and C. Pardini, "Collision Risk Mitigation in Geostationary Orbit," Space Debris, Vol. 2, 2002, pp. 67–82.

[20] NASA, "Process for Limiting Orbital Debris," NASA-STD-8719.14 Change 4, National Aeronautics and Space Administration, September 2009.

[21] IADC/WG4, "Support to the IADC Space Debris Mitigation Guidelines," tech. rep., IADC, October 2004.

[22] IADC/WG4, "IADC Space Debris Mitigation Guidelines," tech. rep., IADC, September 2007.

[23] N. L. Johnson, "A New Look at the GEO and Near-GEO Regimes: Operations, Disposals, and Debris," Acta Astronautica, Vol. 80, June 2012, pp. 82–88.

[24] W. Flury, "Collision Probability and Spacecraft Disposition in the Geostationary Orbit," Advances in Space Research, Vol. 11, No. 12, 1991, pp. 67–79.

[25] C. Pardini and L. Anselmo, "Influence of the Spacecraft End-of-Life Re-Orbiting Altitude on the Long-Term Collision Risk in the Geostationary Ring," Advances in Space Research, Vol. 28, No. 9, 2001, pp. 1403–1408.

[26] I. Wytrzyszczak and S. Breiter, "Long-Term Evolution of Disposal Orbits Beyond the Geostationary Ring," Advances in Space Research, Vol. 28, No. 9, 2001, pp. 1409–1414.

[27] H. Lewis, G. Swinerd, C. Martin, and W. Campbell, "The Stability of Disposal Orbits at Super-Synchronous Altitudes," Acta Astronautica, Vol. 55, 2004, pp. 299–310.

[28] C.-C. Chao and S. Campbell, "Long-Term Perigee Height Variations of GEO Disposal Orbits - A Revisit," Proceedings of the 4th European Conference on Space Debris (D. Danesy, ed.), ESA/ESOC, 2005.

[29] S. Hobbs, "Disposal Orbits for GEO Spacecraft: A Method for Evaluating the Orbit Height Distributions Resulting from Implementing IADC Guidelines," Advances in Space Research, Vol. 45, 2010, pp. 1042–1049.

[30] T. Yasaka and N. Ishii, "Breakup in Geostationary Orbit: A Possible Creation of a Debris Ring," Acta Astronautica, Vol. 26, No. 7, 1992, pp. 523–530.

[31] D. Oltrogge and D. Finkleman, "Consequences of Debris Events in Geosynchronous Orbit," Proceedings of the 2008 AIAA/AAS Astrodynamics Specialist Conference and Exhibit, No. 2008-7375, August 2008.

[32] B. W. Hansen and M. E. Sorge, "Summarizing the General Effects of Breakup Debris in GEO," Proceedings of the 2013 AAS/AIAA Astrodynamics Specialist Conference, No. 13-844, August 2013.

[33] T. Flohrer, "Classification of Geosynchronous Objects: Issue 16," Tech. Rep. 1, European Space Operations Centre, February 2014.

[34] J.-C. Liou, "An Active Debris Removal Parametric Study for LEO Environmental Remediation," Advances in Space Research, Vol. 47, 2011, pp. 1865–1876.

[35] G. E. Peterson, "Target Identification and Delta-V Sizing for Active Debris Removal and Improved Tracking Campaigns," Proceedings of the International Symposium on Space Flight Dynamics, 2012.

[36] J. R. Quinlan, C. A. Jones, V. Vittaldev, and A. Wilhite, "On the Design of an Active Debris Removal Architecture for Low Earth Orbit Space Debris Remediation," Proceedings of the 2011 AIAA SPACE Conference and Exposition, September 2011.

[37] F. R. Hoots and R. L. Roehrich, "Spacetrack Report No. 3: Models for Propagation of NORAD Element Sets," tech. rep., Office of Astrodynamics, Aerospace Defense Center, December 1980.

[38] D. Vallado, Fundamentals of Astrodynamics and Applications. Microcosm Press, 3 ed., 2007.

[39] D. A. Vallado, P. Crawford, R. Hujsak, and T. S. Kelso, "Revisiting Spacetrack Report No. 3: Revision 2," Proceedings of the 2006 AIAA/AAS Astrodynamics Specialist Conference, August 2006.

[40] T. Flohrer, H. Krag, and H. Klinkrad, "Assessment and Categorization of TLE Orbit Errors for the US SSN Catalogue," Proceedings of the 2008 Advanced Maui Optical and Space Surveillance Technologies Conference, September 2008.

[41] H. Curtis, Orbital Mechanics for Engineering Students. Elsevier Butterworth-Heinemann, 2005.

[42] O. Montenbruck and E. Gill, Satellite Orbits: Models, Methods, Applications. Springer, 2000.

[43] H. Schaub and L. Jasper, "Circular Orbit Radius Control using Electrostatic Actuation for 2-Craft Configurations," Proceedings of the 2011 AAS/AIAA Astrodynamics Specialist Conference, August 2011.

[44] USNO and UKHO, The Astronomical Almanac for the Year 2013. U. S. Nautical Almanac Office with Her Majesty's Nautical Almanac Office, 2013.

[45] M. M. Berry and L. M. Healy, "Implementation of Gauss-Jackson Integration for Orbit Propagation," Journal of the Astronautical Sciences, Vol. 52, July-September 2004, pp. 331–357.

[46] N. L. Johnson, P. H. Krisko, J.-C. Liou, and P. D. Anz-Meador, "NASA's New Breakup Model of Evolve 4.0," Advances in Space Research, Vol. 28, No. 9, 2001, pp. 1377–1384.

[47] K. Luu and C. Sabol, "Effects of Perturbations on Space Debris in Supersynchronous Storage Orbits," tech. rep., Air Force Research Laboratory, October 1998.

[48] V. A. Chobotov, Orbital Mechanics. American Institute of Aeronautics and Astronautics, Inc., 2002.

[49] "Satellite Collision Leaves Significant Debris Clouds," Orbital Debris Quarterly News, Vol. 13, NASA Orbital Debris Program Office, April 2009, pp. 1–2.

[50] K. S. Capelle and J. Sharma, "Geosynchronous Satellite Orbit Pattern: Improvements to SBV Geosynchronous Search," Proceedings of the 2000 Space Control Conference, MIT Lincoln Laboratory, April 2000, pp. 29–42.

[51] J. Sharma, G. H. Stokes, C. v. Braun, G. Zollinger, and A. J. Wiseman, "Toward Operational Space-Based Space Surveillance," Lincoln Laboratory Journal, Vol. 13, No. 2, 2002, pp. 309–334.

[52] L. J. Friesen, D. J. Kessler, and H. A. Zook, "Reduced Debris Hazard Resulting from a Stable Inclined Geosynchronous Orbit," Advances in Space Research, Vol. 13, No. 8, 1993, pp. 231–241.

[53] S. H. Vaughan and T. L. Mullikin, "Long Term Behavior of Inactive Satellites and Debris near Geosynchronous Orbits," Proceedings of the 1995 AAS/AIAA Spaceflight Mechanics Conference, Vol. 89, 1995, pp. 1571–1585.

[54] D. S. McKnight, F. R. Di Pentino, and P. Dingman, "Semi-Empirical Satellite Anomalies Analysis Highlighting Contributions from the Fengyun-1C," Proceedings of the 64th International Astronautical Congress, 2013.

[55] H. Schaub and J. L. Junkins, Analytical Mechanics of Space Systems. American Institute of Aeronautics and Astronautics, Inc., 2nd ed., 2009.

[56] D. S. McKnight, Simulation of On-Orbit Satellite Fragmentations. PhD thesis, University of Colorado at Boulder, 1986.

[57] T. Kelecy, M. Jah, J. Baldwin, and J. Stauch, "High Area-to-Mass Ratio Object Population Assessment from Data/Track Association," Acta Astronautica, Vol. 96, March-April 2014, pp. 166–174.

[58] C. Früh and M. Jah, "Coupled Orbit-Attitude Motion of High Area-to-Mass Ratio (HAMR) Objects including Efficient Self-Shadowing," Acta Astronautica, Vol. 95, February-March 2014, pp. 227–241.

[59] S. Jones, "Negating the Yearly Eccentricity Magnitude Variation of Supersynchronous Disposal Orbits due to Solar Radiation Pressure," Master's thesis, University of Colorado at Boulder, 2013.

[60] IADC/WG4, "IADC Recommendation: Reorbit Procedure for GEO Preservation," tech. rep., IADC, December 1997.

[61] H. Schaub, L. E. Z. Jasper, P. V. Anderson, and D. S. McKnight, "Cost and Risk Assessment for Spacecraft Operation Decisions Caused by the Space Debris Environment," Proceedings of the 65th International Astronautical Congress, International Astronautical Federation, October 2014.

[62] H. Schaub and D. F. Moorer, "Geosynchronous Large Debris Reorbiter: Challenges and Prospects," Journal of the Astronautical Sciences, Vol. 59, No. 1-2, 2012, pp. 165–180.

[63] C. Bombardelli and J. Pelaez, "Ion Beam Shepherd for Contactless Space Debris Removal," Journal of Guidance, Control and Dynamics, Vol. 34, No. 3, 2011, pp. 916–920.

[64] F. Raballand, D. Mignon, and J.-L. Gonnaud, "Eurostar 2000 Disposal on a Graveyard Orbit: Orbit Control Strategy and Operational Implementation," Proceedings of the 4th European Conference on Space Debris, ESA/ESOC, April 2005.

[65] J. E. Prussing and B. A. Conway, Orbital Mechanics. Oxford University Press, 2 ed., 2013.

[66] H. Schaub and J. L. Junkins, "Dynamics and Control of Micro-Robot Swarms: Planar Motion and State Estimation," tech. rep., Texas A & M University, 1998.

[67] N. E. Leonard and E. Fiorelli, "Virtual Leaders, Artificial Potentials and Coordinated Control of Groups," Proceedings of the 40th IEEE Conference on Decision and Control, December 2001.

[68] O. Junge and S. Ober-Blobaum, "Optimal Reconfiguration of Formation Flying Satellites," Proceedings of the 44th IEEE Conference on Decision and Control, December 2005.

[69] D. Izzo and L. Pettazzi, "Autonomous and Distributed Motion Planning for Satellite Swarm," Journal of Guidance, Control and Dynamics, Vol. 30, March 2007.

[70] D. J. Bennet and C. R. McInnes, "Pattern Transition in Spacecraft Formation Flying via the Artificial Potential Field Method and Bifurcation Theory," Proceedings of the 3rd International Symposium on Formation Flying, April 2008.

[71] A. R. Tatsch, Artificial Potential Function Guidance for Autonomous In-Space Operations. PhD thesis, University of Florida, 2006.

[72] C. Louembet and G. Deaconu, "Collision Avoidance in Low-Thrust Rendezvous Guidance using Flatness and Positive B-Splines," Proceedings of the 2011 American Control Conference, June 2011.

[73] R. Epenoy, "Fuel Optimization for Continuous-Thrust Orbital Rendezvous with Collision Avoidance Constraint," Journal of Guidance, Control and Dynamics, Vol. 34, March-April 2011.

[74] A. Richards, T. Schouwenaars, J. P. How, and E. Feron, "Spacecraft Trajectory Planning with Avoidance Constraints using Mixed-Integer Linear Programming," Journal of Guidance, Control and Dynamics, Vol. 25, July-August 2002.

[75] Z.-H. Mao, E. Feron, and K. Bilimoria, "Stability of Intersecting Aircraft Flows under Decentralized Conflict Avoidance Rules," Proceedings of the AIAA Guidance, Navigation, and Control Conference, AIAA, 2000, pp. 1042–1052.

# Appendix A

## The Geosynchronous Orbit Environment

### A.1 Fundamentals of GEO Orbit

Geosynchronous orbit (GEO) is a unique orbit about the Earth in which the period of motion is approximately one sidereal day (86164 seconds), such that a GEO satellite moves within its orbit at the same rate that the Earth rotates about its spin axis.[38] In this manner, GEO satellites appear from the Earth-centered, Earth-fixed (ECEF) frame to be stationary in longitude; those synchronous satellites that are furthermore in circular ($e = 0$), equatorial ($i = 0°$) orbits are *geostationary* in that these satellites are completely motionless in the sky from the perspective of a ground observer fixed to Earth. The rotation rate of Earth is approximately $\omega_\oplus \approx 72.9217 \times 10^{-6}$ rad/s,[41] which is equal to the mean motion for GEO:

$$\omega_\oplus = \sqrt{\frac{\mu_\oplus}{r_{\text{GEO}}^3}} \implies r_{\text{GEO}} = 42{,}164.17 \text{ km} \tag{A.1}$$

Thus, the GEO ring is approximately 35,786 km (or 22,236 miles) above the surface of the Earth,[1] an altitude at which a single GEO satellite can observe ~42% of the Earth's surface, with latitudinal coverage extending from 81°S to 81°N.[41] The GEO ring is therefore very attractive for communications, data relay, and Earth-observation applications because of such extensive on-ground coverage, and furthermore because it is not necessary to accurately follow GEO satellites to determine where to point antennas (e.g., DIRECTV dishes). Figure A.1 shows two views of Earth from the GEO altitude, captured in late January 2015

[1] Put in perspective, this altitude is roughly nine times the distance from New York City to Los Angeles, which is approximately one-tenth of the average distance from the Earth to its nearest neighbor, the Moon.

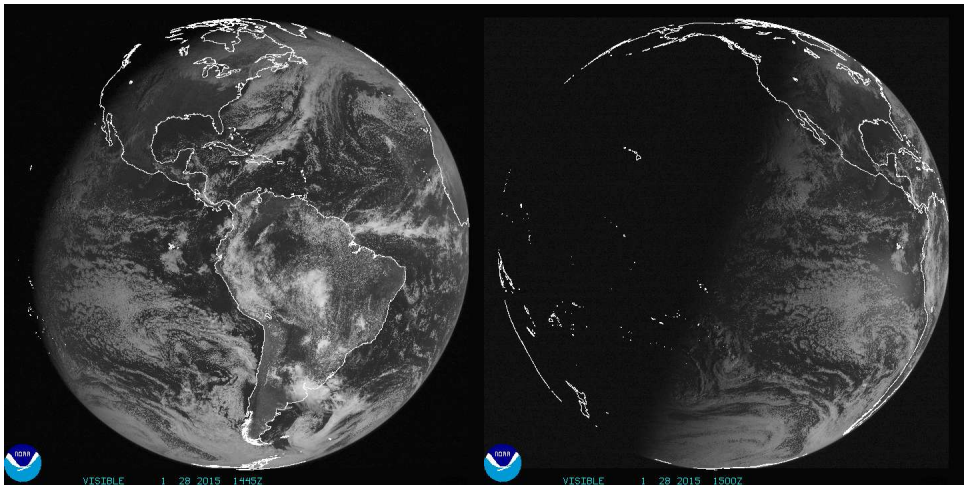

Figure A.1: Full disk views of Earth from GOES East and West satellites.

by the National Oceanic and Atmospheric Administration's (NOAA) Geostationary Operational Environmental Satellite system (GOES), currently stationed at 105°W and 135°W.[2]

Relative to the rotating ECEF frame, true geostationary satellites appear motionless, i.e., the ground track over one revolution appears as a single point in the equatorial plane. Inclined, geosynchronous objects in circular orbits have ground tracks that appear as vertical lines, reflecting the short-period change in latitude experienced over each revolution. Inclined, geosynchronous objects in elliptic orbits exhibit "figure-8" analemmas as a result of non-zero eccentricity. Although the mean motion for these objects matches the rotation rate of Earth, non-zero true anomaly acceleration induces eastward drift during periapsis passage that is counteracted by westward drift accumulated during apoapsis passage. The combination of this daily longitude pattern with north-south latitude motion gives the resulting analemma a "double teardrop" or "figure-8" shape. Inclined, near-geosynchronous objects have sinusoidal ground tracks, which result from the combination of north-south latitude motion with continuous drift in longitude (eastward for objects beneath the GEO altitude, and westward for objects above the GEO altitude). Figure 2.3 in Chapter 2 shows

[2] Full disk, hemispheric, and regional images and visualizations are available on NOAA's Geostationary Satellite Server at: `http://www.goes.noaa.gov`.

several examples of these once-daily ECEF trajectories relative to the GEO longitude slots.

## A.2 Natural Perturbations in the GEO Environment

As described in Chapter 2, the two-body equations of motion for uncontrolled objects at GEO are augmented by various environmental perturbations that naturally occur at the GEO altitude. Specifically, the equations of motion for each uncontrolled GEO object are

$$\ddot{\boldsymbol{r}} = -\frac{\mu_\oplus}{r^3}\boldsymbol{r} + \boldsymbol{a}_\oplus + \boldsymbol{a}_\mathfrak{D} + \boldsymbol{a}_\odot + \boldsymbol{a}_{\text{SRP}} \tag{A.2}$$

where the first term denotes two-body acceleration, $\boldsymbol{a}_\oplus$ is the perturbation due to the non-sphericity of Earth, $\boldsymbol{a}_\mathfrak{D}$ and $\boldsymbol{a}_\odot$ are the third-body perturbations from the Moon and Sun, respectively, and $\boldsymbol{a}_{\text{SRP}}$ is the SRP perturbation. In the following sections, the specific computations applied for evaluating each of the perturbations in Equation (A.2) are presented, as implemented in custom ANSI-C software tools developed for this dissertation research.

### A.2.1 Non-Spherical Earth Perturbations

Non-spherical Earth perturbations are commonly modeled via a spherical harmonics expansion of the Earth's gravitational field, in which the retention of higher-order terms in the series expansion provides a higher-fidelity model for the "lumpy" topography of Earth (recall that the two-body acceleration in Equation (A.2) is derived under the uniformity of a point-mass assumption). Using a potential function $U$ to model the irregular distribution of Earth's mass, $\boldsymbol{a}_\oplus$ is expressed in Earth-centered, Earth-fixed frame components as:[38] [3]

$$a_\oplus^x = \left(\frac{1}{r}\frac{\partial U}{\partial r} - \frac{r_z}{r^2\sqrt{r_x^2+r_y^2}}\frac{\partial U}{\partial \phi}\right) r_x - \left(\frac{1}{r_x^2+r_y^2}\frac{\partial U}{\partial \lambda}\right) r_y \tag{A.3}$$

$$a_\oplus^y = \left(\frac{1}{r}\frac{\partial U}{\partial r} - \frac{r_z}{r^2\sqrt{r_x^2+r_y^2}}\frac{\partial U}{\partial \phi}\right) r_y + \left(\frac{1}{r_x^2+r_y^2}\frac{\partial U}{\partial \lambda}\right) r_x \tag{A.4}$$

$$a_\oplus^z = \frac{r_z}{r}\frac{\partial U}{\partial r} + \frac{\sqrt{r_x^2+r_y^2}}{r^2}\frac{\partial U}{\partial \phi} \tag{A.5}$$

[3] Note that because Equations (A.3)-(A.5) provide the perturbing acceleration in non-inertial ECEF components, the acceleration vector must be converted into inertial frame components for numerical integration.

where $(r_x, r_y, r_z)^T$ denotes the satellite position vector in ECEF components, $\phi$ and $\lambda$ denote geocentric latitude and longitude, respectively, and the partial derivatives of the potential with respect to spherical coordinates are evaluated to the desired degree and order with[38]

$$\frac{\partial U}{\partial r} = -\frac{\mu_\oplus}{r^2}\sum_{l=2}^{\infty}\sum_{m=0}^{l}\left(\frac{R_\oplus}{r}\right)^l (l+1)P_{l,m}(\sin\phi)\Big[C_{l,m}\cos(m\lambda) + S_{l,m}\sin(m\lambda)\Big] \tag{A.6}$$

$$\begin{aligned}\frac{\partial U}{\partial \phi} = \frac{\mu_\oplus}{r}\sum_{l=2}^{\infty}\sum_{m=0}^{l}\left(\frac{R_\oplus}{r}\right)^l &\Big[P_{l,m+1}(\sin\phi) - m\tan(\phi)P_{l,m}(\sin\phi)\Big] \\ &\times \Big[C_{l,m}\cos(m\lambda) + S_{l,m}\sin(m\lambda)\Big]\end{aligned} \tag{A.7}$$

$$\frac{\partial U}{\partial \lambda} = \frac{\mu_\oplus}{r}\sum_{l=2}^{\infty}\sum_{m=0}^{l}\left(\frac{R_\oplus}{r}\right)^l mP_{l,m}(\sin\phi)\Big[S_{l,m}\cos(m\lambda) - C_{l,m}\sin(m\lambda)\Big] \tag{A.8}$$

where $R_\oplus$ is the Earth's equatorial radius, $P_{l,m}$ denote the associated Legendre functions of degree $l$ and order $m$, $C_{l,m}$ and $S_{l,m}$ are the un-normalized Stokes coefficients for the EGM-96 gravity model,[4] and the geocentric latitude and longitude coordinates are computed by

$$\phi = \sin^{-1}\left(\frac{r_z}{\sqrt{r_x^2 + r_y^2 + r_z^2}}\right) \tag{A.9}$$

$$\lambda = \tan^{-1}\left(\frac{r_y}{r_x}\right) \tag{A.10}$$

As shown in Figure A.2, three classes of spherical harmonics are described by the Stokes coefficients: (a) *zonal* harmonics, defined by $l \neq 0$ and $m = 0$, which represent symmetric latitude bands, (b) *sectorial* harmonics, defined by $l = m$, which represent longitude bands, and (c) *tesseral* harmonics, defined by $l \neq m \neq 0$, which describe specific, "tile-like" regions on the surface of the Earth.[3,38] The dominant zonal harmonic $J_2 \equiv -C_{2,0}$ describes the gravitational perturbations resulting from the oblateness of the Earth, while the coefficient $J_{2,2} \equiv \sqrt{C_{2,2}^2 + S_{2,2}^2}$ describes the longitudinal "bulges" responsible for libration motion—and consequently, the need for weekly, east-west station-keeping—of satellites near GEO. Section A.3 gives a high-level overview of why libration motion physically occurs at GEO.

[4] Normalized Stokes coefficients for the EGM-96 gravity model are available from: `http://cddis.nasa.gov/926/egm96/egm96.html`. Reference 38 gives the normalization process and shows how to un-normalize.

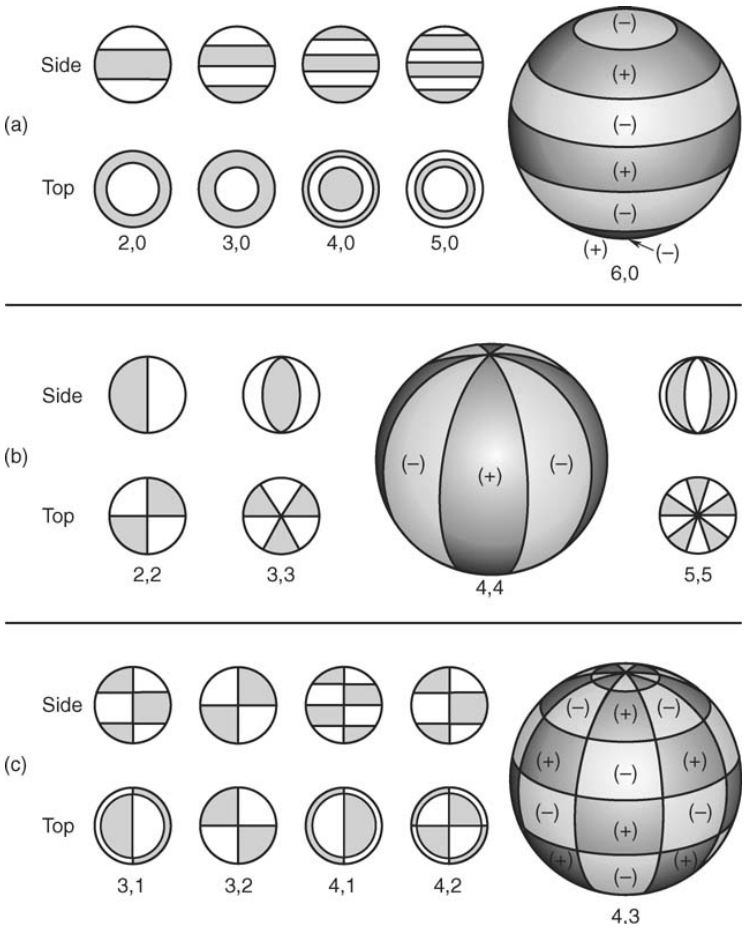


Figure A.2: Illustration of various Stokes coefficients.[3]

### A.2.2 Luni-Solar Perturbations

Direct and indirect perturbations from the gravitation of the Sun and Moon are modeled using the framework of the three-body Newtonian gravitation problem as follows:[38]

$$\boldsymbol{a}_{\mathbb{D}} = \mu_{\mathbb{D}} \left( \frac{\boldsymbol{r}_{j,\mathbb{D}}}{\|\boldsymbol{r}_{j,\mathbb{D}}\|^3} - \frac{\boldsymbol{r}_{\oplus,\mathbb{D}}}{\|\boldsymbol{r}_{\oplus,\mathbb{D}}\|^3} \right) \tag{A.11}$$

$$\boldsymbol{a}_{\odot} = \mu_{\odot} \left( \frac{\boldsymbol{r}_{j,\odot}}{\|\boldsymbol{r}_{j,\odot}\|^3} - \frac{\boldsymbol{r}_{\oplus,\odot}}{\|\boldsymbol{r}_{\oplus,\odot}\|^3} \right) \tag{A.12}$$

where $\boldsymbol{r}_{j,\mathbb{D}/\odot} = \boldsymbol{r}_{\mathbb{D}/\odot} - \boldsymbol{r}_j$ is the inertial position vector from the satellite to the Moon/Sun, and $\boldsymbol{r}_{\oplus,\mathbb{D}/\odot} = \boldsymbol{r}_{\mathbb{D}/\odot} - \boldsymbol{r}_{\oplus}$ is the inertial position vector from the Earth ($\oplus$) to the Moon/Sun, respectively. The constants $\mu_{\mathbb{D}} \equiv GM_{\mathbb{D}}$ and $\mu_{\odot} \equiv GM_{\odot}$ are the gravitational parameters of

the Moon and Sun. Luni-solar gravitation therefore exerts a direct, two-body perturbation on the satellite's motion, and furthermore exerts an indirect perturbation via gravitational interactions with Earth. As discussed in detail in Chapter 3, these luni-solar perturbations couple with the $J_2$ harmonic to drive a 53-year, cyclical progression of the orbit plane that is reflected in the phase portrait for doubly-averaged inclination and RAAN variations.[3]

### A.2.3 Solar Radiation Pressure Perturbation

The solar radiation pressure acceleration is modeled with the classical "cannonball" formulation, in which the geometry of the propagated satellite is simplified as a sphere.[38] This model serves as a convenient approximation for high-fidelity SRP acceleration, which is dependent not only on accurate knowledge of the Sun's location relative to the satellite, but the satellite's attitude, time-varying cross-sectional area exposed to the Sun, and time-varying reflectivity coefficients, which govern the degree to which individual surfaces are translucent, absorptive, or reflective.[38] In this model, the perturbative SRP acceleration is

$$\boldsymbol{a}_{\text{SRP}} = -p_{\text{SRP}} c_r \beta \left( \frac{\boldsymbol{r}_{j,\odot}}{\|\boldsymbol{r}_{j,\odot}\|} \right) \tag{A.13}$$

where $p_{\text{SRP}}$ is the solar radiation pressure at the satellite's location, $c_r$ is the mean coefficient of reflectivity, and $\beta \equiv A_\odot/m$ is the exposed-area-to-mass ratio, for which $\beta \approx 0.04$ m$^2$/kg is representative for typical GEO satellites.[43] The term $\boldsymbol{r}_{j,\odot} = \boldsymbol{r}_\odot - \boldsymbol{r}_j$ denotes the position vector of the Sun relative to the satellite, expressed in inertial frame (i.e., ECI) coordinates. Solar radiation pressure $p_{\text{SRP}}$ is modeled using the inverse-square "diffusion" formulation

$$p_{\text{SRP}} = \frac{L_\odot}{4\pi \|\boldsymbol{r}_{j,\odot}\|^2 c} \tag{A.14}$$

where $L_\odot \approx 3.839 \times 10^{26}$ W is the mean solar luminosity, and $c \approx 3 \times 10^8$ m/s$^2$ is the speed of light, such that $p_{\text{SRP}} \approx 4.55 \times 10^{-6}$ N/m$^2$ at 1 AU. Per Equation (A.13), this value for the solar pressure yields $\|\boldsymbol{a}_{\text{SRP}}\| \approx 2.73 \times 10^{-7}$ m/s$^2$ at 1 AU assuming the reflectivity $c_r = 1.5$. To account for eclipsing at GEO, the magnitude of this acceleration is attenuated by using the scaling factor derived from the geometric occultation algorithm given in Reference 42.

Physically, the SRP perturbation accelerates a satellite as it moves opposite the local Sun direction during its orbital motion, and decelerates the satellite as it moves towards the Sun. The cumulative end-result over the course of one year is a periodic oscillation in both the magnitude and direction of the eccentricity vector, which is minimized by operators by choosing the perigee of the operational orbit such that it points in the Sun direction.[3,47,59]

## A.3 Why Does Libration Motion Occur?

As stated in Section A.2.1, the second degree and second order sectorial harmonic, as represented by the Stokes coefficients $C_{2,2}$ and $S_{2,2}$, quantifies the gravity perturbations induced by Earth's longitudinal bulges, which are responsible for driving periodic, libration motion at GEO. To gain intuition as to why these oscillations in longitude physically occur, Figure A.3 shows a top-down schematic of Earth as represented by the dominant $C_{2,2}$ term only, which corresponds to equatorial ellipticity.[38] By symmetry, the gravitational force $\boldsymbol{F}$ will be purely radial when the satellite is on an extension of either the major or minor axes of this ellipse. When the satellite is off-axis, however, a tangential component of $\boldsymbol{F}$ directed towards the nearest major axis arises.[38] By Newton's second law, does this induce longitudinal acceleration in the direction of the tangential component, or against this direction?

Consider a circular orbit of semi-major axis $a$, and let $\boldsymbol{F} = F_\theta \hat{\boldsymbol{o}}_\theta$ be expressed in the local tangential direction. The radial component of $\boldsymbol{F}$ is excluded here because we are only interested in the change in orbital energy arising from the tangential component $F_\theta$, i.e., the deviation from a purely-radial gravitational attraction assumed in the two-body problem. The position vector is $\boldsymbol{r} = a\hat{\boldsymbol{o}}_r$ and, by application of the transport theorem, the velocity is $\dot{\boldsymbol{r}} = \dot{a}\hat{\boldsymbol{o}}_r + an\hat{\boldsymbol{o}}_\theta$. Differentiating the well-known, two-body orbit energy equation, we have

$$\epsilon = -\frac{\mu}{2a} \implies \dot{\epsilon} = \frac{\mu}{2a^2}\dot{a} \tag{A.15}$$

From mechanics, the energy rate $\dot{\epsilon}$ is given by the product of force and velocity, such that

$$\dot{\epsilon} = \boldsymbol{F} \cdot \dot{\boldsymbol{r}} = anF_\theta \tag{A.16}$$

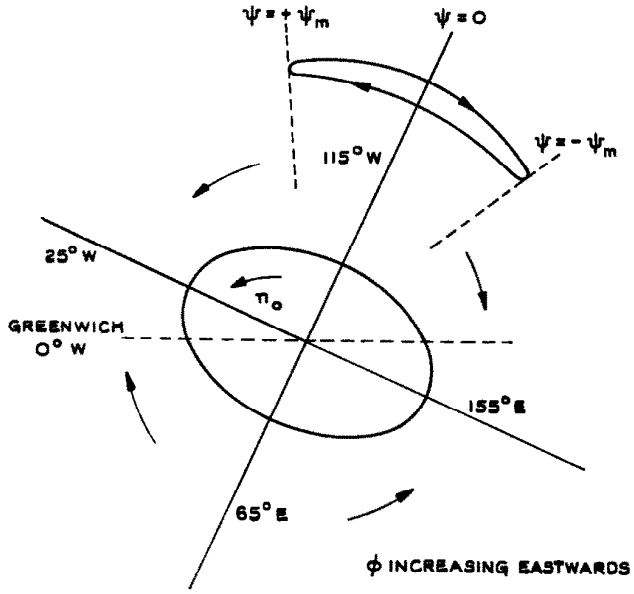


Figure A.3: Top-down schematic showing ellipticity of Earth.[4]

Equating Equations (A.15)-(A.16) and using the identity $\mu = n^2 a^3$, the semi-major axis rate is directly proportional to the tangential force component:

$$\dot{a} = \frac{2}{n} F_\theta \tag{A.17}$$

Thus, as the satellite is approaching an extension of the major axis of the equatorial ellipse, two-body energy and the semi-major axis increase, since $\dot{a} > 0$ because $F_\theta > 0$. Conversely, as the satellite is approaching an extension of the minor axis, two-body energy and semi-major decrease, since $\dot{a} < 0$ because $F_\theta < 0$ (i.e., opposite to the local tangential direction).

Noting that the longitudinal drift rate is given by $\dot{\lambda} = n - \omega_\oplus$, then the longitudinal acceleration is given by $\ddot{\lambda} = \dot{n}$, or

$$\ddot{\lambda} = \frac{\mathrm{d}}{\mathrm{d}t}\left(\sqrt{\frac{\mu}{a^3}}\right) = -\frac{3n}{2a}\dot{a} = -\frac{3}{a}F_\theta \tag{A.18}$$

Thus, acceleration in longitude opposes the tangential force component.[4] As the satellite is approaching an extension of the major axis of this ellipse, $\dot{a} > 0$ but $\ddot{\lambda} < 0$, such that the satellite slows in longitude until reversing direction once $\dot{\lambda} = 0$ is reached. Conversely, the satellite accelerates in longitude as it approaches a minor axis of the ellipse, because $\dot{a} < 0$

but $\ddot{\lambda} > 0$. Since momentum is gained as the longitude accelerates towards the minor axis, the satellite drifts past this point, the tangential force component reverses direction in the local orbit frame, and the process repeats, producing the libration effect.[38] As a result, the two extensions of the minor axis are called the *stable equilibrium points* (or potential wells), which lie at 75°E and 105°W, while the extensions of the major axis are termed the *unstable equilibrium points* (or potential hills), which lie at 165°E and 15°W by ellipse symmetry.[5]

To illustrate the coupling between semi-major axis and longitude that occurs during libration about one of the stable equilibrium points, Figure A.4 shows a five-year libration profile for an uncontrolled GEO object starting at 160°W (55°W of the well at 105°W). The semi-major axis decreases until the satellite reaches the stable point at approximately nine months, after which it begins increasing until the satellite slows down, reverses direction at 50°W (55°E of the well at 105°W), and once again reaches the stable point on the reverse pass. According to Figure A.4, the simulated object has a libration period of approximately three years, which is proportional to the amplitude of the libration motion (Chapter 5).[4]

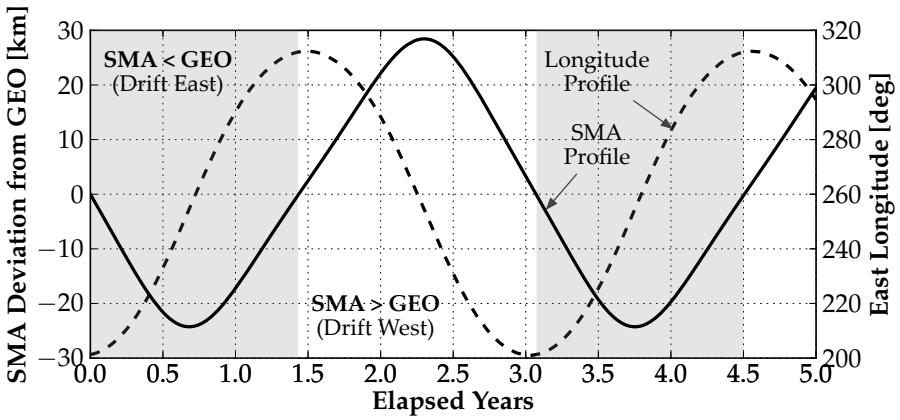


Figure A.4: Five-year libration profile for GEO satellite at 160°W.

In the same manner than inclination drift driven by luni-solar perturbations creates the need for north-south station-keeping, longitude drift driven by the second degree and

[5] The longitudes for the stable and unstable points in Figure A.3 differ by 10° because of the uncertainties in the exact values for the $C_{2,2}$ and $S_{2,2}$ coefficients in 1963, the year of Figure A.3's original publication.[4]

order sectorial harmonic creates the need for routine, east-west station-keeping. If higher-order terms in the spherical harmonics expansion are truncated, an exact analytic solution for the semi-major axis drift rate—and consequently, the longitudinal acceleration—can be derived as a function of longitudinal deviation $\Delta\lambda \equiv \lambda - \lambda_{2,2}$ from the nearest major axis:[3]

$$\dot{a}(\lambda) = -12 r_{\text{GEO}} n_{\text{GEO}} J_{2,2} \left(\frac{R_\oplus}{r_{\text{GEO}}}\right)^2 \sin(2\Delta\lambda) \approx -132 \sin(2\Delta\lambda) \quad \text{[m/day]} \tag{A.19}$$

$$\ddot{\lambda}(\lambda) = -\frac{3n}{2r_{\text{GEO}}}\dot{a}(\lambda) \qquad \approx 0.0017 \sin(2\Delta\lambda) \quad \text{[deg/day}^2\text{]} \tag{A.20}$$

These are beneficial for estimating annual east-west station-keeping budgets based on the operational longitude slot. Figure A.5 illustrates Equations (A.19)-(A.20) by providing the semi-major axis drift and longitude acceleration accumulated over the course of one day. Since the gravitational force is completely radial on either the major or minor axes of the equatorial ellipse, then $F_\theta = 0$ and $\dot{a}$ and $\ddot{\lambda}$ vanish at these locations. Maximum semi-major axis and longitude drift occur midway between each of the four stable/unstable pairs,[3,4] such that the annual east-west station-keeping cost is maximized at these longitudes. GEO satellites located at or near the stable points incur minimal east-west station-keeping costs, and have the benefit of passive stability (i.e., minimal libration amplitude) if thrusters fail.

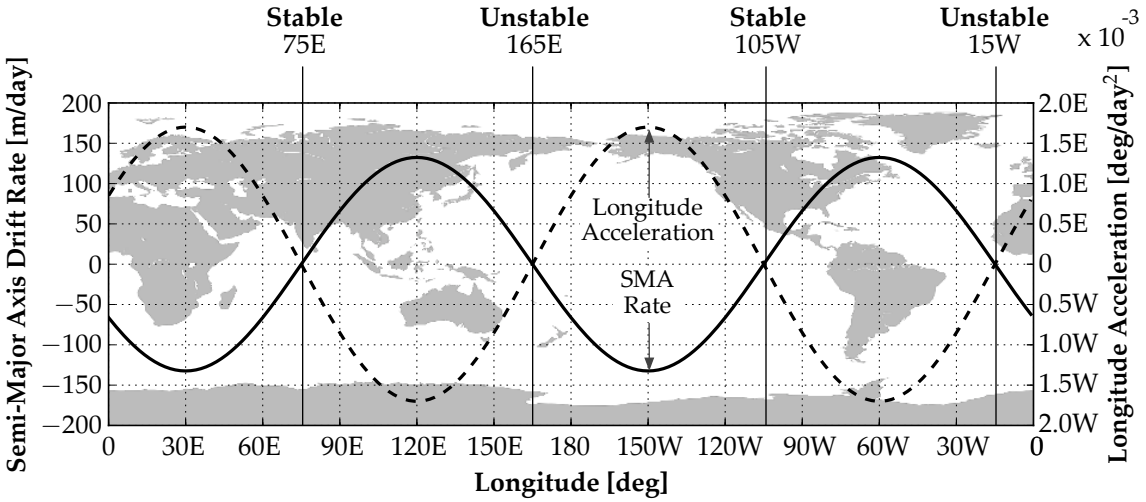


Figure A.5: Daily semi-major axis and longitude drift as a function of longitude.